# STATIC AND DYNAMIC BEHAVIOR OF WELDED JOINTS FOR AN ARMORED Mn-Si-Cr STEEL

R. Serrano[a], R. R. Ambriz[a*], C. García[b], D. Jaramillo[a]

[a] Instituto Politécnico Nacional CIITEC-IPN, Cerrada de Cecati S/N, Col. Sta. Catarina, C.P. 02250 Azcapotzalco, Ciudad de México, México.
[b] Facultad de Ingeniería, Universidad Autónoma de San Luis Potosí, Av. Dr. Manuel Nava No. 8, Zona Universitaria, C.P. 78290, San Luis Potosí, S.L.P., México.

E-mail address: rrambriz@ipn.mx

**Abstract**

Mechanical properties of gas metal arc welds performed on a quenched and tempered low-alloy armored (QTLA) steel, using ferritic and nickel-based alloy fillers are reported. Microhardness, tensile, instrumented Charpy impact, free fall vertical impact and high-cycle fatigue tests were performed. Mechanical properties were correlated to the microstructural characteristics of the welded joints. Also, a fracture surfaces analysis was carried out.

It was observed that welded joints performed by a nickel-based alloy filler metal (ERNiFeCr-2) tend to increase its mechanical resistance in relation to the weldments made with a commonly used ER-70S filler metal. An improvement of 6.5% in hardness, 33% in tensile strength, 25% on impact resistance and 20% on the fatigue strength coefficient was observed. However, an important loss of ductility was also detected (approximately 50%). This behavior was attributed to the carbides formation in the fusion zone, increasing the strength of the welded joints but also acting as preferential sites for crack nucleation decreasing ductility.

***Keywords***: Welding, GMAW, Armored Steel, Inconel 718, High Cycle Fatigue, Impact Testing.

## 1. Introduction

Martensitic steels have been historically used on ballistic applications due to their good ratio between resistance and ductility. Additionally, high hardness levels become necessary to avoid projectile penetration [1]. The main issues when welding armored steels are excessive hardening on the heat affected zone (HAZ), cracking induced by hydrogen diffusion, as well as poor hardness and low resistance on the fusion zone [2]. The excessive hardening and hydrogen induced cracking can be solved by using adequate preheating and inter-pass temperatures [3].

Aiming to improve the mechanical properties of the fusion zone, this work proposed the use of a nickel-based filler (ERNiFeCr-2) that is used to weld Inconel 718 alloy. The mechanical and microstructural properties of nickel-based weldments were compared to those performed using a ferritic filler metal (ER-70S).

## 2. Methodology

### *2.1. Materials and welding*

Quenched and tempered low-alloy armored steel plates (20×70×10 mm) were used. The chemical composition (weight percent) of the steel is as followed: 0.22% C, 1.36% Mn, 0.4517% Si, 0.3829% Cr. This composition in conjunction with the heat treatment provided the following hardness and tensile properties: 283 $HV_{0.5}$ on the LT direction, 501 $HV_{0.5}$ on the LC direction, and 424 $HV_{0.5}$ on the TC direction, as well as 1.3 GPa and 1.67 GPa for yield and ultimate tensile strength, respectively.

Double Vee grooves with a root separation of 1.3 mm were machined on the plates to deposit weld beads by using GMAW process (DCEP). The following welding parameters were used:

**Table 1**. Welding parameters.

| | ER-70S | ERNiFeCr-2 |
|---|---|---|
| Shielding gas | Ar+$CO_2$ | Ar |
| Voltage | 26 v | 26.5 (high impedance) |
| Feed | 133 $mms^{-1}$ | 140 $mms^{-1}$ |

### *2.2. Mechanical properties and microstructure*

The mechanical properties of the welds were evaluated by means of microhardness, tensile, high cycle fatigue, instrumented Charpy impact and free fall vertical impact testing.

Optical and scanning electron microscopies were used to analyze the microstructure and fracture surfaces of the welded joints. Additionally, energy dispersive X-ray spectroscopy (EDX) was used to determine the chemical composition on the different regions of the joints.

## 3. Results and discussion

### *3.1. Mechanical properties of the welds*

Figure 1 shows the microhardness profiles of the welded joints. A low hardness zone is observed in the fusion zone (FZ) due to the formation of a different microstructure in comparison with the base material (BM), followed by a recrystallization or tempering zone located approximately at 7.5 mm from the center of the FZ.

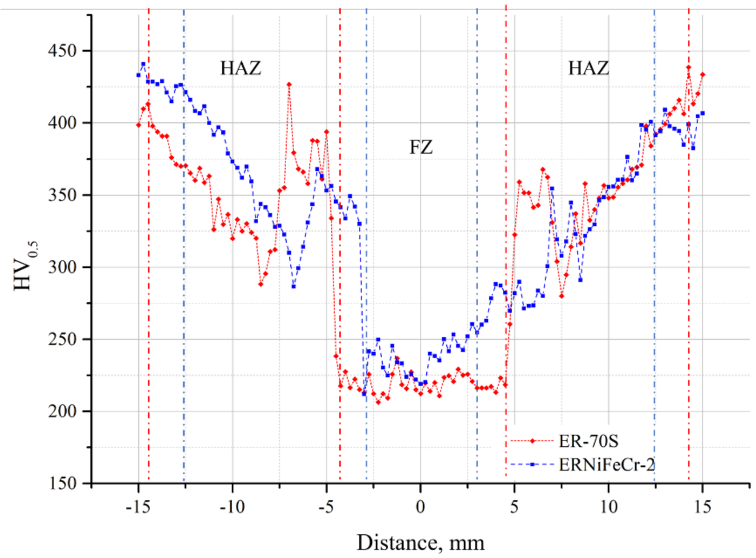


**Figure 1**. Microhardness profiles of the welded joints.

Figure 2 shows the results from tensile and Charpy impact tests. The weldments from both filler materials exhibited a lower tensile strength (~0.5 compared to the base material). After the tensile tests the failures were found in the FZ. It was observed an increment in the yield and ultimate tensile strength on the joints performed using nickel-based filler in comparison to the joints made with a ferritic filler. This strength improvement was attributed to the presence of carbides and secondary phases. Nevertheless, a loss of ductility (ERNiFeCr-2 joints) due to the brittle particles presence that act as preferential sites for crack nucleation was also observed.

A similar behavior was observed on the impact testing results. The ERNiFeCr-2 weldments presented an increment on impact resistance, but the shorter impact resistance times indicated ductility losses (Figure 2b and c).

Figure 3 shows the results obtained from high-cycle fatigue testing performed on the BM and the welded joints. From Figure 3b it was observed that welded joints made with ERNiFeCr-2 filler material have a greater fatigue resistance coefficient, however, the corresponding curve has a steeper slope, causing the fatigue life to decrease more abruptly.

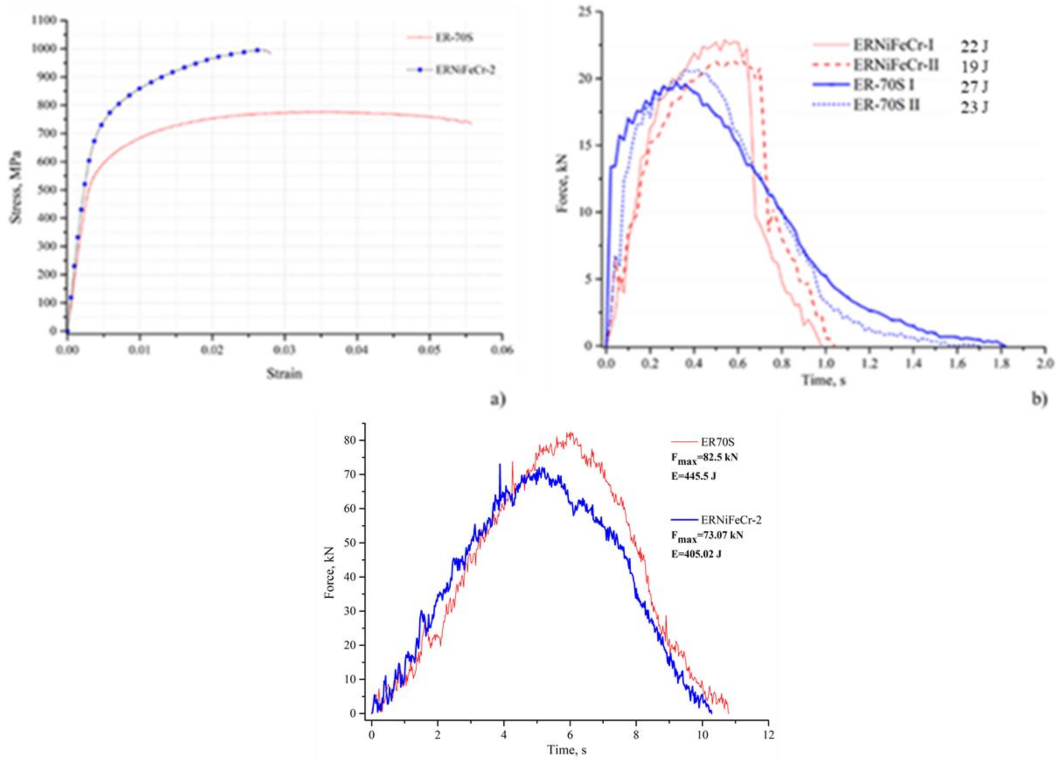


**Figure 2.** a) Conventional stress-strain curves for welded joints. b) force-time curves obtained from instrumented impact Charpy tests for welded joints and c) force-time curves obtained from the vertical impact testing

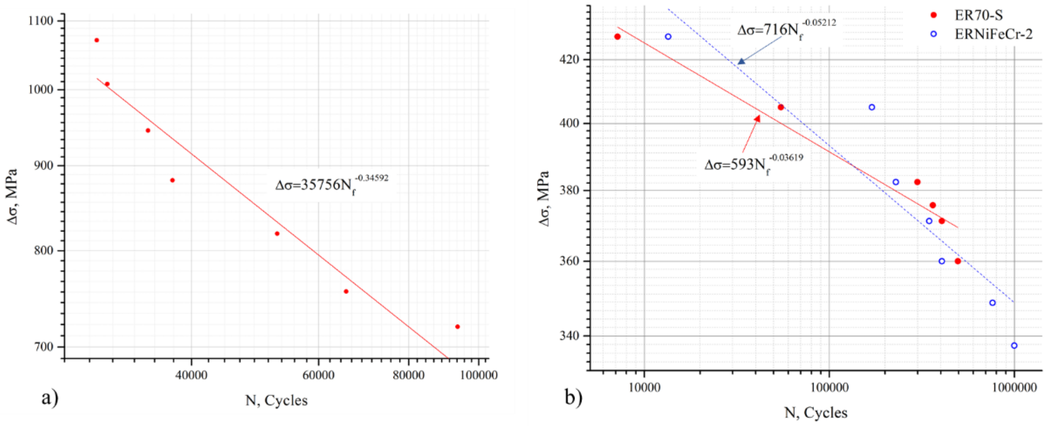


**Figure 3**. S-N curves for a)base material and b) welded joints.

*3.2. Microstructural Characterization*

*3.2.1. Metallographic analysis*

The microstructure of the welded joints is shown in Figure 4. From this figure it is possible to observe the interface between the FZ and HAZ for both conditions. Figure 4a and b shows that the microstructure of the FZ corresponding to the ER70-s welds is formed by a ferrite matrix and perlite. In contrast, the FZ of the ERNiFeCr-2 welds consists of an austenitic matrix with element segregation in the grain boundaries. Also, an unmixed zone between the FZ and the BM is observed. Figure 5 shows the variation of the chemical composition along the welded joints.

*3.2.2. Fracture surfaces analysis*

Fracture analysis of ER-70S welds reveals the formation of dimples and micro voids that are commonly observed in ductile fractures. The fracture surfaces of ERNiFeCr-2 welds also show dimples and micro voids, but in this case, due to the strong tendency of the material to form carbides in fast cooling conditions, detachments and broken particles can be observed. Those particles are responsible of the increment in tensile strength and hardness in this welding condition. However, these particles act as preferential sites for crack nucleation decreasing the fatigue life of the welded joints.

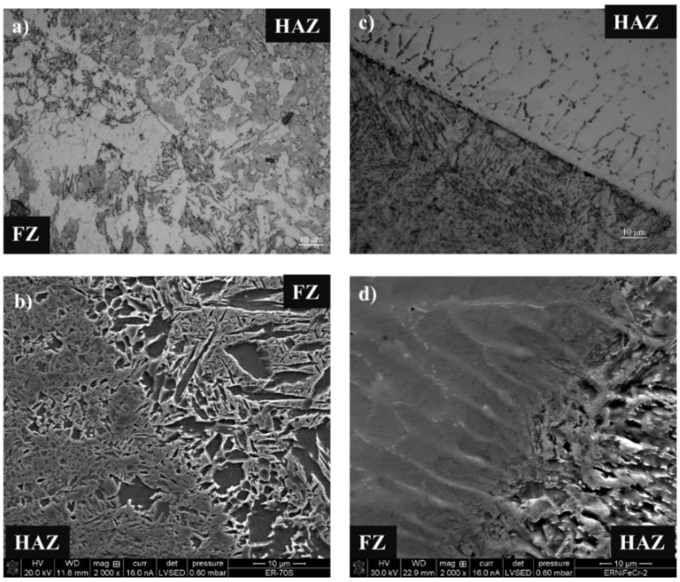


**Figure 4.** Metallographic samples of ER-70S (a, b) and ERNiFeCr-2 (c, d) welded joints.

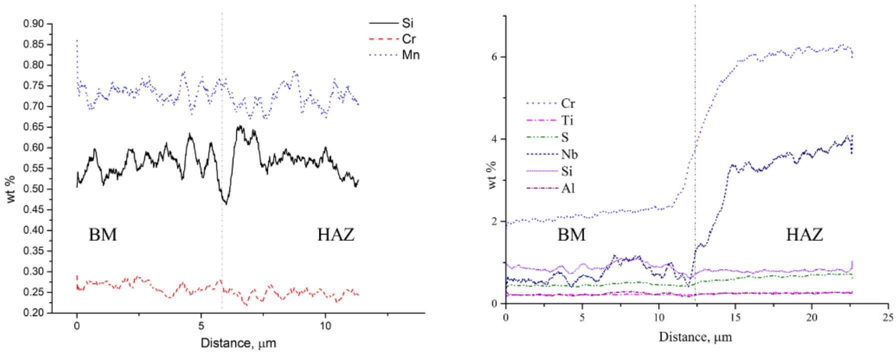


**Figure 5.** Chemical composition variation along the welded joints.

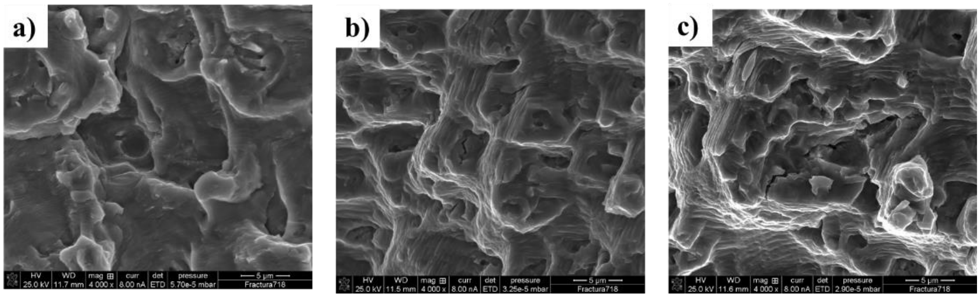


**Figure 6**. Fatigue fracture surface of ERNiFeCr-2 welds.

## 4. Conclusions

Due to the tendency of the ERNiFeCr-2 FZ to the formation of carbides in fast cooling conditions. During the welding thermal cycle numerous brittle particles were formed in this material. The particles observed are responsible for the hardness increase, strength improvement and fatigue resistance coefficient improvement; however, those same particles act as preferential sites for crack nucleation causing ductility loses, and a more drastic diminution on the fatigue life compared to the ER-70S joints. Considering that the use of nickel-based filler materials implies a cost 30 times higher; the given advantages for this particular application does not justify the extra investment.

## References.

[1] I. G. Crouch, *Science of armour materials*. Woodhead Publishing, 2017.

[2] G. Magudeeswaran, V. Balasubramanian, T. S. Balasubramanian, and G. M. Reddy, *"Effect of welding consumables on tensile and impact properties of shielded metal arc welded high strength, quenched and tempered steel joints," Sci. Technol. Weld. Join.*, vol. 13, no. 2, pp. 97–105, Feb. 2008.

[3] W. H. Kearns, Ed., *AWS Welding Handbook Seventh Edition*. Palgrave Macmillan, 1983.

# Tensile, Creep, and Fatigue Behaviors of High Density Polyethylene (HDPE)

Mohammadreza Amjadi, Ali Fatemi

*Department of Mechanical Engineering, University of Memphis, Memphis, TN, USA*

*E-mail address:* m.amjadi@memphis.edu

**Abstract**

Tensile, creep, and fatigue behaviors of high-density polyethylene (HDPE) were investigated in this experimental study, including the effects of temperature, strain rate, and multiaxial stress state. In addition to the generated experimental data, predictive models were employed to correlate the data for different conditions. Tensile properties such as tensile strength and elastic modulus were evaluated at different temperatures and strain rates. Larson-Miller parameter was used to correlate creep time to rupture, temperature, and creep stress. A general fatigue model was used to correlate all uniaxial fatigue data at different temperatures, frequencies, and mean stress levels. Multiaxial fatigue behavior of HDPE was also investigated and a critical plane approach is proposed to correlate all multiaxial fatigue data including out of phase loading condition.

***Keywords***: HDPE, Tensile Properties, Creep, Fatigue, Frequency Effect, Temperture Effect, Multiaxial Stress

## 1. Introduction

Polymers and their composites are widely used in many engineering applications due to their excellent properties with production increasing from 1.5 million tons per year in 1950 to 288 million tons in 2012 [1]. Polyethylene is a simple polymer with the basic repeating unit (-CH2–CH2 -) and the most commonly used polymer with a consumption of 84 million tons in 2014. [1]. High-density polyethylene (HDPE) is the most used polyethylene in the world and many studies have evaluated the HDPE characteristics [2-8]. It is a semicrystalline polymer with crystalline and amorphous phases with different degrees of crystallinity. This paper provides a brief overview of tensile, creep, and fatigue behaviors of HDPE. Experimental results as well as predictive models for each section are briefly presented and discussed.

## 2. Monotonic Tensile Behavior

Tensile properties are the basic material properties required in many design applications. In addition, tensile properties may be used as material properties in predictive models, for example creep and/or fatigue. Processing technique may influence the microstructural properties for thermoplastics and affect tensile properties. Tensile properties can be affected by the processing technique used, for example injection molding, compression molding, and blow molding. Tensile properties of thermoplastics can also be significantly affected by temperature and strain rate due to their viscoelastic nature. Tensile strength variations with temperature and strain rate are shown in Figs. 1(a), and 1(b), respectively. These figures indicate the significant effects of temperature and strain rate on tensile strength of HDPE.

## 3. Tensile Creep Behavior

For polymers creep can occur even at room temperature, depending on their glass transition temperature. For HDPE, creep failure is a major concern in design because of its low glass transition temperature (~ -110℃). Creep rupture time depends on both the temperature and the applied stress. Creep stress versus time to rupture were generated from experimental tests at 23℃, 53℃, and 82℃ as shown in Fig. 2(a). A power law equation can be used to represent creep strain versus time, as shown in the figure. The constants for this power law equation are functions of stress and temperature. In addition, Larson-Miller parameter, which has been commonly used for metals, can be used to relate stress, temperature, and time to rupture. This is shown in Fig.2 (b). This parameter is given by:

$$LMP = \frac{(T+273)(\log t_R + C_{LMP})}{1000} \tag{1}$$

where $T$ is temperature in degree Celsius, $t_R$ is time to rupture (Hours), and $C_{LMP}$ is Larson-Miller constant.

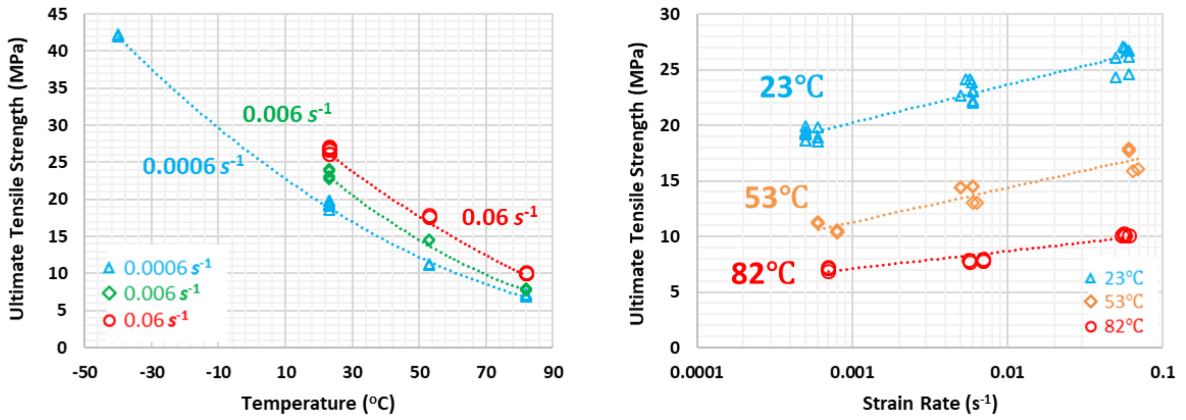


(a) (b)

**Figure 1**: Effects of temperature (a) and strain rate (b) on ultimate tensile strength of HDPE.

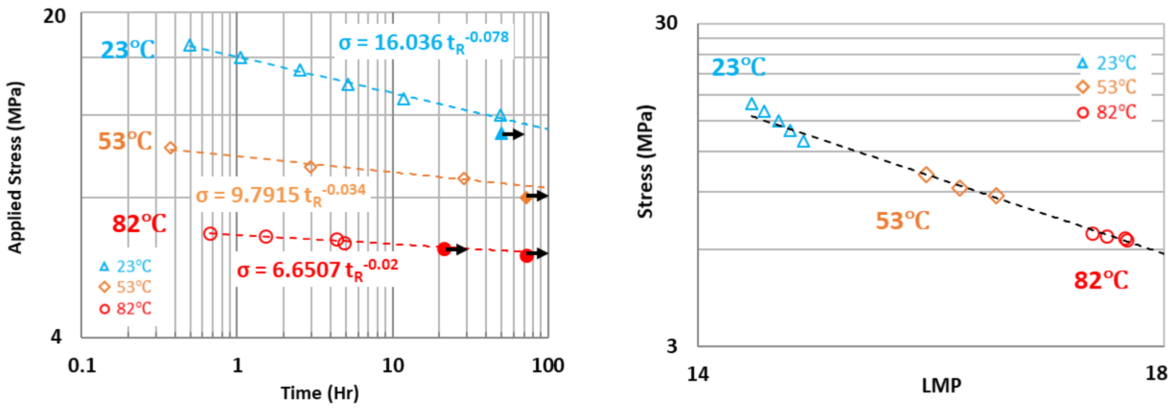


(a) (b)

**Figure 2**: (a) Effect of temperature on creep behavior of HDPE. (b) LMP master curve for HDPE.

## 4. Fatigue Behavior

Fatigue in polymers is affected by different factors from microstructural characteristics to loading conditions. Frequency can have beneficial or detrimental effect on fatigue life of HDPE. The beneficial effect is for higher frequencies (i.e. higher strain rates) but when the temperature rise in the material is below a critical value and self-heating does not occur. On the other hand, if the released energy during cyclic deformation cannot be dissipated fast enough to the environment, the temperature increases and results in thermal failure. As it is shown in Fig. 3(a), test temperature significantly affects fatigue life of HDPE. At elevated temperatures the mobility of the polymer chains in amorphous phase increases, therefore, the semicrystalline structure of HDPE shows more ductility. Higher temperatures also break the secondary molecular bonds in amorphous phase, resulting in strength reduction and lower fatigue strength.

Epaarachchi et al. [9] suggested a fatigue life prediction model based on strength degradation of a polymeric material under constant amplitude loading. This model can be used to account the effects of mean stress, temperature, and frequency (but only the beneficial due to higher loading rate). The fatigue data correlations for HDPE using this model under the aforementioned conditions are shown in Fig. 3(b). The equivalent stress using general model is given by:

$$\sigma_{Nf} = A\left\{\frac{f^{\beta}\left[\sigma_u-\left(\frac{\Delta\sigma}{1-R}\right)\right]}{\alpha\sigma_u^{1-R}\Delta\sigma^{R}} + 1\right\}^{\frac{B}{\beta}} \tag{2}$$

where $A$, $B$ are intercept of S-N line in the reference condition (here taken for $R$ = -1 date at 23°C), $\sigma_u$ is ultimate tensile strength at related temperature in MPa, $f$ is the frequency in Hz, $R$ is stress ratio, $\alpha$ given as function of $\sigma_u$, and $\beta$ = 0.2 for a variety of neat and reinforced thermoplastics. This model cannot, however, account for the detrimental effect of frequency due to self-heating.

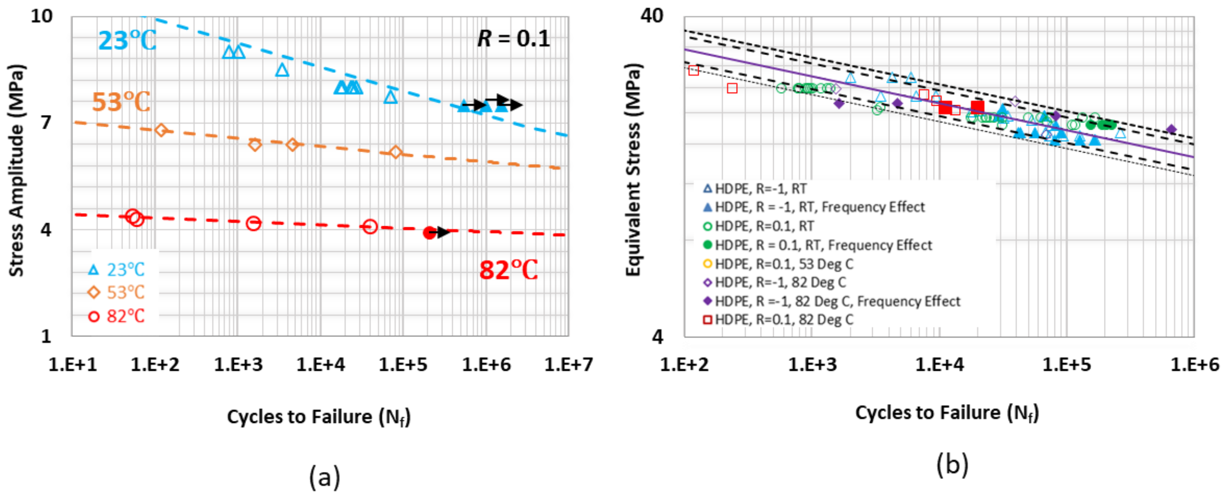


**Figure 3**: (a) Effect of temperature on fatigue behavior of HDPE. (b) Fatigue data correlation using a general model including effects of temperature, frequency, and mean stress.

### 5. Multiaxial Stress Effect on Fatigue Performance

Multiaxial stress state is another important aspect in fatigue behavior of HDPE. Loading of component and structures made of HDPE are not necessarily always uniaxial. There may be different loading sources in terms of applied loads and at different frequencies or out of phase. Therefore, understanding of multiaxial fatigue behavior is important in many design applications. Multiaxial stress states may also exist at stress concentrations such as notch root locations, even under uniaxial loading condition. von-Mises stress and maximum principal stress are the common multiaxial fatigue criteria used in the literature for multiaxial stress states. These criteria are not accurate, especially when it comes to out-of-phase fatigue loading.

Experimental multiaxial fatigue tests were conducted in this study under axial, torsion, in-phase axial-torsion, and out-of-phase axial-torsion for HDPE. The Fatemi-Socie (FS) critical plane damage parameter which is a common multiaxial fatigue parameter used for metals based on the maximum shear strain amplitude and the maximum normal stress on the maximum shear strain range plane. Gates and Fatemi [10] suggested replacement of yield strength as a material property in the original form [11] with $G\Delta\gamma$ [12]. A stress version of this parameter can then be written as:

$$D = \tau_a\left(1 + k\frac{\sigma_{n,max}}{\tau_a}\right) = A\,N_f^{b} \tag{4}$$

where $\tau_a$ is the shear stress amplitude, $\sigma_{n,max}$ is the maximum normal stress, and $k$ is a material constant. Data correlations for multiaxial fatigue data using von-Mises and FS damage parameter are shown in Figs. 4(a), and 4(b), respectively. As can be seen, the FS critical plane damage parameter correlated the data much better than the commonly used von-Mises criterion, particularly for out-of-phase loading.

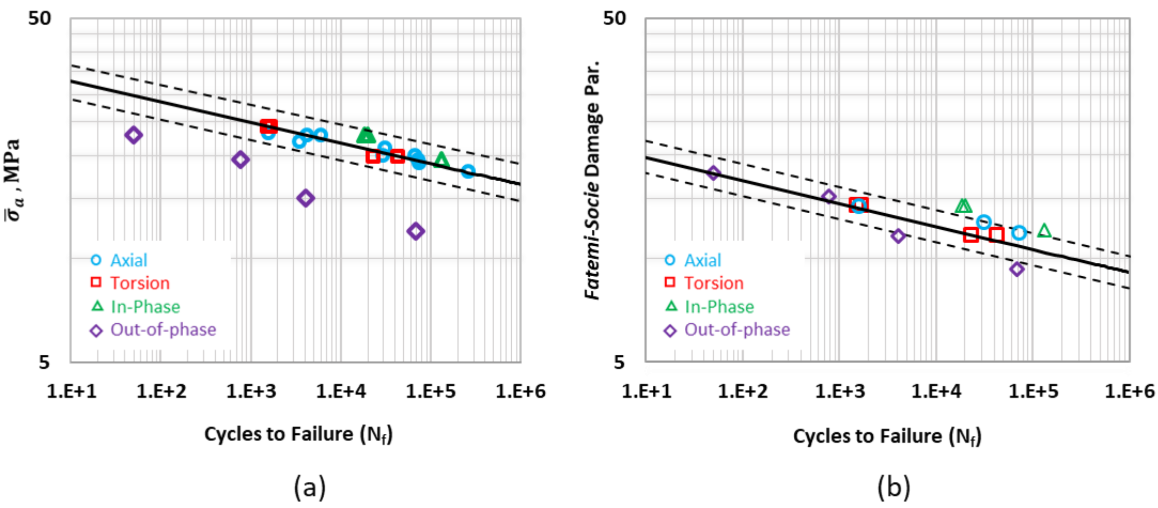


**Figure 4**: Multiaxial fatigue data correlations for HDPE using (a) equivalent von-Mises criterion and (b) Fatemi-Socie damage parameter.

## Acknowledgements

Funding for this study was provided by General Motors Corporation. Technical support of Dr. A.K. Khosrovaneh is appreciated.

## Reference


[1] Spalding, M.A. and Chatterjee, A., Handbook of Industrial Polyethylene and Technology: Definitive Guide to Manufacturing, Properties, Processing, Applications and Markets.Wiley, NJ, USA, 2017

[2] G'Sell, C. and Jonas, J.J., Yield and transient effects during the plastic deformation of solid polymers. "*Journal of Materials Science*", pp. 1956-1974, 1981

[3] Bretz, P.E., Hertzberg, R.W., and Manson, J.A., Mechanisms of fatigue damage and fracture in semi-crystalline polymers. "*Polymer*", pp. 1272-1278, 1981

[4] Lai, J. and Bakker, A., Analysis of the non-linear creep of high-density polyethylene. "*Polymer*", pp. 93-99, 1995

[5] Bonner, M., Duckett, R.A., and Ward, I.M., The creep behaviour of isotropic polyethylene. "*Journal of Materials Science*", pp. 1885-1897, 1999

[6] Riddell, M.N., Koo, G.P., and O'Toole, J.L., Fatigue mechanisms of thermoplastics. "*Polymer Engineering & Science*", pp. 363-368, 1966

[7] Dusunceli, N. and Colak, O., High density polyethylene (HDPE): Experiments and modeling. "*Mechanics of Time-Dependent Materials*", pp. 331-345, 2006

[8] Qi, Z., Lu, L., Doan, L., Thota, B., Zeng, D., and Su, X., Frequency Effects on High-Density Polyethylene Failure under Cyclic Loading. "*SAE International*", 2017

[9] Epaarachchi, J.A. and Clausen, P.D., An empirical model for fatigue behavior prediction of glass fibre-reinforced plastic composites for various stress ratios and test frequencies. "*Composites Part A: Applied Science and Manufacturing*", pp. 313-326, 2003

[10] Gates, N.R., Fatigue Behavior under Multiaxial Stress States Including Notch Effects and Variable Amplitude Loading, University of Toledo, 2016

[11] Fatemi, A. and Socie, D.F., A Critical Plane Approach to Multiaxial Fatigue Damage Including Out-of-Phase Loading. "*Fatigue & Fracture of Engineering Materials & Structures*", pp. 149-165, 1988

[12] Gates, N.R. and Fatemi, A., On the consideration of normal and shear stress interaction in multiaxial fatigue damage analysis. "*International Journal of Fatigue*", pp. 322-336, 2017

# SOFT METACOMPOSITES: THE KIRIGAMI GEOMETRY INVESTIGATION ON FAILURE MODES

Antonio F Ávila[a], Elvis C. Monteiro[b], Milvia Reis[b]

[a]*Universidade Federal de Minas Gerais, Department of Mechanical Engineering, 6627 Antonio Carlos Avenue, Belo Horizonte, 31270-901, Brazil*

[b]*Universidade Federal de Minas Gerais, Mechanical Engineering Graduate Program, 6627 Antonio Carlos Avenue, Belo Horizonte, 31270-901, Brazil*

*E-mail address:* avila@ufmg.br

**Abstract** A failure analysis based on Kirigami's geometry changes is investigated. This special type of soft metamaterial appears to have a mechanical bistability condition. The kirigami experimental response to uniaxial tensile loading can be described by different phenomena, i.e. local buckling and out-of-plane rotation. The first transition region, from the initial elastic regime to a nonlinear regime, is trigger by the critical buckling load. This transition is followed by a secondary elastic plateau. In this case, a dynamic phenomenon is evolving, where buckling occurs at the beams as they rotate to align with the applied load, and deformation occurs out of the plane of the sample. The final stage can be described by the alignment of the struts causes the overall structure to densify perpendicular to the pulling direction. Failure process begins when the ends of the cuts tear and crease owing to high stress at these regions.

***Keywords:*** Metamaterials; Kirigami; Failure modes; Experimental data

## 1. Introduction

Metamaterials are classified as a special group of artificial materials engineered to have a property that is not found in naturally. As commented by Surjadi et al. [1], metamaterials combine the concept of hierarchical architecture with material size effects at micro/nanoscale. The results are materials with superior mechanical performance that allow researchers to explore new options of material properties, e.g. ultra-high strength-to-density ratios and large deformations without yielding. Cellular materials are included in such special class of materials. Additive manufacturing, 3D printing, open a new venue for researchers to study and develop new metamaterials. Figure 1, from Surjadi et al. [1], shows some examples of cellular metamaterials. These materials are in general rigid and can applied into conditions where bending or stretching are the dominated loading conditions. The disadvantage of such metamaterials is they are not flexible.

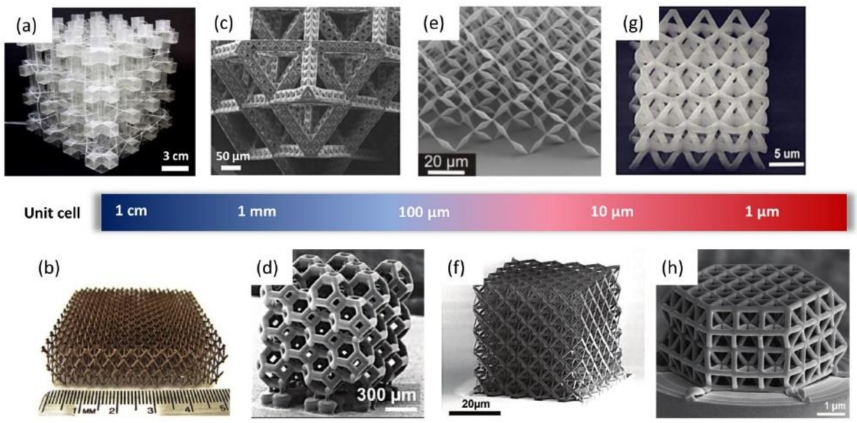


**Figure 1:** Examples of 3D architected cellular materials with unit cell (from [1])

According to Shyu et al. [2] flexible metamaterials emerged based on two ancient Japanese art, i.e. origami and kirigami, which can be used to programmable and reconfigurable mechanical metamaterials. The origami configuration is based on folding patterns and assembling typical planar or 2D materials, in general thin sheets, into complex 3D structures. Such technique has been applied into a variety of applications, e.g. into satellite/space industry [3], biomedical [4], and impact/energy absorption [5]. The difference between origami and kirigami is that for kirigami folding process is combined with cuts. These cuts allow kirigami based structures to be undergo large deformations with failure. Kirigami principles have been employed to design highly stretchable devices and morphing structures. Researchers such as Shyu et al. [2], Isobe and Okumura [6], Hwang and Bartlett [7], Rafsanjani and Bertoldi [8], and Hu et al [9], not only investigated the effects of special distribution of cuts on buckling and post-buckling effects but they also extend its applications to different fields such as energy harvesting [9], and morphing/crawling structures [10]. Figures 2A-B shows separately one origami (biomedical/cardiovascular stents) and one kirigami (morphing/crawling) application.

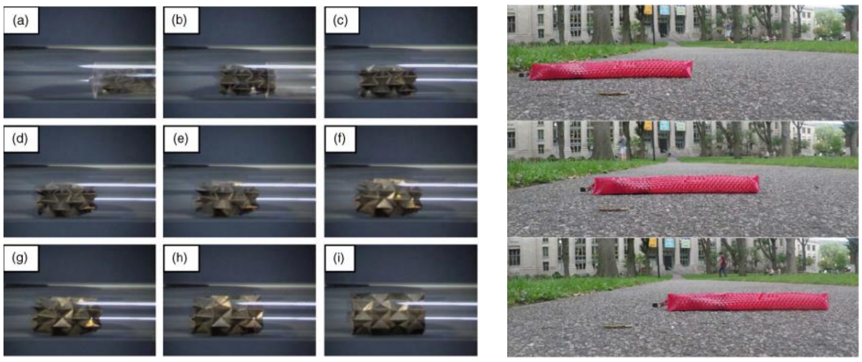


(a) (b)

**Figure 2:** (a) Origami application from [4]; (b) Kirigami application from [10]

## 2. Materials and Methods

The Isobe-Okumura kirigami configuration [6] was selected to this research due to its simple form (see Figure 3 for details). As we are dealing with large deformations, an elastomeric material was selected. Moreover, such material must be easy to make cuts and homogeneous. The Ethylene-vinyl acetate (EVA) is available worldwide with mechanical properties within certain limits. The EVA sheets have around 1.65 mm uniform thickness. The first step is tensile mechanical characterization. The ASTM D 412 [11] standard for thin films was selected. Once the stress-strain curve is obtained an elastoplastic approximation is made. This information will be used for finite element simulations through ANSYS. The next step is the kirigami manufacture and test under tensile load at constant displacement of 5 mm/mim using a EMIC DL1000 universal testing machine with load cell of 200N. To be able to evaluate the cut effect into the overall kirigami response the following W/d ratio were tested, i.e. 1.0, 1.5, 2.0, 3.0, 4.0, 6.0, 8.0. At least five specimens were tested for each W/d ratio. Numerical results and experimental data were compared and some correlations will be described.

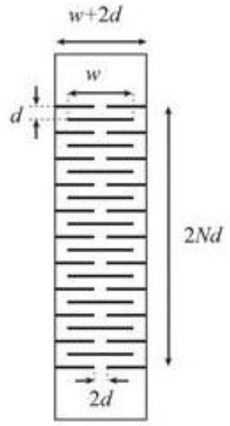


**Figure 3:** Configuration of Isobe-Okumura's Origami shape

## 3. Data Analysis

A representative EVA stress-strain tensile curve is shown in Figure 4A. The EVA behavior under tensile loadings is nonlinear, moreover it can be fitted to an elastoplastic bilinear or multi-linear formulation. Based on EVA's response to tensile loading, the kirigami behavior is expected to be also nonlinear. The stress-strain curve based on W/d ratio equals to 6 is shown in Figure 4B. The Kirigami configuration clearly changed the mechanical response as the two curves are completely dissimilar.

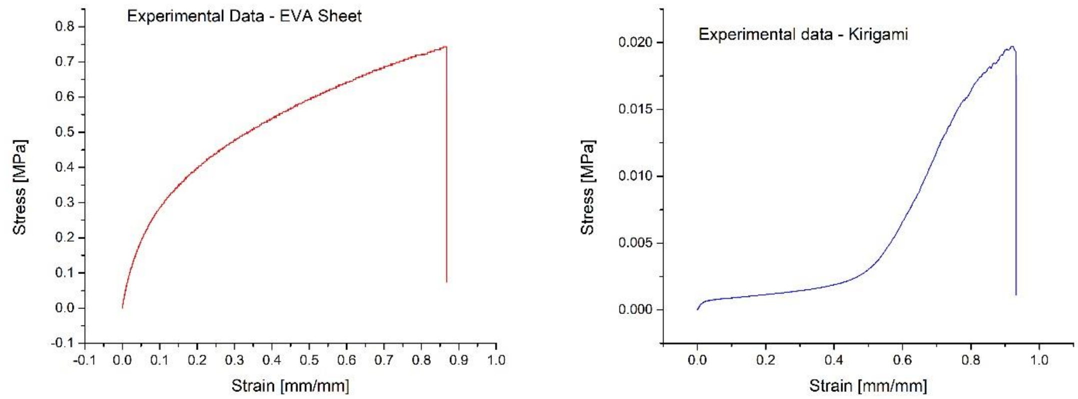


**(a)** **(b)**

**Figure 4:** Experimental Stress-strain curves. (a) EVA sheet. (b) Kirigami sheet

The kirigami configuration, cuts spatial distribution, must control the overall meta-structure response to loadings, in this case tensile loadings. Shuy et al [2] analysed this overall behaviour based on an approximation of the individual struts formed by kirigami as beams. However, the beam deflection analysis predicts the total critical force, but it does not take into account for deformation in buckling and torsion. The kirigami experimental response to uniaxial tensile loading can be described by different phenomena, i.e. local buckling and out-of-plane rotation. Note that such phenomena are trigger based on geometrical differences among the various kirigami configurations. Geometrical parameters such as cut width (*W*) and distance between cuts (*d*) can influence the overall response, as it can trigger local buckling and out-of-plane rotations. The first transition region, from the initial elastic regime to a nonlinear regime, is trigger by the critical buckling load. This transition is followed by a secondary elastic plateau. In this case, a dynamic phenomenon is evolving, where buckling occurs at the beams as they rotate to align with the applied load, and deformation occurs out of the plane of the sample. As discussed by Shyu et al. [2], the Kirigami's out-of-plane deformation can be attributed to a mechanical bistability condition. The final stage can be described by the alignment of the struts causes the overall structure to densify perpendicular to the pulling direction. Failure process begins when the ends of the cuts tear and crease owing to high stress at these regions. An illustrative representation of such response to tensile loading is shown in Figure 5.

.

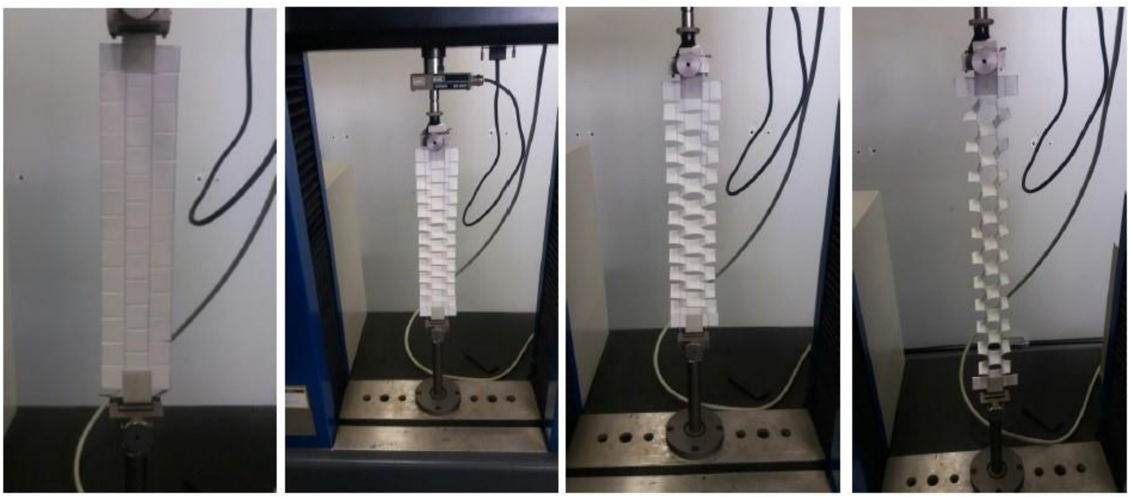

**Figure 5:** Kirigami deformation under tensile loadings.

Another important issue is the (*W/d*) ratio effect on failure loading and final deformation. As it can be observed in Figure 6, as the (*W/d*) ratio increases there is an increase of failure loading, while the total deformation decreases. This behavior is due to the buckling load increase, due to beam's changes on geometry.

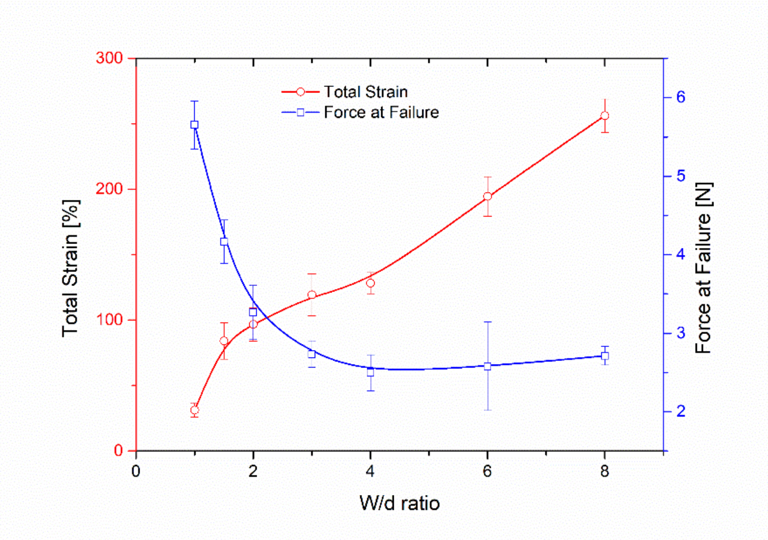


**Figure 6:** The (W/d) ratio effects on Kirigami's failure behavior.

## 4. Conclusions

The kirigami experimental response to uniaxial tensile loading can be described by different phenomena, i.e. local buckling and out-of-plane rotation. Geometrical parameters such as cut width (W) and distance between cuts (d) can influence the overall response, as it can trigger local buckling and out-of-plane rotations. The first transition region, from the initial elastic regime to a nonlinear regime, is trigger by the critical buckling load. This transition is followed by a secondary elastic plateau. In this case, a dynamic phenomenon is evolving, where buckling occurs at the beams as they rotate to align with the applied load, and deformation occurs out of the plane of the sample. The final stage can be described by the alignment of the struts causes the overall structure to densify perpendicular to the pulling direction. Failure process begins when the ends of the cuts tear and crease owing to high stress at these regions.


## Acknowledgement

The first author would like to acknowledge the financial support provided by the Brazilian Research Council (CNPq) under grant 304556/2018-1.


## References


[1] Surjadi, J. U., Gao, L., Du, H., Li, X., Xiong, X., Fang, N. X., Lu, Y. 2019. Mechanical metamaterials and their engineering applications, *Adv. Eng. Mater.*, 21, 1800864.

[2] Shyu, T.C., Damasceno, P.F., Dodd, P.M., Lamoureux, A., Xu, L., Shlian, M., Shtein, M., Glotzer, S.C., Kotov, N.A. 2015. A kirigami approach to engineering elasticity in nanocomposites through patterned defects. *Nature Materials*, 14, 785-790.

[3] Papa, A., Pellegrino, S. 2008. Systematically Creased Thin-Film Membrane Structures. *J. of Spacecraft and Rockets*, 45, 10-18.

[4] Kuribayashi, K., Tsuchiya, K., You, Z., Tomus, D., Umemoto, M., Ito, T., Sasaki, M. 2006. Self-deployable origami stent grafts as a biomedical application of Ni-rich TiNi shape memory alloy foil. *Mat. Sci. Eng. A.*, 419, 131-137.

[5] Yang, K., Xu, S., Shen, J., Zhou, S., Xie, Y.M. 2016. Energy absorption of thin-walled tubes with pre-folded origami patterns: Numerical simulation and experimental verification. *Thin Walled-Structures*. 103, 33-44.

[6] Isobe, M., Okumura, K. 2016. Initial rigid response and softening transition of highly stretchable kirigami sheet materials. *Scientific Reports*, 6, 24718.

[7] Hwang, D-G., Bartlett, M. D. 2018. Tunable Mechanical Metamaterials through Hybrid Kirigami Structures. *Scientific Reports*, 8, 3378.

[8] Rafsanjani, A., Bertoldi, K. 2017. Buckling-induced kirigami. *Physical Review Letters*. 118, 084301.

[9] Hu, N., Chen, D., Wang, D., Huang, S., Trase, I., Grover, H.M., Yu, X., Zhang, J.X.J., Chen, Z. 2018. Stretchable Kirigami Polyvinylidene Difluoride Thin Films for Energy Harvesting: Design, Analysis, and Performance, *Physical Review Applied*. 9, 021002.

[10] Rafsanjani, A., Zhang, Y., Liu, B., Rubinstein, S. M., Bertoldi, K. 2018. Kirigami skins make a simple soft actuator crawl. *Sci. Robot.*, 3, eaar7555.

[11] ASTM D412. 2016. Standard Test Methods for Vulcanized Rubber and Thermoplastic Elastomers—Tension, *ASTM International*, 15,1-8.

# Investigation of KI and KII stress intensity factor prediction in metal matrix composites using moiré interferometry

G. Plata Contreras, N. A. Fellows[a], J. F. Durodola[a]

[a]*Oxford Brookes University, Oxford, UK*

*E-mail address:* neil.fellows@brookes.ac.uk

**Abstract**

This paper uses Finite Element Analysis to investigate how well different analytical models, utilising moiré interferometry measurements of Crack Opening Displacements, predict Stress Intensity Factors (SIFs) in Titanium Metal Matrix Composites (Ti-MMC) subject to Mode I and Mode II loading. The development of lightweight MMC's has been driven by the aerospace industry that has been looking for high stiffness to low weight materials. These materials, which tend to be used within the engine, are subjected to load and thermal cycles. During bending mixed mode fatigue crack growth occurs in these materials due to off axis crack propagation. Solutions for predicting the SIFs for Ti-MMC under these load conditions have not been carried out before and presents difficulties, both analytically and experimentally. There are several methods to measure the COD during the fatigue crack propagation, but these techniques have limited measuring capabilities. However, the Moiré interferometry technique gives very sensitive and detailed data, due to its ability to measure the full field displacements near the crack tip. This method has therefore been used to determine the COD of a Textron SCS-6/Ti-6-4 MMC subject to four point bending. The results presented are unique in that very little data on SIFs in Ti-MMC material is available and the ability of analytical methods to predict KI and KII SIFs for these types of materials has not been addressed until now.

***Keywords****:* SIF; MMC; Titanium; COD; Fatigue

## 1. Introduction

During fatigue crack growth of Ti-MMC's, the presence of two off-axis cracks have been reported [1-8]. When two cracks grow off-axis, the crack growth is driven by both Mode I and Mode II. In composite materials like Ti-MMC the SIFs calculated using Linear Elastic Fracture Mechanics (LEFM) will predict crack growth although crack retardation occurs. It is believed that this difference is caused by the real SIFs in the material being affected by fibre bridging, multiple cracks and curvature in the crack path. Currently there is no experimental work or numerical predictions to show whether this is true.

## 2. Experimental Procedure

The experimental procedure is divided into three sections (material characteristics, specimen preparation and moiré interferometry)

### *2.1. Material Characteristics*

The material tested in this work was titanium $\alpha+\beta$ dual phase Ti-6-4 alloy matrix, reinforced with Textron SCS-6 silicon carbide fibre (SCS-6/Ti-6Al-4V); supplied by Roll Royce, Derby. The fibre diameter was 140 μm and the fibre volume fraction was ~40%. The composite sheet had a thickness of ~1.57 mm with eight unidirectional fibre layers. The mechanical properties are shown in Table 1.

### *2.2. Specimen preparation*

Single edge notch (SEN) specimens were used in a Four Point Bend (4PB) configuration for the fatigue tests and were divided into four types [9], one of which is presented in this paper (Figure 1 and Table 2).

An electro discharge machine was used to make 0.5mm wide notches with 0.5mm semi-circular notch profiles. This process was used to avoid generating residual stresses around the crack tip. The specimen surfaces near to the notch were polished and 0.2mm cross perpendicular lines drawn to facilitate the visualisation of the crack's propagation. The SCS-6/Ti-6Al-4V was tested in the as received condition.

**Table 1**. Mechanical Properties of SCS-6/Ti-6-4 [10]

| | | |
|---|---|---|
| Tensile modulus of fibre | $E_f$ | 400 GPa |
| Tensile modulus of matrix | $E_m$ | 110 GPa |
| Shear modulus of matrix | $G_m$ | 73 GPa |
| Tensile modulus of composite | $E_c$ | 230 GPa |
| Poisson's ratio for fibre | $\nu_f$ | 0.25 |
| Volume Fraction of fibre | $V_f$ | 0.40 |
| Volume Fraction of matrix | $V_m$ | 0.60 |
| CTE of fibre | $\alpha_m$ | $5x10^{-6}/^oC$ |
| CTE of matrix | $\alpha_f$ | $10x10^{-6}/^oC$ |

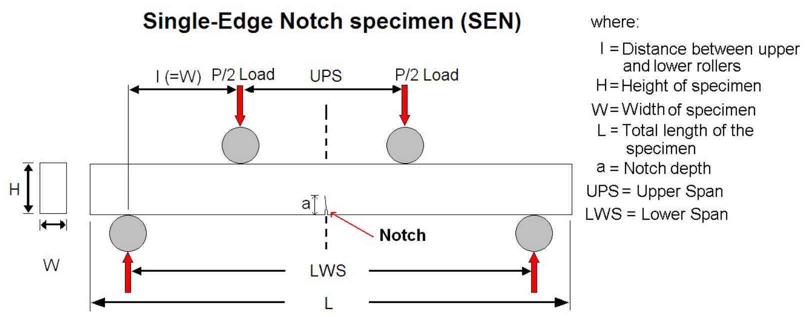


**Figure 1.** Single-Edge Notch specimen for four point bending load configuration (SEN)

**Table 2.** Dimensions of the SEN specimens

| SEN specimen type | Length mm L | Height mm H | Width mm W | Notch deep mm | Upper Span mm UPS | Lower Span mm LWS | Material |
|---|---|---|---|---|---|---|---|
| D | 75 | 10 | 1.58 | 0.5 | 30 | 70 | Steel and Ti-MMC |

### *2.3. Moiré interferometry*

The glass master method, developed by Post *et al.* [11] was used to create 1200 lines per mm moiré diffraction gratings on the specimen faces. The specimens were then placed in a 4 point bend and moiré interferometer rig, attached to a servo-pneumatic fatigue machine. The moiré system used in this work was a Four-Beam optical arrangement with a three-mirror system. The specimen was loaded several times before measurements were taken, with the aim of propagating the crack in the aluminium grating and localizing the crack tip. After this, a null field was created at zero load by adjusting the mirrors.

Then the maximum load was applied to the specimen and five interferograms were captured, rotating the optical flat by a small angle between each one. The rotation of the optical flat stage was made using a rack and pinion gear utilising a Vernier micrometer to enable the rotation to be determined. The interferograms were captured, using a CCD camera, personal computer and frame grabber software.

## 3. Analytical Methods

Two methods were found in literature that investigated the SIF's for combined Mode I and Mode II loading on cracks. These methods are discussed below.

### *3.1. Method one*

MacKenzie *et al*. [12] proposed a solution to calculate mixed mode *KI* and *KII* using $U_1$ and $U_2$ displacements at the crack tip (*x* along crack direction and *y* perpendicular to crack direction) as given in equations 1 and 2

$$KI_{m1} = (FU_2 - CU_1) / A(BF - CD) \tag{1}$$

$$KII_{m1} = (BU_1 - DU_2) / A(BF - CD) \tag{2}$$

where $A=(1/2G)(r/2\pi)^{1/2}$, $B=\cos\frac{1}{2}\theta[k-1+2\sin^2\frac{1}{2}\theta]$, $C=\sin\frac{1}{2}\theta[k+1+2\cos^2\frac{1}{2}\theta]$, $D=\sin\frac{1}{2}\theta[k+1-2\cos^2\frac{1}{2}\theta]$, $F=-\cos\frac{1}{2}\theta[k-1-2\sin^2\frac{1}{2}\theta]$, r is the radial distance from the crack tip, θ is the angle relative to the a line running from the crack tip in direction to point r, G = 0.5 E /(1+ν ), $k=3-4\nu$ for plane stress and $k=(3-\nu)/(1+\nu)$ for plane strain and $\nu$ is the Poisson ratio..

Thus, $KI_{m1}$ and $KII_{m1}$ can be calculated as functions of $r$, $\theta$, $U_2$ and $U_1$, using the experimental measurement of the displacements field components at $\theta = 90^o$ and 0° (relative to a chosen direction).

*3.2 Method two*

Feng *et al.* [13] used the Crack Opening Displacement (COD) and the Crack Shear Displacement (CSD) to calculate the SIF values $KI_{m1}$ and $KII_{m2}$ in mixed mode conditions as given in equations 3 and 4

$$KI_{m2} = \frac{COD \times E\sqrt{\pi a}}{4a\sqrt{1-\left(\frac{r}{a}\right)^2}} \tag{3}$$

$$KII_{m2} = \frac{CSD \times E\sqrt{\pi a}}{4a\sqrt{1-\left(\frac{r}{a}\right)^2}} \tag{4}$$

where $E$ is the Young's modulus, $r$ is the distance from the crack tip and $a$ is the crack length. The COD and CSD relative displacements are given by equations 5 and 6 [14]

$$COD = \frac{4\sigma a}{E^*}\sqrt{1-\left(\frac{x}{a}\right)^2} \tag{5}$$

$$CSD = \frac{4\tau a}{E^*}\sqrt{1-\left(\frac{x}{a}\right)^2} \tag{6}$$

where $E^* = E$ for plane stress and $E^*=E/1-\nu^2$ for plane strain, $\sigma=\sigma_0 \cos\alpha$, $\tau=\sigma_0\cos\alpha\sin\alpha$, $\sigma_0$ is the specimen applied bulk stress, α is the notch angle relative to the shear stress direction and x is the crack opening displacement perpendicular to the crack face at point r.

In order to calculate the SIF the KI and KII, the values are plotted against the distance from the crack tip $r$. The extrapolation of these values to $r = 0$ gives the SIF.

## 4. FEA model

During fatigue loading of 4pt bend SEN SCS-6/Ti-6-4 specimens two cracks will develop from the notch. Due to the difficulty in replicating this phenomenon in non-composite materials it was decided to create a FEA model with the same specimen geometry and loading but utilising isotropic material properties and introducing two 30 º off axis cracks symmetrical around the notch specimen centre line. The COD, CSD and displacements $U_1$ (parallel to crack) and $U_2$ (perpendicular to crack) along six different directions from the crack tip were obtained from the FEA. The KI and KII SIFs were then calculated using the data with the two analytical methods and compared with SIFs obtained using the J-integral method.

## 5. Results

The J-Integral SIF results and the SIF results using method one and method two (with displacements used parallel and perpendicular to the crack face) from the two-crack isotropic FEA model are presented in table 3.

**Table 3.** Comparison of analytical method one using FEA and J-Integral using FEA for the KI and KII SIFs

| | FEA Analytical Method One | | FEA Analytical Method two | | FEA J-Integral |
|---|---|---|---|---|---|
| | Plane Strain | Plane Stress | Plane Strain | Plane Stress | |
| KI | 1.04E07 | 9.71E06 | 1.04E07 | 9.72E06 | 9.97E06 |
| KII | 1.82Eo6 | 1.70E06 | 1.62E06 | 1.52E06 | 1.78E06 |

The results for a SEN SCS-6/Ti-6-4 specimen using the analytical methods and data obtained from the moiré interferometry are shown in table 4.

**Table 4.** KI and KII SIFs obtained from analytical method one using moiré displacements along the left and right crack faces and analytical method two using moiré COD and CSD measurements.

| | FEA Analytical Method One (left side of crack face) | | FEA Analytical Method One (right side of crack face) | | FEA Analytical Method Two | |
|---|---|---|---|---|---|---|
| | Plane Strain | Plane Stress | Plane Strain | Plane Stress | Plane Strain | Plane Stress |
| KI | 1.69E08 | 1.41E08 | 4.50E07 | 3.75E07 | 2.45E07 | 2.30E07 |
| KII | 6.76E07 | 5.63E07 | -2.50E07 | -3.00E07 | -8.44E06 | -7.92E06 |

## 6. Discussion

The parallel and perpendicular displacements (along the crack face) gave the closest SIF results for method one in comparison to the J-Integral method. Method two, the J-Integral method and method one (using the displacement along the crack face) all gave very similar SIFs when using results from the two-crack isotropic FEA model (Table 3).

When using moiré displacement data from a SCS-6/Ti-6-4 specimen the methods do not agree with one another for either KI or KII SIFs (Table 4). This uncertainty means that it is not clear whether either method is reliable. To overcome this further work will be carried out create a 3D FEA model to evaluate the reliability of the methods for use with Ti-MMC materials and to look at the changes in the predicted Ti-MMC SIF values during crack growth.


## Acknowledgements

The authors would like to acknowledge the support of Rolls Royce, Derby, UK, who supplied the test materials.


## References


[1] P. Bowen, A.R. Ibbotson, C.J. Beevers, Fatigue crack-growth in continuous fiber reinforced titanium-alloy metal matrix composites, 1992.

[2] S.M. Jeng, P. Alassoeur, J.M. Yang, Fracture mechanisms of fiber-reinforced titanium-alloy matrix composites .5. Fatigue crack-propagation, Materials Science and Engineering a-Structural Materials Properties Microstructure and Processing 154(1) (1992) 11-19.

[3] S.M. Jeng, P.C. Wang, J.M. Yang, Fatigue Damage Evolution and Degradation of Mechanical Properties in Silicon-Carbide (SiC) Fiber-Reinforced Titanium Matrix Composites, in: S. Johnson, J. Larsen, B. Cox (Eds.), ASTM International, West Conshohocken, PA, 1996, pp. 377-394.

[4] C. Barney, C.J. Beevers, P. Bowen, Fatigue-crack growth in sic continuous fiber-reinforced Ti-6Al-4V alloy metal-matrix composites, 1993.

[5] A.R. Ibbotson, C.J. Beevers, P. Bowen, Damage assessment and lifting of continuous fiber-reinforced metal-matrix composites, Composites 24(3) (1993) 241-247.

[6] R. John, J.R. Jira, J.M. Larsen, N.E. Ashbaugh, Analysis of bridged fatigue cracks in unidirectional SCS/6/Ti-24Al-11Nb composite, 1993.

[7] J.M. Larsen, J.R. Jira, R. John, N.E. Ashbaugh, Crack-Bridging Effects in Notch Fatigue of SCS-6/TIMETAL 21S Composite Laminates, in: S. Johnson, J. Larsen, B. Cox (Eds.), ASTM International, West Conshohocken, PA, 1996, pp. 114-136.

[8] Y. Akiniwa, T. Fujii, H. Kimura, K. Tanaka, Evaluation of fibre bridging stress of short fatigue cracks in SCS-6/Ti-15-3 composite, Fatigue & Fracture of Engineering Materials & Structures 30(3) (2007) 258-266.

[9] P.C. Gerrado, Evaluation of stress intensity factors in metal matrix composites, Department of Mechanical Engineering and Mathematical Sicences, Faculty of Technology Design and Envioroment, Oxford Brookes University, Oxford 2007.

[10] L. Davidson, The micromechanics of fatigue crack growth at 25oC IN Ti-6Al-4V reinforced with SCS-6 fibres, Metallurgical and Materials Transactions Vol. 24A (1992) 865-879.

[11] D. Post, B. Han, P. Ifju, High sensitivity moire interferometry : experimental analysis for mechanics and materials, Springer-Verlag, New York, 1994.

[12] P.M. Mackenzie, C.A. Walker, R. Giannettoni, A technique for experimental evaluation of mixed-mode stress intensity factors, International Journal of Fracture 62(2) (1993) 139-148.

[13] H. Feng, J. Zhang, J. Rohde, Crack surface relative displacement analysis of mixed-mode fracture-mechanics problems, Engineering Fracture Mechanics 36(6) (1990) 971-978.

[14] I.N. Sneddon, M. Lowengrud, Crack Problems in the Classical Theory of Elasticity, John Wiley, New York, 1969

# Finite element model for fatigue crack growth in cold hole expanded specimens

A. Hernández[a], D. E. Sánchez[b], C. García[a*], R. R. Ambriz[b]

[a] *Facultad de Ingeniería, Universidad Autónoma de San Luis Potosí, Av. Dr. Manuel Nava No. 8, Zona Universitaria Poniente, C.P. 78290, San Luis Potosí, S.L.P., México.*
[b] *Instituto Politécnico Nacional CIITEC-IPN, Cerrada de Cecati S/N, Col. Sta. Catarina, C.P. 02250, Azcapotzalco, Ciudad de México, México.*

*E-mail address: garcia.ch@uaslp.mx*

**Abstract**

Cold expanded specimens are regularly used by the aerospace industry, because the fatigue life resistance is regularly improved. Fatigue crack growth analysis in cold expanded specimens is cumbersome because of the variable residual stress distribution. In this work, the induced 3-D residual stress by a cold hole expansion procedure in 6061-T6 Al alloy were analysed via a submodeling FE technique, which uses three levels corresponding to a global model, intermediate and fine submodels. The FE residual stress and strain results produced by the expansion procedure were set as an initial condition for a subsequent simulation of a fatigue crack growth process, where the FE submodeling technique was also used. Effective stress intensity factors were determined from the FE models and the Paris-Erdogan relationship was used to determine *da*/*dN* rates. The FE results were compared against experimental results from fatigue crack growth tests in the aluminium alloy 6061-T6. The numerical *da*/*dN* rates exhibited a good correlation with the experimental results, especially for a region close to the expanded-hole bore where the FE submodeling technique allowed to resolve the variable residual stresses.

***Keywords:*** Fatigue crack growth, cold hole expansion, residual stress, FE submodeling technique, effective stress intensity factor.

## 1. Introduction

Manufactured holes in aircraft fastened joints are regularly subjected to cold hole expansion procedures, because the experience shows larger fatigue life cycles in cold expanded holes than as-manufactured ones [1-2]. The expansion is a quasi-static procedure, where a gradual interference between the hole bore and expansion tools results in non-uniform residual stress fields through the thickness of the component. Several models have been developed to analyze the fatigue crack propagation in cold expanded specimens. The majority have been based on a combination of the linear-elastic fracture mechanics and the superposition method. This approach combines empirical fatigue crack growth relationships and a total stress intensity factor that combines applied loads and post-cold expanded residual stresses [3-4]. Other approaches incorporate crack closure effects for the evaluation of an effective stress intensity factor, where post-cold expanded residual stresses influenced the crack opening stresses. The simulation of the induced-plasticity fatigue crack closure is also largely used for the determination of the crack opening stresses [5-6]. Despite the different approaches and parameters used for the fatigue crack growth analysis in cold expanded components, the numerical results have shown a poor correlation with the experimental fatigue crack growth behavior [7-8]. Experimental results exhibited fatigue crack growth arrest and restarts [7], which are not captured by the superposition or effective stress intensity factor methods. The poor correlation can be directly related with absence of the residual strain/stress history, which is variable along the thickness of the cold hole expanded components.

This manuscript presents a novel method for the fatigue crack growth analysis in cold expanded specimens with variable residual stresses. The method proposed a revised definition for the effective stress intensity factor, which implicitly considers the residual strain/stress history as a function of the fatigue crack growth process rather than just post-cold expanded residual stresses for an uncracked geometry.

## 2. Finite element submodeling

3-D Finite Element (FE) models were created to determine the residual stresses induced by a cold hole expansion operation. The FE models were developed in the commercial-available software ABAQUS™. A direct mandrel expansion was simulated by passing a tapered mandrel through a center-hole-plate geometry. The largest diameter in the tapered mandrel produced a 4% cold hole expansion. The plate geometry were

200 mm length, by 100 mm width, and 6.35 mm thick, and the drilled circular hole at its centre were of 6.35 mm diameter. The material model was an elastic-plastic with a combined strain hardening behaviour. The material parameters were standard values for a 6061-T6 Al alloy. Symmetry conditions were used, thus, the FE models were only a quarter region of the drilled hole plate. Eight-node linear brick elements were used in the FE meshes with a reduced integration scheme. The large residual stress gradients induced by the cold hole expansion around the hole bore were captured by using the FE submodeling technique. Three levels were used corresponding to the global FE model, intermediate and fine FE submodels. The average mesh sizes were 0.264, 0.159 and 0.019 mm, respectively. Figure 1 presents the relative position between FE models for the global and submodel regions, the different FE meshes used, and the tapered mandrel used for the cold hole expansion simulation.

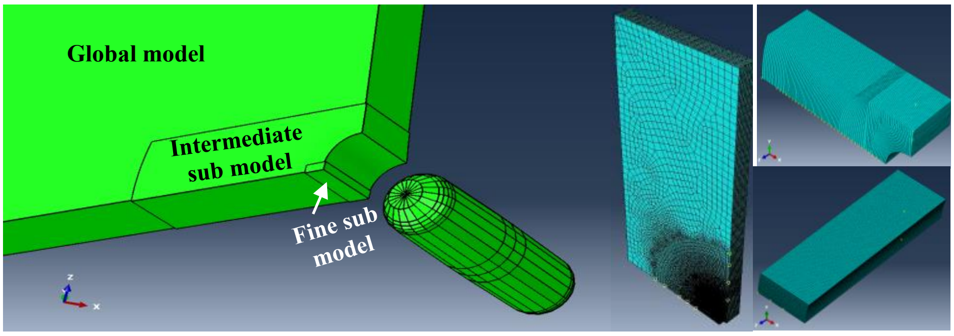


Figure 1. Global and submodel regions and the FE meshes. The expansion tool is also shown.

## 3. Fatigue crack growth simulation

The post-cold expanded residual strain and stress were used as an initial condition for the fatigue crack growth simulation. Through-the-thickness cracks were introduced into the FE meshes (global model and submodels) by releasing the nodes corresponding to the crack face. The initial crack length measured from the center of the hole was of 4 mm. Mode I cyclic loading were prescribed to the far end of the global FE model. The cyclic loading conditions were set to replicate the experimental conditions reported in the literature for fatigue crack growth tests of cold hole expanded specimens made from 6061-T6 Al alloy [9]. The corresponding maximum cyclic load was 39 kN and the stress ratio was of 0.1. A re-mesh strategy was used for the fatigue crack growth simulation. The initial crack length was 4.0 mm, the final crack length was 19 mm, and intermediate crack lengths analyzed were 6.0, 8.0, 12.0 and 16.0 mm.

## 4. Results and discussion

Figure 2 shows the FE results for the residual stress distribution induced by the cold hole expansion. Figure 2a presents the distribution at the entrance and exit faces of the plate, and at its mid-plane thickness according to the intermediate FE submodel. Larger compressive residual stresses at the hole bore were determined at the mid-plane thickness and exit face of the plate with respect to the entrance face. The compressive values were ~300 MPa, ~260 MPa and ~145 MPa, respectively. Figure 2b presents the residual stress distribution determined by the global model, intermediate and fine submodels at the entrance face of the plate. The residual stress distribution was almost identical between the global model, intermediate and fine submodels for distances of 5 mm and beyond from the hole edge. However, larger differences were observed in the residual stress distribution from the hole bore up to 2 mm distance between the global model, intermediate and fine submodels. The corresponding compressive residual stresses at the hole bore were ~165, 145 and 100 MPa, respectively. Thus, the severity of the compressive residual stresses were overestimated by a 65% in the global FE model, and by a 45% in the intermediate FE submodel. The three-level FE models shows an increasing compressive residual stress region from the hole edge up to 2.5 mm, followed by a decreasing compressive residual stress up to 5 mm where the residual stress changed to an increasing tensile condition up to 6 mm, afterwards the residual stress decreased towards a value of 10 MPa at approximately 23 mm. The maximum compressive residual stress value for the three-level submodels was around 205 MPa at 2.5 mm while the maximum tensile RS for the three-level submodels was approximately 60 MPa at 6 mm. As observed in Figure 2b, the results captured by the fine FE submodel are not continuous along the whole distance from the hole edge, because the fine FE submodel were discretely used for the specific fatigue crack lengths of 4.0, 6.0, 8.0, 12.0, 16.0 and 19.0 mm.

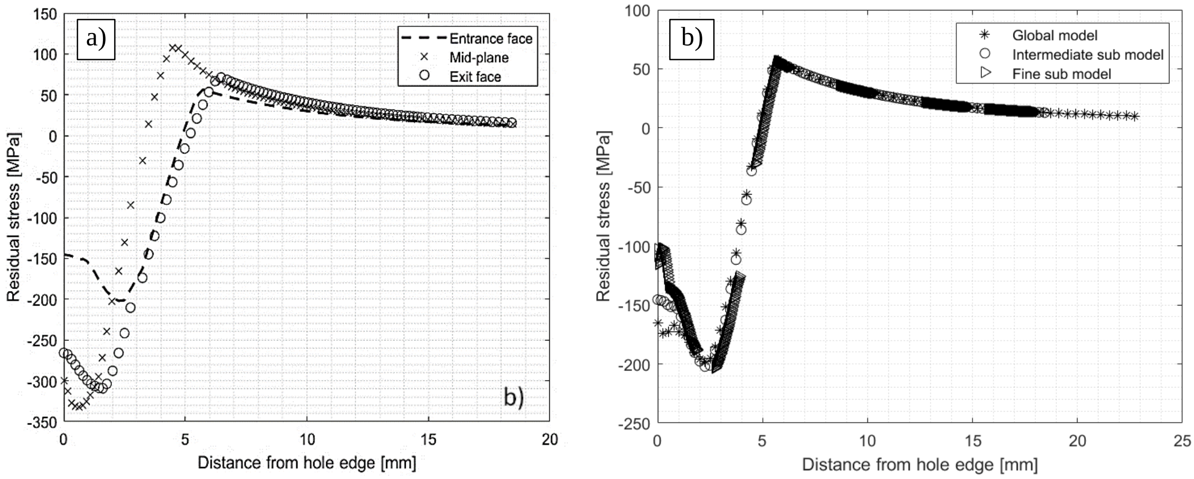


Figure 2. a) FE residual stress distribution induced by the cold hole expansion at the entrance face, mid-plane thickness and exit face of the 6061-T6 Al alloy, and b) comparison between the global FE model, intermediate and fine FE submodels for the residual stress distribution.

The residual stress differences between the global FE model, the intermediate and fine FE submodels were very significant, which also represented quite different effective *K*-values estimations. Therefore, the fatigue life predictions are very sensible to slight changes on the predicted residual stress field. Table 1 shows the differences of calculating the effective $\Delta K$-values on a 4 mm cracked center-hole-plate model with the three-level different models. Moreover, Table 1 shows the corresponding fatigue crack growth rates $da/dN$ for the $\Delta K$-values. The corresponding $da/dN$-values were estimated through the Paris-Erdogan empirical relation, where material coefficients reported from the literature for 6061-T6 Al alloy were used [10].

Table 1. Comparative results for the effective $\Delta K$ and $da/dN$ rate values from the global FE model, and intermediate and fine FE submodels.

| FE model | Effective $\Delta K$ $[MPa\sqrt{m}]$ | $\frac{da}{dN}, \left[\frac{mm}{cycle}\right]$ |
|---|---|---|
| Global model | 10.956 | 1.1231e-04 |
| Intermediate sub model | 5.6519 | 1.2476e-05 |
| Fine sub model | 3.1457 | 1.7832e-06 |

According to the information presented on Table 1, the $da/dN$-values differ from one another, depending on the FE model level, by a magnitude order. The less conservative $da/dN$ value was estimated by the global model, as it was the fastest fatigue crack growth rate. Contrary, the more conservative $da/dN$ value was predicted by the fine submodel as it was the slowest fatigue crack growth rate. In other words, regarding the fatigue life estimations, the cycles required for a 0.5 mm crack length increment ($\Delta a$ = 0.5) would be: 4452, 40077 and 280395 cycles for the global model, intermediate and fine submodels, respectively. The global model is underestimating the cycles required for the 0.5 mm crack increment by approximately 63 times regarding the fine submodel.

Figure 3 presents the computed $da/dN$ values determined by the fatigue crack growth simulation based on the fine FE submodel, along with corresponding experimental results [9]. A good correlation was observed between the computational and the experimental results. Specially, for the region close to the hole bore, where a large gradient was presented for the post-cold hole expanded residual stresses. The largest portion of the fatigue life for cold hole expanded components is expended in the region close to the hole bore, where a large number of cycles are consumed in the fatigue crack initiation process.

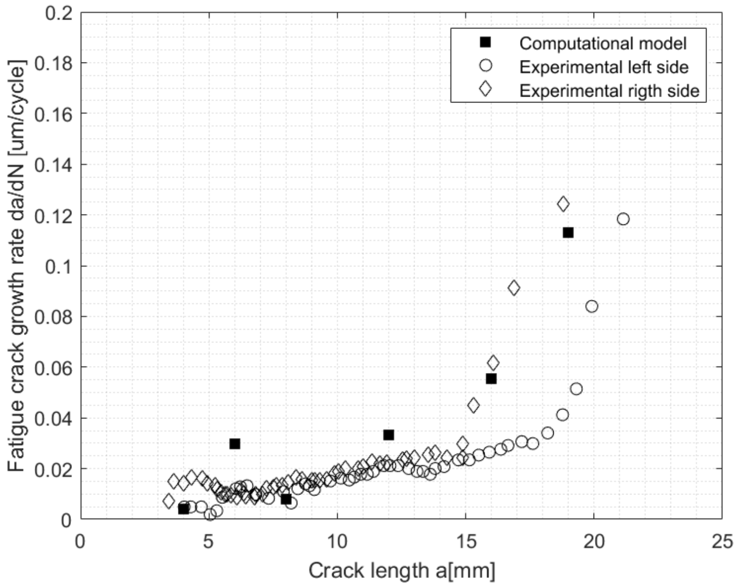


Figure 3. Fatigue crack growth rate as a function of the crack length for a cold hole expanded component.

## 5. Conclusions

The FE submodeling technique was used to determine the residual stresses induced to a drilled hole by the cold hole expansion procedure. A 2 mm annular region from the expanded hole bore presented remarkably differences in the residual stress distribution according to the FE model lever (global, intermediate and fine). The corresponding compressive residual stresses at the hole bore were ~165, 145 and 100 MPa, respectively. Differences in the residual stress distribution resulted in *da*/*dN* values dependent upon the FE model level. Fastest crack growth rates were determined by the global FE model, and the slowest ones were determined by the fine FE submodel. The slowest *da*/*dN* values determined by the fine FE submodel presented a good correlation with corresponding experimental results, specially for the 2 mm annular region close to the expanded hole bore.

## References


[1] S. Pasta, "Fatigue crack propagation from a cold-worked hole," Eng. Fract. Mech., vol. 74, no. 9, pp. 1525–1538, 2007.

[2] G. Clark, "Modelling Residual Stresses and Fatigue Crack Growth At Cold-Expanded Fastener Holes," Fatigue Fract. Eng. Mater. Struct., vol. 14, no. 5, pp. 579–589, 1991.

[3] X. R. Wu, X. C. Zhao, W. Xu, and D. H. Tong, "Discussions on weight functions and stress intensity factors for radial crack(s) emanating from a circular hole in an infinite plate," Eng. Fract. Mech., vol. 192, no. February, pp. 192–204, 2018.

[4] B. F. Jogi, P. K. Brahmankar, V. S. Nanda, and R. C. Prasad, "Some studies on fatigue crack growth rate of aluminum alloy 6061," J. Mater. Process. Technol., vol. 201, no. 1–3, pp. 380–384, 2008.

[5] K. Solanki, S. R. Daniewicz and J.C. Newman Jr., "Finite element analysis of plasticity-induced fatigue crack closure: an overview", Eng. Fract. Mech., vol. 71, pp. 149-171, 2004.

[6] P. F. P. De Matos and D. Nowell, "Analytical and numerical modelling of plasticity-induced crack closure in cold-expanded holes," Fatigue Fract. Eng. Mater. Struct., vol. 31, no. 6, pp. 488–503, 2008.

[7] V. D. Lacarac, A. A. Garcia-Granada, D. J. Smith, M. J. Pavier, "Prediction of the growth rate for fatigue cracks emanating from cold expanded holes", Int. J. Fatigue, vol. 26, no. 6, pp. 585-595, 2004.

[8] K. W. Jones, M. L. Dunn, "Predicting corner crack fatigue propagation from cold worked holes", Int. J. Fatigue, vol. 76, no. 13, pp. 2074-2090, 2009.

[9] J. L. Cuevas, "Influencia de los esfuerzos residuales en la morforlogía de crecimiento de grieta por fatiga en Al 6061-T6", M.S. Thesis, Instituto Tecnológico de Pachuca, Pachuca, 2017.

[10] R. R. Ambriz, G. Mesmacque, A. Ruiz, A. Amrouche, V. H. López, N. Benseddiq, "Fatigue crack growth under constant amplitude loading of Al-6061-T6 welds obtained by modified indirect electric arc technique", Sci Technol Weld JOI, vol. 15, no. 6, pp. 514-521, 2010.

# Effects of laser shock peening on fatigue crack behaviour in aged duplex steel specimens

V. Granados-Alejo[1,3*], C. Rubio-González[1], A. Ruiz[2], A. Banderas-Hernández[1], P. de los Santos-Lara[3].

[1] *Centro de Ingeniería y Desarrollo Industrial, Pie de la cuesta 702, Desarrollo San Pablo, Querétaro, Qro., 76130, México*
[2] *Instituto de Investigaciones en Metalurgia y Materiales, UMSNH, Morelia, Michoacán; México*
[3] *Universidad Politécnica de Guanajuato, Av, Universidad Sur 1001 Juan Alonso, 38496 Cortazar, Guanajuato, Mexico*

*E-mail address:* vgrandos@posgrado.cidesi.edu.mx

**Abstract** (max. 200 words)

Laser Shock Peening (LSP) is a technique for improving fatigue strength in metal alloys by introducing a compressive residual stresses field. In the open literature, very few studies have reported the effect of LSP on specimens with thermal aging. The objective of the present research is to evaluate the effect on fatigue life and fracture in specimens of aged 2205 duplex stainless steel. The technology implemented to perform the surface treatments consists of a Nd:YAG pulsed laser system operating with a frequency of 10 Hz; a fundamental wavelength of 1064 nm and a pulse density of 2500 pulses/cm$^2$ were used, releasing an energy of 1 J/pulse. The compact tension specimens were machined and thermally aged with four different holding times; then an area of 2.5 cm$^2$ was treated with LSP in both faces. Fatigue tests were performed on a MTS 810 servo-hydraulic system at room temperature, the load ratio used was R = 0.1 with a frequency of 20 Hz. A 6 DOF anthropomorphic robot industrial was used for moving the specimen and producing the desired pulse density and swept direction. An improvement on fatigue crack growth was obtained in specimens with LSP treatment. An analysis of the fracture surface by SEM microscopy was performed and beneficial influence of the residual stress fields on the zone of stable growth is observed by decrease fatigue crack growth and on the other hand is visible the negative influence of thermally aged.

***Keywords**:* LSP; Duplex Stainless Steel; Fatigue; Fracture; SEM microscopy.

## 1. Introduction

Laser Shock Processing (LSP) has been successfully utilized for extending the fatigue life of critical engineering components. Through LSP it is possible to delay the fatigue cracks initiation and growth by introducing a compressive residual stress field into specific areas such as stress raisers. Potential applications are directed to aerospace, automotive and power industries. Static, cyclic, fretting fatigue and stress corrosion performance are some properties that have been improved by LSP for different materials [1-3]. According with the iteration of radiation with matter, the laser beam is directed and focused on the sample surface as shown in Figure 1. When it contacts the surface, a thin layer of the surface is vaporized and due to the high concentration of energy in a reduced area, the temperature is increased and the medium is ionized, giving rise to the formation of plasma. Over time, the plasma expands and generates a high pressure on the material surface in the order of GPa [4]. This pressure transmits shock waves into the material by plastically deforming the surface and inducing a compression residual stresses field.

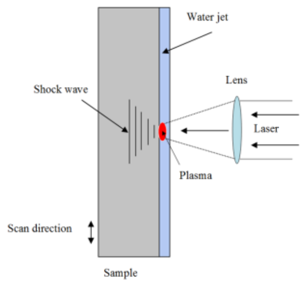


**Figure 1**: Laser shock penning principle

## 2. Methodology

A plate 12.7 mm thick of 2205 DSS with the chemical composition: 0.022 C, 23.4 Cr, 5.75 Ni, 3.238 Mo, 0.272 Cu, 0.882 Mn, 0.407 Si, 0.16 N, 0.011 S, was used in this study. The mechanical properties of the samples were determined by tensile tests using dog-bone type specimens. The offset tensile yield stress was 520 MPa, ultimate tensile strength was 710 MPa and elastic modulus was 190 GPa. For the fatigue experiments, compact tension specimens are used, with dimensions as illustrated in Figure 2. All fatigue crack growth tests specimens were machined with the loading axis parallel to the rolling direction. The dimensions of the specimens and pulse swept direction which is perpendicular to the specimen longitudinal axis are shown in Figure 2. The specimens were heat treated, during the 15, 60, 360 and 1440 min times at 750 ° C and tempered in water at room temperature 21 ° C. Research related are few [5-8].

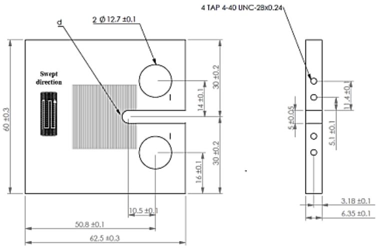

**Figure 2**: Geometry of compact tension specimens used for crack growth test.

The LSP experiments were performed using a Q switched Nd:YAG laser operating at 10 Hz with a wavelength of 1064 nm, the FWHM of the pulses was 10 ns. A convergent lens was used to deliver 1 J/pulse. Spot diameter was 1.3 mm with a power density of 7.55 GW/cm$^2$. Pulse density was 2500 pul/cm$^2$. A special device to produce a controlled water jet was implemented to form a thin water layer on the sample to be treated. Figure 3 shows the experimental set-up used in this study. The treatment was performed without protective coating. A 6 d.o.f. robotic arm was used to control specimen position and generate the desired pulse swept and treated area was 25x25 mm on both sides. For fatigue crack growth test a pre-crack 3 mm long was made in specimens after LSP treatment.

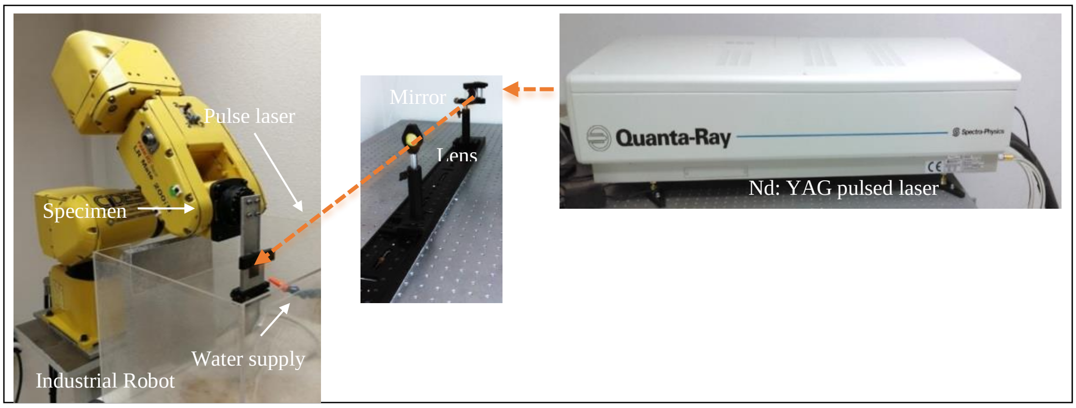


**Figure 3**: Set up of array of laboratory.

## 3. Results

Fatigue crack growth in thermally aged and LSP treatment is shows in Figure 4, it is observed that fatigue crack growth rate increases considerably specially for 30 min and 1440 min thermal aging time.

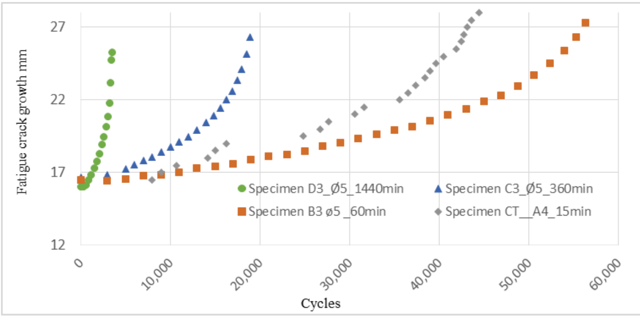


**Figure 4** Fatigue crack growth specimens with thermal damage and LSP.

The Figures show the various stages of the fracture, such as the beginning of the crack, stable growth and ductile fracture. Regarding fractography, the beginning of crack in specimens with aging time of 15 min and 60 min, has a tendency to start in the center of the specimen. On the other hand, there is a greater area of stable growth in relation to the specimens aged 300 and 1440 min. Specimens with aging time of 15 min and 60 min there is a tendency to start in the center of the specimen Figure 5 (a), 5 (d), Figure 5 (b), 5 (e) shows fatigue crack growth stable zone, ductile fracture can see in the Figure 5 (c), 5 (f). Effect of residual stress in fracture surface is similar to [9].
An important feature is observed in the transition zone from stable growth to ductile fracture there is greater growth in the center of the specimens and less in the area near the edges; a curvature is observed on the fatigue crack front this is a consequence of the influence of residual compression stress induced by the LSP treatment.

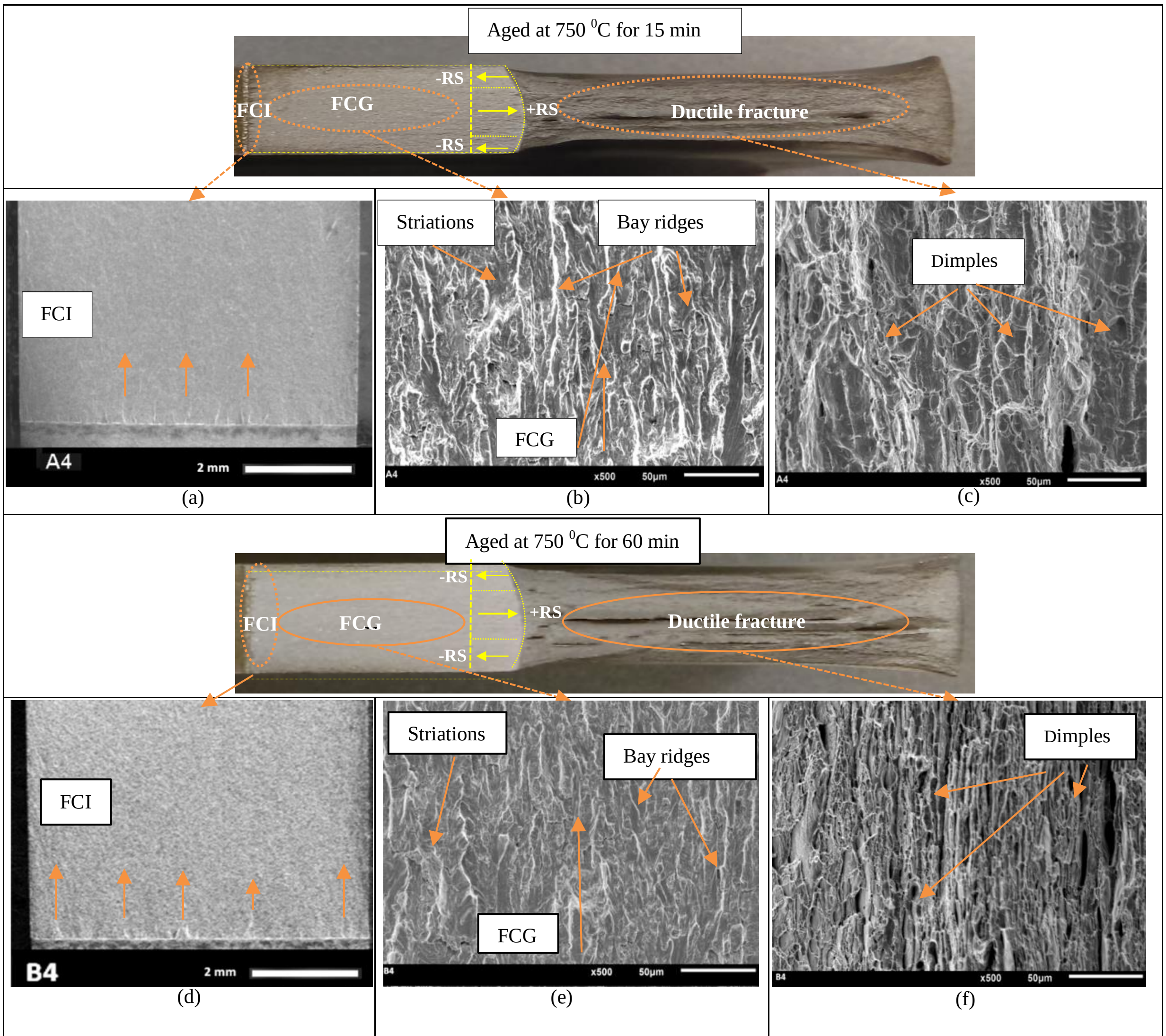


**Figure 5**. Fracture surfaces of the specimens with LSP and aged, (a), (d) crack initiation, (b), (e) fatigue crack growth, (c), (f) final rupture for 15 min and 60 min respectively..

Specimens with aging time of 360 min and 1440 min there is a tendency to start in all edge of the specimen Figure 1 (a), 6 (d), Figure 6 (b), 6 (e) shows fatigue crack growth stable zone, ductile fracture can see in the Figure 6 (c), 6 (f).
In relation to the magnitude of the stable growth zone, a larger area is observed for the case of 15 min and 60 min, the increase is 35% and 55% compared to 360 min and 1440 min respectively. The ductile fracture zone, a considerable increase in the specimens of 360 min and 1440 min is clearly observed; the transverse deformation is almost zero.

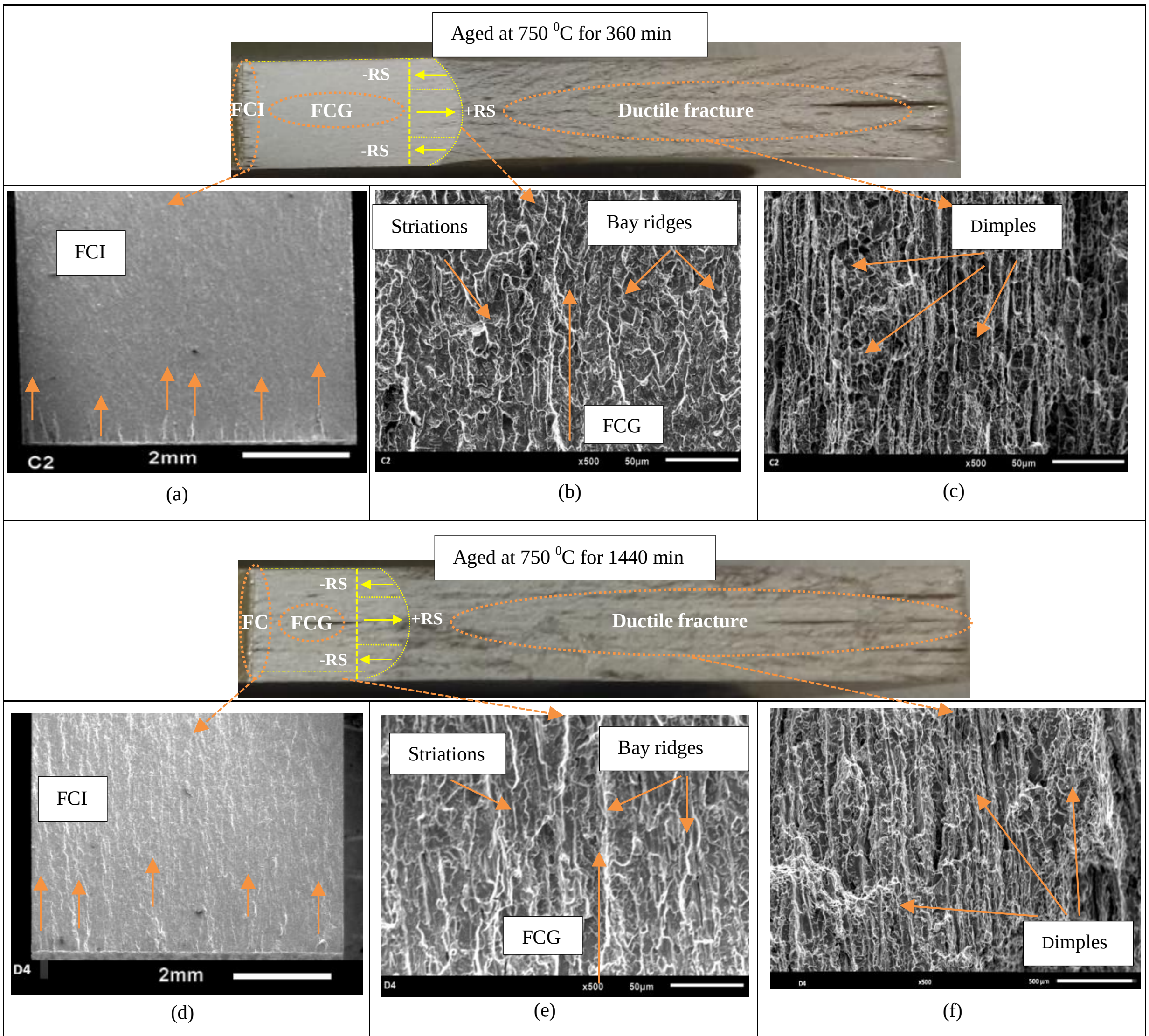


**Figure 6**. Fracture surfaces of the specimens with LSP and aged, (a), (d) crack initiation, (b), (e) fatigue crack growth, (c), (f) final rupture for 360 min and 1440 min respectively.

## Conclusions

The LSP treatment induces beneficial effect in treated specimens with aged damage. Favorable results as obtained in fatigue crack growth test on specimens with 60 min of thermally aged. It was observed effect of residua stress in fracture surface since arrest the fatigue crack growth. The fatigue crack initiation and fatigue crack growth is negatively influenced by the heat treatment principally in the times of 360 and 1440 min; improved effects of LSP are predominantly obtained in the times of 15 and 60 min.

## References

[1] Yongkang Zhang, Jinzhong Lu, Kaiyu Luo, "Laser Shock Processing of FCC Metals". Springer-Volume 179 2013
[2] K. Ding, L.Ye, "Laser shock peening Performance and process simulation", Woodhead Publishing Limited, 2006
[3] P. Peyre, R. Fabbro, "Laser shock processing: a review of the physics and applications", Opt. Quant. Electron. 27 (1995) 1213-1229.
[4] R. Fabbro, J. Fournier, P. Ballard, D. Devaux, J. Virmont. Journal of applied physics 1990; 68: 775-84.
[5] C. Rubio-González, C. Felix-Martinez, G. Gomez-Rosas, J. L. Ocaña, M. Morales, J. Porro, "Effect of laser shock processing on fatigue crack growth of duplex stainless steel", Mater. Sci. Eng. A 528 (2011) 914-919.
[6] J.L. Ocaña, "Fatigue Life Enhancement of High Reliability Metallic Components by Laser Shock Processing" Proc. SPIE (2015) vol. 9356.
[7] Cesar Roberto de Farias, et al, "An overview of the recurrent failures of duplex stainless steels" Engineering Failure Analysis 97 (2019) 161–188.
[8] V. Granados-Alejo, C. Rubio-González, C.A. Vázquez-Jiménez, J.A. Banderas, G. Gómez-Rosas, "Influence of specimen thickness on the fatigue behavior of notched steel plates subjected to laser shock peening", Optics and Laser Technology, 101 (2018) 531–544
[9] Yinfang Jiang, Xin Li, Wenfan Jiang, Quanhong Wan, et al "Thickness effect in laser shock processing for test specimens with a small hole under smaller laser power density" Optics and Laser Technology 114 (2019) 127–134.

# Estimation of the Fatigue Life of Additively Manufactured Metallic Components Using Modified Strain Life Parameters Based on Surface Roughness

Peter Grohs[a], Suraj Nikam[a], Jinseok Kim[a†], Daniel Kujawski[a]

[a]*Western Michigan University, 1903 West Michigan Avenue, Kalamazoo, MI 49009, U.S.A.*

[†]*E-mail address:* jinseok.kim@wmich.edu

**Abstract:** In this study, a method is presented to quantify the effects of surface roughness on the fatigue life of titanium Ti6Al4V, aluminum 7075-T6, and steel 4340 alloys via modified strain life parameters using finite element analysis (FEA). This technique is highly beneficial to the fatigue analysis of additively manufactured metal components, whose rough surfaces, which are difficult to quantify and predict directly using finite element simulation, can be represented by a single effective stress concentration factor $\overline{k}_t$ for the sake of fatigue analysis through the use of surface roughness parameters $R_a$, $R_t$, mean $R_{z,ISO}$, and mean valley radii $\overline{\rho}_{10}$. In this research, notched finite element models with $k_t$ values ranging from 3.058 – 10.75 (representing rough surfaces) are analyzed and the S–N curves are obtained. A parametric study is done to match the S–N curves via a smooth specimen and by modifying fatigue life parameters $\sigma_f{}'$ and $\varepsilon_f{}'$. A relation is established between $k_t$ and $\sigma_f{}'$ and $\varepsilon_f{}'$ such that the effects of a notch on fatigue life, or an effective stress concentration from surface roughness on fatigue life, can be easily studied without any modification to geometry.

***Keywords****:* Fatigue life; Surface roughness; Additive manuifacturing; Finite element method; Strain life parameters

## 1. Introduction

Additively manufactured (3D printed) components are becoming increasingly commonplace in research and industry [1, 2]. The process allows for complex, optimized geometries not previously possible with conventional manufacturing. It is particularly beneficial for metals, which when 3D printed have static properties nearly identical to conventionally manufactured components [3, 4]. However, where monotonic properties are very similar, in their as built state, the parts have extremely irregular and rough surfaces and suffer greatly in fatigue life performance. As-built parts under fatigue fail exclusively due to surface flaws [5]. Surface effects are also difficult to represent using finite element analysis, and although a number of methods exist to represent rough surfaces using statistically generated surface data [6–8], these can be difficult or unfeasible to implement on complex or irregular surface geometries, which is often the case for 3D printed parts. They also require modifications to the underlying geometry and an extremely complex mesh to account for flaws on the order of micrometers, which is unfeasible for large geometries.

An effective method for representing the chaotic surface profile of 3D printed parts using an effective stress concentration factor $\overline{k}_t$ has recently been described. Though initially developed for polymers, fatigue life predictions match reasonably well to a curve of experimental results produced by Pegues et al. [9]. The method of equating surface roughness to an effective stress concentration method utilizes several roughness characteristics to create a holistic representation of the surface roughness in the form of a notch [9].

$$\overline{k}_t = 1 + n\left(\frac{R_a}{\overline{\rho}_{10}}\right)\left(\frac{R_t}{R_{z,ISO}}\right), \quad n = \begin{cases} 1 & \text{shear} \\ 2 & \text{tension} \end{cases} \tag{1}$$

where $R_a = \frac{1}{l}\int_0^l |Z(x)|\ dx$, $R_t = |z_{max} - z_{min}|$, $R_{z,ISO} = \frac{1}{5}\left[\sum_{i=1}^5 z_{i,min} + \sum_{j=1}^5 z_{j,max}\right]$, $\overline{\rho}_{10} = \frac{1}{5}\left[\sum_{i=1}^5 \rho_{i,min}\right]$, $z_{min}$ is the depth of the lowest valley from the ideal surface height, $z_{max}$ is the height of the highest peak from the ideal surface height, $\sum_{i=1}^5 z_{i,min}$ is the sum of the five lowest valleys from the ideal surface height, $\sum_{j=1}^5 z_{j,max}$ is the sum of the five highest peaks from the ideal surface height, and $\sum_{i=1}^5 \rho_{i,min}$ is the sum of the notch radii from the five lowest valleys from the ideal surface height.

It is supposed that this relation between roughness and $k_t$ can be used as a link between surface roughness and its effects on fatigue life. Notches are a well-studied aspect of fatigue research [10]. Examining notch effects using finite element analysis can be as simple as producing the notched geometry and applying a fine enough mesh to capture the effects. Some FEA software packages, such as Ansys Mechanical, even provide mechanisms [11] to account for fatigue notch factor $k_f$, which is equivalent to $k_t$ for cases of fatigue loading, though lower due to the tendency of a material to be less sensitive to notches under cyclical loads. The relation between $k_t$ and $k_f$ is accounted for using the material property notch sensitivity, $q$ [10]. It is a simple affair to determine the effective stress concentration of a part using Eq. (1), then product a notch geometry which matches the value obtained from Eq. (1), and apply it to a FEA model to see its effects on strain life. However, this would only produce a limited picture of the component's fatigue life, and only at the location of the notch. An effective stress concentration would cause lower fatigue life across the entire domain of a component with that surface roughness. Based on this, it is determined that a notched FE model is a poor representation to analyze $\overline{k}_t$ for the purposes of this research.

As an alternative, a relation between $k_t$ and strain life parameters could be used. It is advantageous to use these parameters to study fatigue life performance. Strain life parameters are used exclusively to calculate cycles to failure, and modifying them will not affect the monotonic performance of a component or structure.

**Table 1.** Material properties for FEA [10]

| | | Ti6Al4V | 7075-T6 | 4340 |
|---|---|---|---|---|
| $\sigma_f{}'$ | MPa | 2030 | 1466 | 1758 |
| $b$ | | -0.104 | -0.143 | -0.0977 |
| $\varepsilon_f{}'$ | | 0.841 | 0.262 | 2.12 |
| $c$ | | -0.688 | -0.619 | -0.744 |
| $H'$ | MPa | 1772 | 977 | 1655 |
| $n'$ | | 0.106 | 0.106 | 0.131 |
| $E$ | GPa | 117 | 71 | 207 |
| $\rho$ | kg/m$^3$ | 4620 | 2700 | 7870 |
| $\nu$ | | 0.33 | 0.345 | 0.3 |

## 2. Modeling

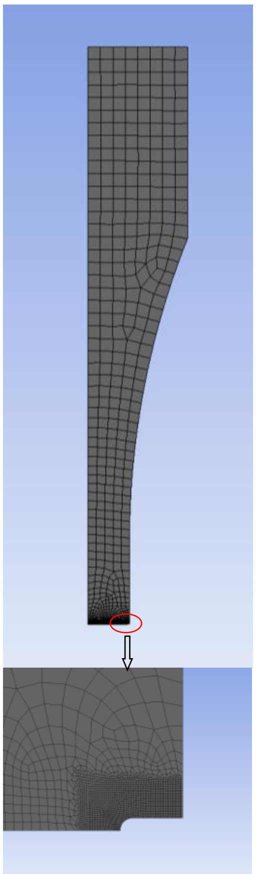

**Figure 1**: Notched FEA model ($k_t = 5.878$)

To study the link between $k_t$ and strain life, parametric studies are done using Ansys Mechanical for titanium, aluminum, and steel alloys. It is noted that a nominal $k_t$ value is assumed for this research. Accounting for crack growth effects using $q/k_f$ is both material and process dependent and is outside of the scope of this research. Material properties for the alloys are listed in Table 1. An axisymmetric model is used for the finite element analysis to save computational time. Making the model symmetric about the center axis further reduces the node count. The Proximity and Curvature sizing model is used to have the best representation of the surface profiles. A Quadrilateral PLANE183 element was used for meshing. A refinement factor of three, which splits one element into sixteen, is applied to the region which is expected to receive 50% of peak stress. This occurs within a depth approximately half the length of the notch into the part. In other words, if a notch extends 20 µm into the surface, a refinement is applied to a region extending 30 µm into the part. Fully reversed uniaxial loading ($R = -1$) was applied to produce S–N curves for each model.

Smooth circular notches with $k_t$ values of 3.058, 3.988, 5.878, 8.044, and 10.750 were applied to the center of the models at the point of peak expected stress. Geometries for these notches to produce the desired $k_t$ have been analytically computed [12]. From these notched models, S–N curves are produced using fully reversed loadings to show actual results. Following this, an attempt is made to reproduce these notched S–N curves using a smooth surface without a notch ($k_t = 1$) and then systematically modifying the strain life parameters $\sigma_f{}'$ and $\varepsilon_f{}'$ to match. Minimizing peak ± % error magnitude in the S–N curve is used as the benchmark, and parameters carried out to maximum three significant digits. If the modeled curve shape deviates from the notched curve, a deviation resulting in a conservative life estimate is preferred. Through extensive simulation work, parameters which provide the strongest correlation are found. These are termed $\sigma_f{}'^*$ and $\varepsilon_f{}'^*$ (Table 3).

It is noted in Figure 2 that the $\sigma_f{}'^*$ and $\varepsilon_f{}'^*$ curves with respect to $k_t$ strongly correlate with

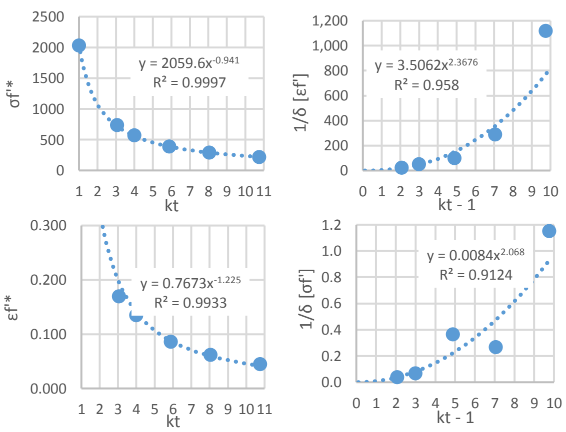


**Figure 2**: Ti6Al4V power law regression

power law regression. However the exponents from this simple power law regression make that model inaccurate at $(k_t = 1)$. A correction factor is introduced to account for this, which reduces the variable count and increases accuracy down to $(k_t = 1)$.

First the calculated regression coefficients are replaced with the original $\sigma_f{}'$ and $\varepsilon_f{}'$ values (see Table 1). A list of predicted initial terms is produced using these as coefficients. The original exponent from the power law regression ($d$ and $j$ for $\sigma_f{}'^{*}$ and $\varepsilon_f{}'^{*}$, respectively) are retained. This produces a list of initial predicted terms, $\sigma_f{}'^{i}$ and $\varepsilon_f{}'^{i}$. The differences between the initial mathematically predicted $\sigma_f{}'^{i}/\varepsilon_f{}'^{i}$ terms and the FEA determined $\sigma_f{}'^{*}/\varepsilon_f{}'^{*}$ terms are called the correction factors, $\delta$. A list of the inverse of the correction factors, $1/\delta$, is graphed against $(k_t - 1)$, so chosen to eliminate the effects of the correction factor at $(k_t = 1)$. Power law regression is done between these lists to produce a regression coefficient ($f$ and $m$) and regression exponent ($g$ and $p$ for $\sigma_f{}'$ and $\varepsilon_f{}'$, respectively). A list of predicted error terms, $\sigma_f{}'^{\delta}$ and $\varepsilon_f{}'^{\delta}$, is produced from this regression. The sum of initial $\sigma_f{}'^{i}/\varepsilon_f{}'^{i}$ and $\sigma_f{}'^{\delta}/\varepsilon_f{}'^{\delta}$ is the final result: $\bar{\sigma}_f{}'$ and $\bar{\varepsilon}_f{}'$.

$$\bar{\sigma}_f{}' = \sigma_f'(k_t)^d + \frac{1}{f\,(k_t - 1)^g} \tag{2}$$

$$\bar{\varepsilon}_f{}' = \varepsilon_f'(k_t)^j + \frac{1}{m\,(k_t - 1)^p} \tag{3}$$

## 3. Results

The effectiveness of this method in FEA is demonstrated in detail for titanium $\varepsilon_f{}'$ analysis in Table 3. Where the initial $\varepsilon_f{}'^{i}$ term varied from the known $\varepsilon_f{}'^{*}$ by up to 48%, the addition of $\varepsilon_f{}'^{\delta}$ reduced the error to 4.5%. Table 2 shows all variables required for equations 2 and 3. Figure 3 compares the notched FEA models to smooth models using the calculated $\bar{\sigma}_f{}'$ and $\bar{\varepsilon}_f{}'$ from Table 2. With this correction factor, the list of parametrically determined strain life terms can be accurately reproduced for any $k_t$ or $\bar{k}_t$ factor in the ranges tested.

**Table 2.** Effective strain life parameters for equations 2 and 3 to represent notches

| | | Ti6Al4V | 7075-T6 | 4340 |
|---|---|---|---|---|
| | $d$ | -0.941 | -0.936 | -0.940 |
| $(\bar{\sigma}_f{}')$ | $f$ | 0.00835 | 0.00376 | 0.155 |
| | $g$ | 2.07 | 2.68 | 1.02 |
| | $j$ | -1.22 | -1.39 | -1.48 |
| $(\bar{\varepsilon}_f')$ | $m$ | -3.51 | -7.37 | -1.18 |
| | $p$ | 2.37 | 2.17 | 2.41 |

**Table 3.** Process for determining $\bar{\varepsilon}_f{}'$ for Ti6Al4V, illustrating error correction effectiveness.

| $k_t$ | $\varepsilon_f{}'^{*}$ | $\varepsilon_f{}'^{i}$ | $\delta$ | $1/\delta$ | $(k_t - 1)$ | $\varepsilon_f{}'^{\delta}$ | $\bar{\varepsilon}_f{}'$ | % error |
|---|---|---|---|---|---|---|---|---|
| *1.000* | **0.841** | 0.841 | 0 | | 0.000 | | **0.841** | 0.00% |
| *3.058* | **0.170** | 0.2140 | 0.04396 | 22.74 | 2.058 | 0.05165 | **0.162** | 4.52% |
| *3.988* | **0.135** | 0.1546 | 0.01957 | 51.10 | 2.988 | 0.02136 | **0.133** | 1.33% |
| *5.878* | **0.0860** | 0.09612 | 0.01012 | 98.82 | 4.878 | 0.006694 | **0.0894** | 3.98% |
| *8.044* | **0.0620** | 0.06546 | 0.003459 | 289.1 | 7.044 | 0.002805 | **0.0627** | 1.06 |
| *10.75* | **0.0450** | 0.04589 | 0.0008936 | 1119 | 9.75 | 0.001299 | **0.0446** | 0.90 |

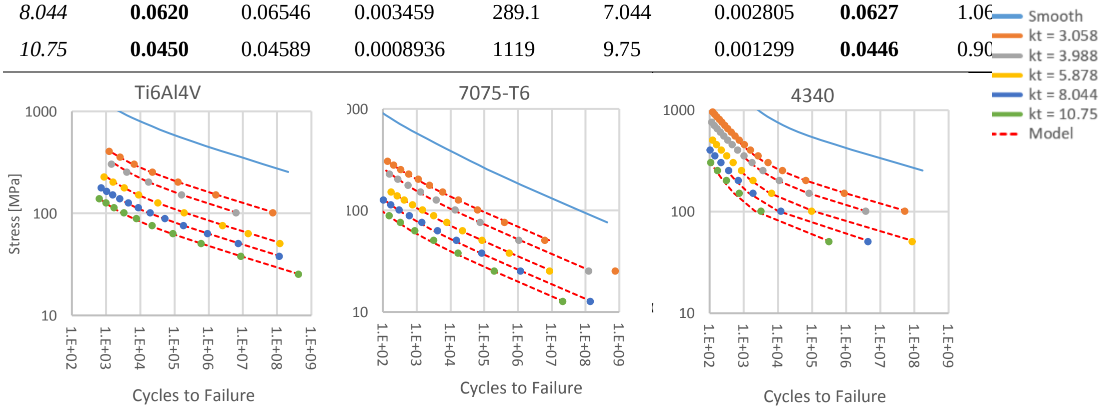

## 4. Conclusions and Future Studies

This research has shown that a notched FEA model can be represented by modifying strain life parameters $\sigma_f{}'$ and $\varepsilon_f{}'$. Furthermore, the variations of these parameters can be modeled as a function of stress concentration factor $k_t$ with material dependent parameters, which have been successfully derived for titanium, aluminum, and steel alloys. This model is able to predict the fatigue life of a notched member to the accuracy described above, and has been demonstrated as viable in FEA for titanium, aluminum, and steel alloys.

Due to the use of only $\sigma_f{}'$ and $\varepsilon_f{}'$, this modified strain life parameter model is not able to account for any curvature changes in the S–N curves as notches are applied, which leads to deviations from actual results. To improve accuracy, strain life exponents $b$ and $c$ must be modified. This paper also assumes a nominal $k_t$, though the effects should be identical for $k_f$. This study is conducted only using finite element analysis and experimental validation on additively manufactured metallic components should be conducted.

Using this modified strain life model, it is proposed that the fatigue life of components with significant surface roughness can be predicted by using finite element model with smooth surface and modified strain life parameters.

## Acknowledgements

The authors gratefully acknowledge the support of Western Michigan University through their research startup fund.

## References

[1] Frazier, W. E. (2014). Metal additive manufacturing: a review. *Journal of Materials Engineering and Performance*, *23*(6), 1917-1928.

[2] Seifi, M., Gorelik, M., Waller, J., Hrabe, N., Shamsaei, N., Daniewicz, S., & Lewandowski, J. J. (2017). Progress towards metal additive manufacturing standardization to support qualification and certification. *Jom*, *69*(3), 439-455.

[3] Yadollahi, A., & Shamsaei, N. (2017). Additive manufacturing of fatigue resistant materials: Challenges and opportunities. *International Journal of Fatigue*, *98*, 14-31.

[4] Yadollahi, A., Mahtabi, M. J., Khalili, A., Doude, H. R., & Newman Jr, J. C. (2018). Fatigue life prediction of additively manufactured material: Effects of surface roughness, defect size, and shape. *Fatigue & Fracture of Engineering Materials & Structures*, *41*(7), 1602-1614.

[5] Wycisk, E., Solbach, A., Siddique, S., Herzog, D., Walther, F., & Emmelmann, C. (2014). Effects of defects in laser additive manufactured Ti-6Al-4V on fatigue properties. *Physics Procedia*, *56*, 371-378.

[6] Thompson, M. K. (2006). Methods for generating rough surfaces in ANSYS. In *Proceedings of the 2006 International ANSYS Users Conference & Exhibition, Pittsburgh, PA*.

[7] Thompson, M. K., Thompson, J. M., & Slocum, A. H. (2007). Surface Topography Importation in Finite Element Models. In *7th International Conference of the European Society for Precision Engineering and Nanotechnology*.

[8] Thompson, M. K., & Thompson, J. M. (2010). Methods for generating probabilistic rough surfaces in ANSYS. In *Proc. 20th Korea ANSYS User's Conf* (pp. 9-10).

[9] Pegues, J. W., Shamsaei, N., Roach, M. D., & Williamson, R. S. (2019). Fatigue life estimation of additive manufactured parts in the as- built surface condition. *Material Design & Processing Communications*, e36.

[10] Dowling, N. E. (2012). *Mechanical behavior of materials: engineering methods for deformation, fracture, and fatigue*. Pearson.

[11] Browell, R., & Hancq, A. (2006). Calculating and displaying fatigue results. *ANSYS® on-line white papers, March*, *29*.

[12] Nowell, D., Dini, D., & Duo, P. (2003). Stress analysis of V-notches with and without cracks, with application to foreign object damage. *The Journal of Strain Analysis for Engineering Design*, *38*(5), 429-441.

# Fracture modelling of large thin-walled structures

Mihkel Kõrgesaar[a,b], Jani Romanoff[b], Heikki Remes[b]

[a]*Tallinn University of Technology, Estonian Maritime Academy, Tallinna 19, 93811, Kuressaare, Estonia*
[b]*Aalto University, Department of Mechanical Engineering, P.O.Box 14300, 00076 Aalto, Finland*

*E-mail address:* mihkel.korgesaar@taltech.ee

**Abstract**

This paper discusses the developments in numerical simulations and their experimental validation of plastic deformation and ductile fracture of large thin-walled steel structures such as ships in collision and grounding events. The basis for discussion is the finite element simulations of penetration tests performed for stiffened and sandwich panels fabricated from steel using laser welding. The simulations employ shell elements. Steps are described to calibrate the fracture criterion suitable for large shell elements. Discussion is given on how this criterion accounts the possible element size variations. Limitations of this approach are highlighted along with challenges introduced by new steel grades, their joining methods and different structural topologies. An outlook to tackle these challenges is presented.

***Keywords****:* collisions; ductile fracture; experiments; simulations; strain-paths; element size; triaxiality

## 1. Introduction

Design of ship structures that can absorb more energy during accidental loading scenarios without rupture contribute to the survivability of ship and thus, to safety at sea. Therefore, around Millennium, the European Union (EU) funded research projects to investigate the collision resistance of ship structures. Full-scale collision test were carried out with various combinations of materials and structures which were designed by state of the art computational methods. Experiments revealed that the structural failure, based on significant plastic deformation and especially ductile fracture under multi-axial stress and strain state, was not successfully predicted with finite element simulations. One reason for the inaccuracies was, and still is, the coarse mesh of shell elements used in these calculations. For computational reasons large shell elements are employed with element length being many times higher than localization zone that needs to be modelled for accurate fracture initiation and propagation analysis. The uncertainties in computational modeling sparked an ongoing experimental-numerical interest in the research community to establish a proper model for the damage prediction [1–6].

First attempts to calibrate the fracture propagation model were pragmatic as they intended to model entire process by an element length dependent equivalent plastic strain [1]. Later it was realized that besides element length and plastic strain, stress state is equally important parameter [7,8]. Nevertheless, benchmark analysis in [9] with three different stiffened shell structures showed that even these fracture criteria are in general not sufficiently accurate. This motivated current authors to design a meticulous experimental campaign that included penetration tests with large sandwich and stiffened steel panels combined with extensive material testing under different stress states. The details of this investigation are presented in [10–12], while this paper presents general information about the experiments and simulations with focus on the outcome of this investigation and lessons learned for future developments.

## 2. Experimental-numerical investigation of the panel response

Investigation involved quasi-static penetration experiments with stiffened and sandwich panels fabricated from steel using laser welding. The main dimensions of square panels were defined so that the stiffness related to membrane action were the same along the principal directions of the plate (*xy*-plane). This led to the situation that sandwich panels are significantly stiffer in bending. It should be noted her that due to the stiffening system especially sandwich panels are significantly orthotropic in shear (around 100/1 stiffness ratio). Panel experiments were complemented by state-of-the-art material characterization with different tensile tests (dogbone, central hole, notched tension and shear) with aim to capture the failure strain for different stress triaxialities. The steps are outlined in Figure 1. The objective was to gauge the fidelity of the panel simulations against the measured data gathered in a controlled laboratory environment.

During experiments data acquisition in panel tests comprised measurement of indentation force and displacement of the indenter. In tensile tests force and displacement were recorded. Discrete fracture data points (markers in Figure 1b) were obtained by comparing the numerical tensile test simulations against experiments (Digital Image Correlation). The Modified Mohr–Coulomb (MMC) plane stress fracture criterion [13] was adopted to provide continuous relation between equivalent plastic failure strain and stress triaxiality. To make this fracture locus applicable to large shell elements a length-scale parameter was introduced that depends on the shell element size (element length to thickness ratio L/t) and stress triaxiality ($\eta$); see Figure 1b right figure.

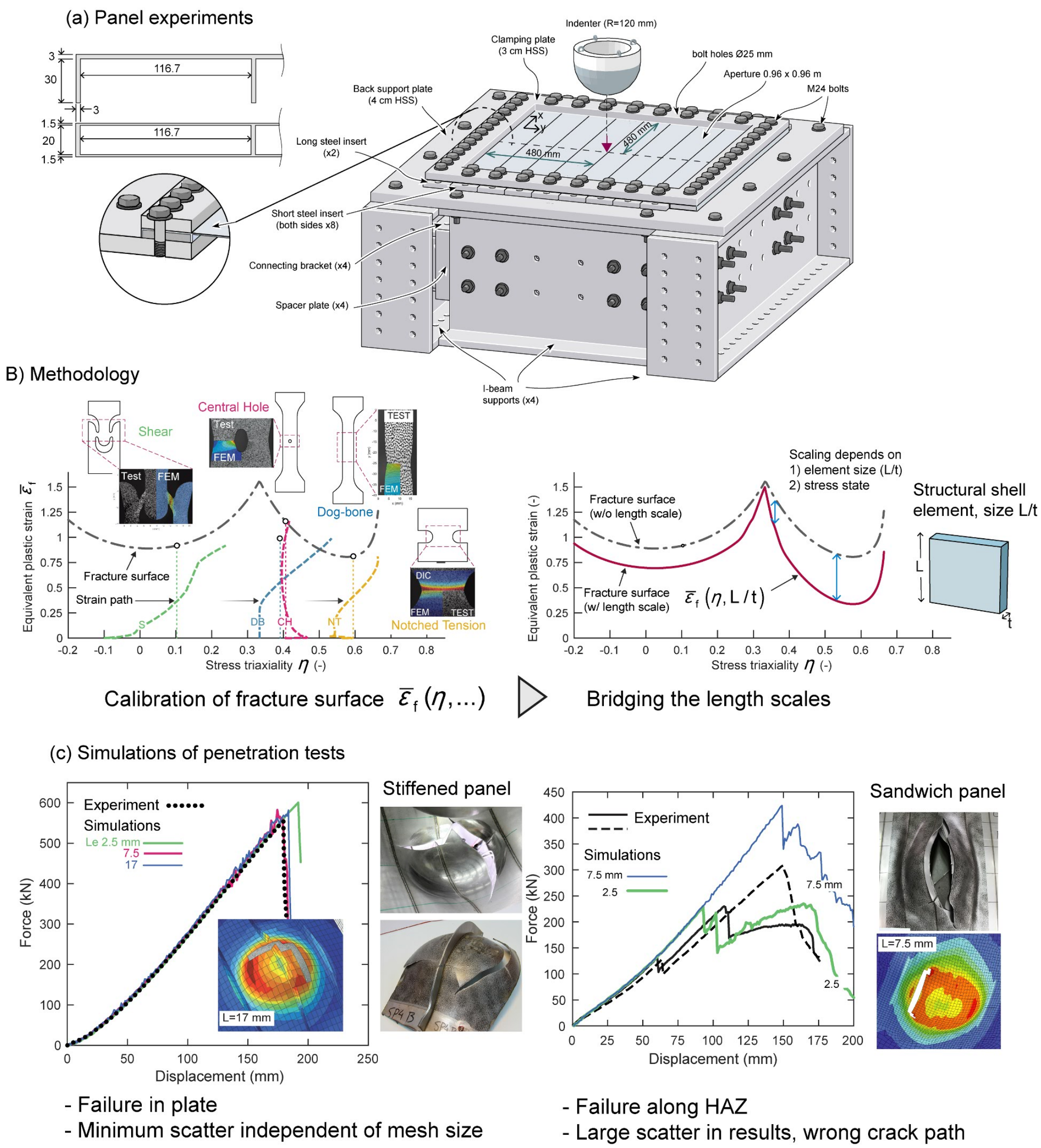


**Figure 1**: The overview of the experimental-numerical study on the penetration response of stiffened and sandwich panels. (a) Setup used for panel experiments. (b) Characterization of steel properties until fracture initiation with experimental and numerical tests including the fracture criterion calibration (S – shear, DB – dog bone, CH – central hole, and NT – notched tension specimen. (c) Simulated panel response with the fracture criterion shown in figure (c). Figures are adopted from [10,12].

Stiffened and sandwich panel simulation results are compared against experiments in Figure 1c. The crucial difference between next generation sandwich panels and more traditional stiffened panels is their load carrying mechanism. In the elastic regime bending stiffness dominates the structural resistance and the sandwich panels demonstrate higher structural stiffness, but also more localized deformation. This deformation is local due to orthotropy in shear. The outcome of this is significant secondary bending (warping) of the unit cells under the indenter. This exposes the laser-welds, web- and face-plates to significant bending. As loading is increased, both panels start to carry the load by membrane action as intended, but the sandwich panels does this more locally due to prevailing step. When fracture initiates in the stiffened panel load carrying capacity immediately drops close to non-existing. Fracture propagates in the face plating with stiffeners contributing little to the overall response. Simulated force-displacement relation correlates with measured data independent of the element size used. In contrast, in general, the behavior of sandwich panel is more desirable in a crash event as the panel can still sustain some load after fracture onset. Although, the first fracture happens at lower load than in stiffened panel. Both in simulations and experiments fracture propagated along the face and web interface, which is along the heat affected zone. Consequently, the scatter in experimental and simulated results is much higher compared to stiffened panels and the details such as the first load drop in the response are not captured. Consequently, the fracture strain scaling approach in Figure 1B is sufficiently accurate and efficiently circumvents the mesh dependence when failure is limited to base plate, but not in the sandwich panel where the weakest links in the structure become more pronounced and localized in the zones of stress concentrations due to bending, material and geometrical discontinuities. Therefore, approach is insufficient for predicting the fracture propagation, respectively the opening size, in large welded ship structures involving material and geometrical discontinuities characteristic to novel light weight high-load carrying energy efficient structural configurations. Moreover, our detailed analysis of failed elements in stiffened panel [11] showed that fairly limited range of strain paths was actually present during failure, see Figure 2. During a real crash events, much more complex loading scenarios are expected involving shear stresses and bending as shown by Kõrgesaar [14].

Morin et al. [19] developed a numerical method tailored for shell framework to account the evolving through thickness strain gradients during bending. However, the approach fails to consider structural discontinuities due to welded joints or shear stresses. The welding process involves local heating of the metal resulting in change of material properties in the heat affected zone. Depending on the material the strength of the material in these zones can reduce like in aluminium [20,21] or increase, but become brittle, like in steel [22]. Present approaches fail to address these discontinuities in a consistent fashion leading to incorrectly predicted crack path. Moreover, these uncertainties are expected to increase further when considering low temperatures, high strength steels (high probability of shear failure) and material thickness variations. This is important considering the significant increase in Arctic activities due to global warming and extraction of natural resources such as oil and gas. Structures operating in these regions are exposed to harsh environmental conditions, particularly sub-zero temperatures (average −50 °C). The crashworthiness of structures for such events should be confirmed in the design phase, but proper design guidelines for modelling of material behaviour at low temperatures are lacking. Recent study [26] showed that brittle fracture in welded stiffened steel structures is predicted insufficiently with current methods.

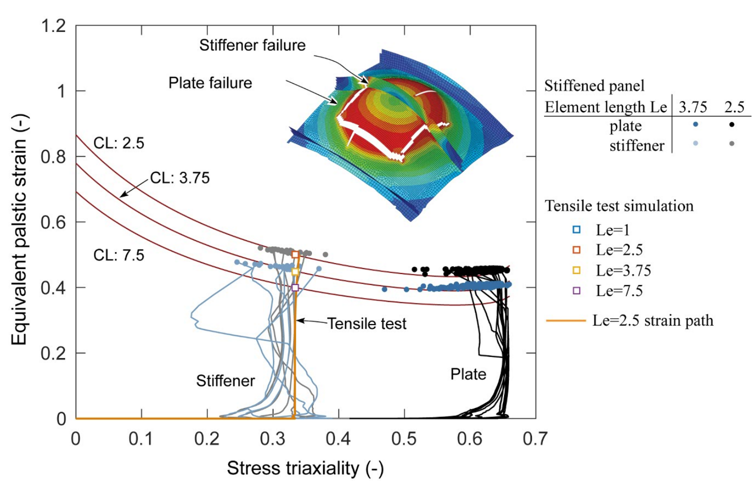


**Figure 2**: Strain paths of failed elements in stiffened panel simulation. Figure is adopted from [11].

## 3. Conclusion

For computational reasons collision and grounding simulations of large thin-walled steel structures employ shell elements that makes it challenging to capture the point of fracture initiation, and as a follow-up proper prediction of the propagation. This is essential in welded steel structures that exhibit material and geometrical discontinuities that change during the evolving plastic deformation preceding the fracture initiation. As the load-carrying mechanism changes, so do the strain and stress paths controlling the material failure. To capture the fracture onset and propagation demands, on the one hand, sophisticated modelling efforts, but on the other hand, must be simple enough to put into practical use. Development of such methods is the subject of the ongoing work.

## Acknowledgements

The experimental program would not have been possible without the funding by the Scientific Advisory Board For Defence (MATINE, 2500M-0058). The simulations and analyses were carried out in project called *Ultra Lightweight and Fracture Resistant Thin-Walled Structures through Optimization of Strain Paths*, by Academy of Finland (310828). The Abaqus License as well as technical support was provided by the CSC Centre for Science. These contributions are gratefully acknowledged.

## References

[1] Simonsen BC, Törnqvist R. Experimental and numerical modelling of ductile crack propagation in large-scale shell structures. Mar Struct 2004;17:1–27. doi:10.1016/j.marstruc.2004.03.004.

[2] Ehlers S, Broekhuijsen J, Alsos HS, Biehl F, Tabri K. Simulating the collision response of ship side structures: A failure criteria benchmark study 2008;55:127–44.

[3] Hogström P, Ringsberg JW. An extensive study of a ship's survivability after collision - A parameter study of material characteristics, non-linear FEA and damage stability analyses. Mar Struct 2012;27:1–28. doi:10.1016/j.marstruc.2012.03.001.

[4] Kõrgesaar M, Romanoff J. Influence of mesh size, stress triaxiality and damage induced softening on ductile fracture of large-scale shell structures. Mar Struct 2014;38:1–17. doi:10.1016/j.marstruc.2014.05.001.

[5] Storheim M, Alsos HS, Hopperstad OS, Amdahl J. A damage-based failure model for coarsely meshed shell structures. Int J Impact Eng 2015;83:59–75. doi:10.1016/j.ijimpeng.2015.04.009.

[6] Cerik BC, Lee K, Park SJ, Choung J. Simulation of ship collision and grounding damage using Hosford-Coulomb fracture model for shell elements. Ocean Eng 2019;173:415–32. doi:10.1016/j.oceaneng.2019.01.004.

[7] Törnqvist R. Design of crashworthy ship structures. vol. 103. 2003. doi:10.1007/s00726-011-1022-z.

[8] Alsos HS, Hopperstad OS, Törnqvist R, Amdahl J. Analytical and numerical analysis of sheet metal instability using a stress based criterion. Int J Solids Struct 2008;45:2042–55. doi:10.1016/j.ijsolstr.2007.11.015.

[9] Storheim M, Amdahl J, Martens I. On the accuracy of fracture estimation in collision analysis of ship and offshore structures. Mar Struct 2015;44:254–87. doi:10.1016/j.marstruc.2015.09.006.

[10] Kõrgesaar M, Romanoff J, Remes H, Palokangas P. Experimental and numerical penetration response of laser-welded stiffened panels. Int J Impact Eng 2018;114:78–92. doi:10.1016/j.ijimpeng.2017.12.014.

[11] Kõrgesaar M, Romanoff J, Remes H. Influence of material non-linearity on load carrying mechanism and strain path in stiffened panel. Procedia Struct Integr 2017;5:713–20. doi:10.1016/j.prostr.2017.07.050.

[12] Kõrgesaar M, Romanoff J, Palokangas P. Experimental and numerical assessment of fracture initiation in laser-welded webcore sandwich panels. Eighth Int Conf Thin-Walled Struct - ICTWS 2018 2018:1–17.

[13] Bai Y, Wierzbicki T. Application of extended Mohr-Coulomb criterion to ductile fracture. Int J Fract 2010;161:1–20. doi:10.1007/s10704-009-9422-8.

[14] Kõrgesaar M. The effect of low stress triaxialities and deformation paths on ductile fracture simulations of large shell structures. Mar Struct 2019;63:45–64. doi:10.1016/j.marstruc.2018.08.004.

# Multiaxial Fatigue Behavior and Modeling of Notched Additive Manufactured Specimens

Reza Molaei[a], Ali Fatemi[a], Nam Phan[b]

[a] *Mechanical Engineering Department, The University of Memphis, Memphis, TN 38152, USA*

[b] *Structures Division, US Naval Air Systems Command (NAVAIR), Patuxent River, MD 20670, USA*

*E-mail address:* rmolaei@memphis.edu

**Abstract** Additive Manufacturing (AM) has gained significant attention in recent years due to several important advantages. However, design of critical load carrying parts using this technique is still at early stages. This is partly due to the lack of sufficient understanding of cyclic and fatigue behavior of these materials as compared to their wrought counterparts. While fatigue performance of AM metals has been evaluated under unnotched uniaxial conditions, most applications involve stress concentrations due to the presence of notches, where stress gradient effect may also be present at the notch root. In this work, notched fatigue and cracking behavior of two commonly used AM metals (Ti-6Al-4V and 17-4 PH Stainless Steel) with different post fabrication heat treatments and surface roughness conditions were studied. Fatigue tests were performed under axial, torsion, and combined axial-torsion loading conditions. The test results are compared to the AM unnotched as well as to the notched and unnotched wrought counterparts. Fatigue analysis is performed at the notch root with considering the effect of stress gradient on the resulting behavior. Different approaches, including stress-based and critical plane-based, are used to model the notch effect on fatigue life.

***Keywords**:* Additive Manufacturing; Multiaxial Fatigue; Notch Effect; Stress Concentration;

## 1. Introduction

Additive Manufacturing (AM) offers considerable advantages over the traditionally fabricated parts (i.e. subtractive manufacturing). Some of these advantages include the capability of fabricating complex geometries difficult to make using conventional methods, the ability to build integrated parts with eliminating some jointing and assembly issues, and on-site fabrication of replacement parts. However, in order to use AM technique in fabricating the parts for critical applications, such as those in aerospace and bio-medical industries, understanding the cyclic properties and fatigue performance of these parts are of utmost important considerations. Despite this importance, the fatigue damage process and cracking behavior of parts fabricated with this technique have not yet been clearly understood, as compared to the conventional fabrication methods. Porosity and Lack of Fusion (LOF) defects, surface roughness, residual stresses, and anisotropy are some of the distinguishing features of the AM parts as compared to the conventionally fabricated parts.

Stress concentrations in producing parts with complex geometries are inevitable. In addition, the rough surface and un-melted particle clusters on the surface of the AM fabricated parts can also act as stress concentrations and significantly affect the fatigue behavior. These stress concentrations most often serve as fatigue crack initiation sites and their effects cannot be underestimated. It is, therefore, essential to be able to accurately characterize the material's behavior in the presence of stress concentrations.

In this work, notched fatigue performance of two commonly used AM metals including Ti-6Al-4V and 17-4 PH Stainless Steel are studied. Different heat treatment and surface finish conditions are considered. Fatigue tests were performed under axial, torsion, and combined axial-torsion loading conditions. The test results are then compared to the unnotched AM and notched and unnotched wrought conditions. The stress distributions around the notch and the effect of stress gradient on fatigue behavior are investigated based on results from linear as well as non-linear FEA. Different approaches, including stress-based and critical plane-based methods are then used to correlate the notched and unnotched fatigue test results together.

## 2. Experimental Program

All the test performed in this study utilized thin-walled (wall thickness if 1.25 mm to 1.6 mm) tubular specimens of Ti-6Al-4V and 17-4 PH Stainless Steel alloys. A Laser Beam Powder Bed Fusion (LB-PBF) AM machine, EOS M290, was used to fabricate the specimens, all in the vertical direction. Ti-6Al-4V samples were tested in annealed (at 700℃ for 1 hour) and HIPed (at 920℃ and 100 MPa for 3 hours), while 17-4 PH specimens were only tested in CA-H1025 heat treated condition. The specimens were tested in both as-built surface and machined surface conditions.

For the notched Ti-6Al-4V specimens, a transverse hole notch was built in the gage section of the specimens, while for the as-built surface 17-4 PH specimens the notch was drilled after the build. For the machined surface condition, the notch was drilled after machining for both materials. The notch had a diameter of 2.4 mm for Ti-6Al-4V specimens, while it was 2.78 mm for 17-4 PH samples. The ratio of the hole diameter to the wall thickness of the specimen was chosen in a way to maintain the plane stress condition surrounding the hole, which was verified using FEA [1]. Representatives of the notched as-built surface and machined surface Ti-6Al-4V specimens are shown in Figure 1.

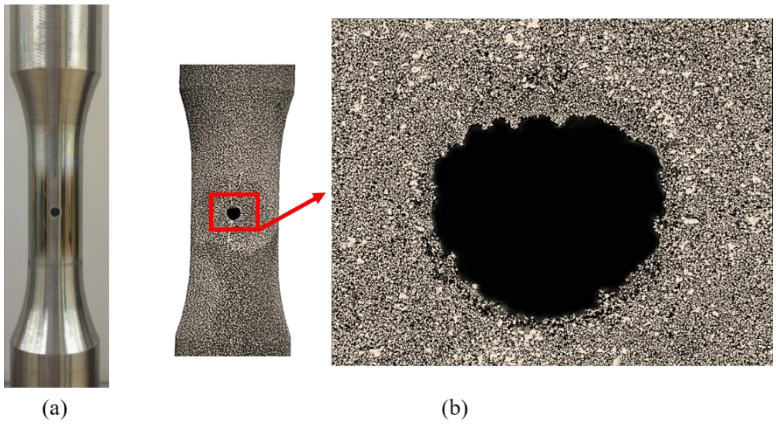


**Figure 1**. Notched tubular specimen geometries of Ti-6Al-4V specimens for (a) machined surface and (b) as-built surface conditions. The notch is built during the AM fabrication process for the as-built surface condition.

As can be seen in Figure 1(b), although the notch was designed to be circular, stair-stepping effect of the AM process resulted in a non-circular notch. This non-uniformity, higher roughness, and sharp edges at the top half of the notch can result in higher stress concentrations than expected and, therefore, premature failures under specific loadings such as torsion, which needs to be considered in design and subsequently in the analysis. Some discussions about this issue will be made in Section 3.

Axial, torsion, and combined in-phase and 90° out-of-phase axial-torsion fatigue tests were performed in load-controlled mode for the notched specimens, all under fully-reversed ($R$ = -1) loading condition. The combined axial-torsion tests had a surface stress ratio of $\sigma/\tau = \sqrt{3}$. For more information about the fabrication process, specimen preparation, testing and crack monitoring procedures the reader is referred to [1].

## 3. Cracking Behavior

Although it has been shown for conventionally fabricated ductile behaving materials that cracks initiate at the notch root on the maximum shear plane orientation for a few hundred microns, and then tend to turn to the maximum tensile plane for the rest of their development period [2], they may act differently for the AM fabricated metals. This could be due to several factors such as presence of surface and/or near surface defects and their interactions with the mechanically induced notches, material ductility, anisotropy, and build direction effects of the AM parts. Representatives of the crack paths observed for the notched as-built surface annealed Ti-6Al-4V specimens and machined surface CA-H1025 treated 17-4 PH specimens are shown in Figure 2 under torsion and combined in-phase axial-torsion loading conditions. The distribution of von-Mises, maximum principal, and maximum shear stresses around the circumference of the hole/notch are also included using radar charts.

Comparison of the radar charts and the crack occurrence locations around the holes in Figure 2 indicate that cracks always occur at the highest stressed location around the hole circumference, regardless of the material and surface condition. However, a closer look at the as-built surface Ti-6Al-4V specimens under torsion loading indicates that although two out of four cracks initiate at -45° and -135° locations, the top two cracks deviate slightly from the expected locations and initiate at about +60° and +120° rather than +45° and +135°, respectively. This is due to the stair-stepping effect discussed earlier for the overhanging regions, which results in sharp edges and much higher roughness of the material at the top half of the hole for the specimens built in the vertical direction. Similar observations were reported in [3] for AM Inconel 718 with V-shaped notches.

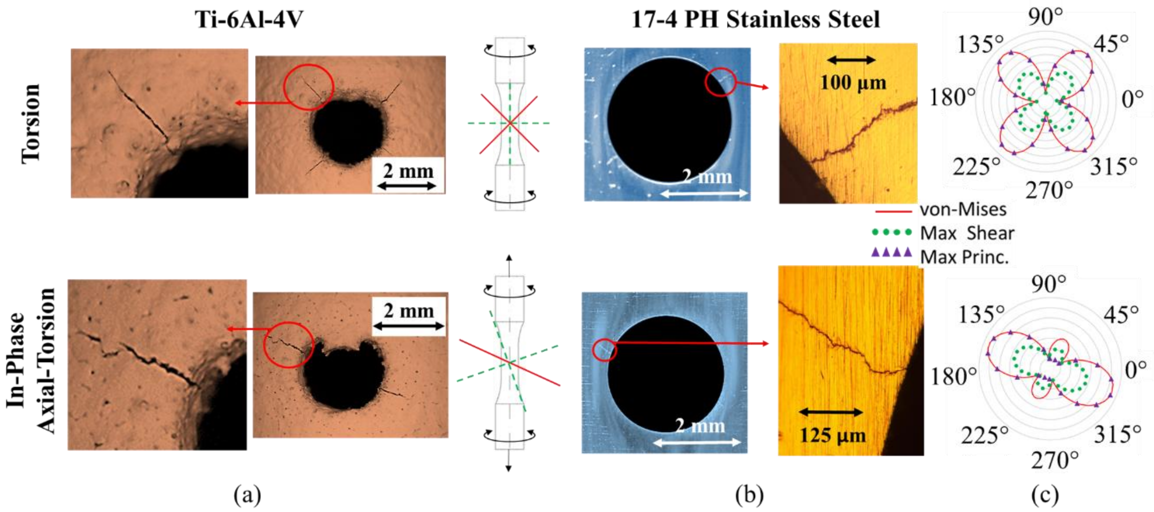


**Figure 2**. Crack paths of (a) as-built surface annealed Ti-6Al-4V specimens and (b) machined surface CA-H1025 treated 17-4 PH specimens under torsion and axial-torsion loading conditions. (c) Radar chart distribution of von-Mises equivalent stress, maximum principal stress, and maximum shear stress around the notch circumference. Solid red lines indicate maximum principal plane orientations, and dashed green lines indicate maximum shear plane orientations.

It was found that although the overall crack growth direction is in mode-I on the maximum principal plane orientation for as-built surface and machined surface conditions of both materials, the initiation orientations were not the same. The initiation orientation of the machined surface specimens was in mode-II on or about the maximum shear plane orientation for both materials, while cracks dominantly initiated and grew in mode-I on or near the maximum principal plane orientation when the as-built surface is present.

Notched specimens were mostly tested at much lower nominal stress levels as compared to the unnotched specimens. Therefore, when the crack initiates in mode-II at the notch root and propagates out of the notch root for a few hundred microns, the combined effect of friction and roughness induced crack closure reduce the effective shear mode driving force until it drops below a critical level to cause the transition to tensile mode (mode-I) [4]. It was discussed in [1, 5] that similar to the as-built surface unnotched specimens, when the rough surface is present for the notched condition, this effect could cause the crack to primarily initiate in mode-I.

## 4. Multiaxial Fatigue Behavior and Data Correlations

As discussed earlier, stress concentration effect of the notches increase the local stresses/strains at the notch root. On the other hand, defects have been found to be the dominant contributors in controlling the fatigue behavior of AM metals in unnotched condition. Hence, it is important to understand how a mechanically induced notch and AM induced defects interact under cyclic loads. From the axial and torsion fatigue tests performed on both unnotched and notched machined surface 17-4 PH specimen data shown in Figure 3, it is clear that the notch effect is significant for both AM and wrought alloys. However, there is much less sensitivity to the notch in AM specimens with increased life as compared to the wrought material. The lower notch sensitivity of the AM is because of the presence of defects in this condition.

In addition, as can be seen in this figure, although there is a significant difference in fatigue behavior of unnotched AM and wrought materials due to the presence of defects in AM alloy, their fatigue behaviors are relatively similar in the notched condition. This indicates that when the notch is present, the stress concentration effect of the notch overtakes the effect of AM internal defects and controls the fatigue performance. Therefore, when stress concentrations due to notches or complexities of the geometry are present in AM parts, the effect of internal defects may be small, and the fatigue performance could be similar to the wrought material.

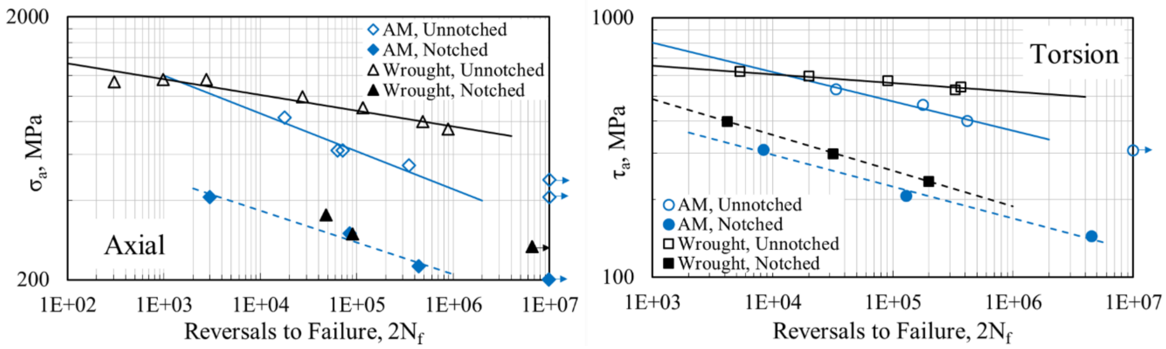


**Figure 3.** Comparison of fatigue test results of machined surface AM and wrought 17-4 PH under (a) axial, and (b) torsion loadings.

The primary difference between the notched and unnotched fatigue analysis is the need to determine the local stresses and strains at the notch root from the nominally applied stresses/strains. The local stress and strain values as well as the local damage of the notched specimens can be calculated after finding the critical locations at the notch root using FEA and considering the stress concentrations and gradient effects via Theory of Critical Distance (TCD). Given the shortcomings of the equivalent stress/strain approaches, critical plane-based damage parameters have been used extensively in recent years for the multiaxial fatigue analysis. These, not only can provide fatigue life estimation under different stress states, but also can predict the failure crack orientations. As can be seen in Figure 4 for a small number of axial and in-phase axial-torsion notched fatigue test results of the as-built surface annealed Ti-6Al-4V and machined surface 17-4 PH CA-H1025 alloys, Fatemi-Socie critical plane-based parameter correlates the notched data with the unnotched data based on the same local damage value.

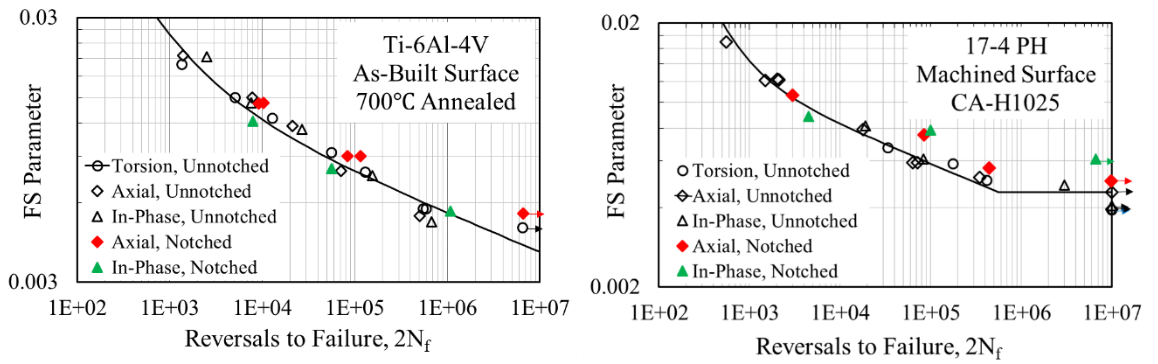


**Figure 4.** Multiaxial notched and unnotched data correlations of (a) as-built surface Ti-6Al-4V and (b) machined surface 17-4 PH alloys based on Fatemi-Socie damage parameter.

## Acknowledgements

United States Naval Air Systems Command (NAVAIR) provided financial support for this study. The authors would like to thank Dr. Nima Shamsaei of Auburn University for fabricating some of the AM specimens.

## References

[1] R. Molaei, A. Fatemi, "Crack paths in additive manufactured metallic materials subjected to multiaxial cyclic loads including surface roughness, HIP, and notch effects," International Journal of Fatigue, vol. 124, pp. 558-570, 2019.

[2] N. Gates, A. Fatemi, "Notched fatigue behavior and stress analysis under multiaxial states of stress," International Journal of Fatigue, vol. 67, pp. 2-14, 2014.

[3] K. Solberg, F. Berto, "Notch-defect interaction in additively manufactured Inconel 718," International Journal of Fatigue, vol. 122, pp. 35-45, 2019.

[4] N. Gates, A. Fatemi, "Fatigue crack growth behavior in the presence of notches and multiaxial nominal stress states," Engineering Fracture Mechanics, vol. 165, pp. 24-38, 2016.

[5] R. Molaei, A. Fatemi, "Crack paths in additive manufactured Ti-6Al-4V specimens subjected to multiaxial cyclic loads " 6th International Conference on Crack Paths (CP 2018), Italy, September, 2018.

# Effect of grain size and grain boundary stability on fatigue and fracture of nanocrystalline nickel thin film

Y. Nakai[a], H. Enomoto[a], R. Takeshige[a], T. Hirai[a], S. Kikuchi[b]

[a]*Department of Mechanical Engineering, Kobe University,1-1, Rokkodai,Nada, Kobe 657-8501, Japan*
[b]*Department of Mechanical Engineering, Shizuoka University, 3-5-1, Johoku, Naka, Hamamatsu 432-8561, Japan*

*E-mail address:* nakai@mech.kobe-u.ac.jp

**Abstract** Recently, not only grain size but also grain boundary stability is recognized as another important factor to affect the mechanical properties of nanocrystalline alloys. The effect of the grain boundary stability on fatigue properties, however, has not been clarified yet. In the present paper, nickel nanocrystalline thin film was fabricated by electrodeposition, and the grain size was changed by the amount of brightener additive in the electrodeposition solution, where sodium allyl sulfonate ($C_3H_5SO_3Na$) was employed as the brightener. The grain boundary stability was changed by low temperature annealing. Tensile and fatigue strengths were increasing with decreasing grain size. Although low temperature annealing deteriorated the tensile strength, it improved the fatigue strength. The ratio of the fatigue limit to the tensile strength for nanocrystalline thin film is much smaller than that for bulk metals. No effect of stress ratio on $da/dN$- $\Delta K$ relationship was observed, but the value of $\Delta K_{th}$ is lower for smaller grain size film, where the crack closure was not observed for nanocrystalline thin film for $R$>0.

***Keywords**:* nanocrystalline nickel, thin film, grain size, grain boundary stability, fatigue

## 1. Introduction

Nanocrystallization is one of the most promising technique to improve the fatigue strength of metallic materials, and their thin films are now being widely used for micro-electro-mechanical systems. The electrodeposition method will be the easiest method to obtain a uniform nanocrystalline structure in thin films, and the effect of grain size on the mechanical and fatigue properties has been studied, where the grain size depended on the electrodeposition condition such as brightener additive. Recently, it has been proposed that grain boundary stability provides an alternative dimension in addition to grain size for producing novel nanocrystalline metals with extraordinary properties [1]. The non-equilibrium grain boundary structure can be changed to the equilibrium one by the annealing at low temperature without affecting the grain size [2]. The grain boundary relaxation during annealing brought the hardening effect [3,4]. Therefore, the effect of grain boundary stability on the mechanical and fatigue properties of electrodeposited nanocrystalline nickel thin films should be clarified.

Moreover, the effect of force ratio and crack closure has not been studied for nanocrystalline thin film while it is well known for fracture mechanics studies of conventional metallic materials that the fatigue crack propagation behavior is affected by the force ratio and the grain size, and these effects have been explained by the difference in crack closure [5].

In the present paper, nickel nanocrystalline thin films are produced by electrodeposition using sulfamate solution, and the effects of the amount of brightener additive in the electrodeposition solution, which brings the change of grain size, and grain boundary stability on the tensile properties and fatigue properties, are examined. In fatigue crack propagation tests, the effect of force ratio is also investigated.

## 2. Material and experimental procedures

### *2.1. Material*

Nickel thin films were produced by electrodeposition using sulfamate solution. The composition of the solution in g/L was as follows: 250 nickel sulfamate, 30 boric acid, 10 nickel chloride, 0.4 sodium lauryl sulphate. Sodium allyl sulfonate ($C_3H_5SO_3Na$) from 0 to 3.2 g/L was employed as brightener. A polished stainless steel plate was used for a cathode and a pure nickel plate for an anode. The temperature of the bath was kept constant at 313 K in a hot-water circulating bath. The pH value of the solution was maintained at 4.0 by adding sulfamate acid. The solution was stirred by a magnetic stirrer to avoid pit formation. The current density was kept constant at 0.25 mA/mm$^2$ by using a constant current supply. Deposition time was 1.8 ks to obtain the film thickness of 10 μm. After deposition, thin films were

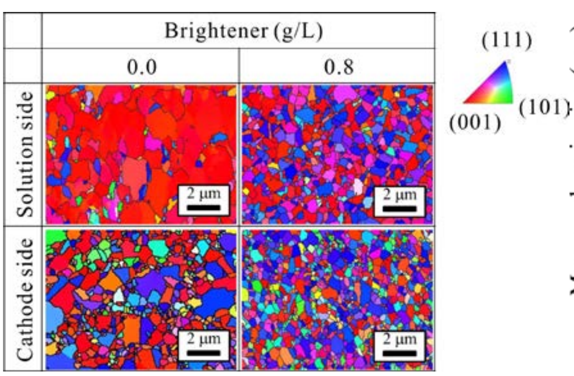


Figure 1. EBSD analysis of thin film.

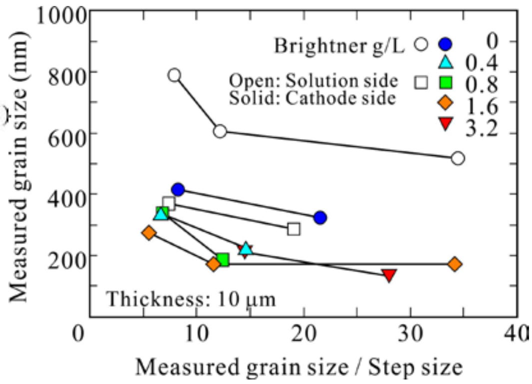


Figure 2. Effect of step size on grain size measurement.

removed from the cathode and subjected to the characterization of tensile and the fatigue properties as free-standing films. Specimens were glued to grips with cyanoacrylate adhesive.

### *2.2. Mechanical tests*

Tensile tests were carried out using a stepping motor driven machine with a capacity of 50 N under cross-head speed of 0.01 mm/s. Since measurement of elongation in reduced parallel section is difficult for thin film sample, it was estimated from the displacement between grips.

Fatigue tests were performed using electrodynamic testing machine with a capacity of 490 N for smooth specimens, and 50 N for crack propagation tests in air without any temperature or moisture control under sinusoidal loading wave with a force (stress) ratio of $R$ = 0.1 or 0.5 and a frequency of 10 or 20 Hz. The crack propagation tests were conducted under stress-intensity-factor-range ($\Delta K$)-controlled conditions. The crack lengths were continuously monitored using compliance between the applied force and the grip-to grip displacement, which was measured by a high resolution laser displacement meter. Crack closure behavior was also observed the elastic-unloading compliance method.

## 3. Experimental results and discussion

### *3.1. Microstructure and grain size*

Figure 1 shows orientation of crystals obtained by EBSD analysis. To accomplish these observations, the materials were annealed at 523 K for 3.6 ks because Kikuchi pattern did not appear for electrodeposition films without annealing. It was reported that low temperature annealing does not change the grain size [2]. Films obtained without brightener additive in the electrodeposition solution, the grain size is much different at cathode side and at solution side. At the cathode side, the orientation is almost random while grains have preferred orientation of (001) direction at the solution side and the grain size at the solution side is much larger than that of cathode side. Films obtained with brightener additive in the electrodeposition solution, the orientation of grains is almost random in both sides, and the grain size is almost the same in both sides. The grain size of this film is much smaller compared with that obtained without brightener additive in the electrodeposition solution.

Grain size was measured by EBSD analysis. The measured grain size depends on the step size as shown in Fig. 2 indicating the step size should be less than one tenth of the grain size, the measured grain size is almost consistent and EBSD analysis can indicate appropriate value of the grain size. The effect of the amount of brightener additive in electrodeposition solution on the grain size of the obtained film is small, while it is significantly smaller than that without brightener additive in electrodeposition solution. The grain size of film from solution with amount of brightener additive in electrodeposition solution is about 200 nm and that without brightener additive in electrodeposition solution is about 300 nm.

### *3.2. Tensile test*

Figure 3 shows the stress-strain relationship and Fıgure 4 shows the effect of graın sıze on the tensıle strength. For as-prepared film, both the ductility and the tensile strength are greater with increasing amount of brightener additive in electrodeposition solution. For annealed film, however, the effect of amount of brightener additive in electrodeposition solution on these tensile properties is small while that is much larger compared with the film without brightener additive in electrodeposition solution.

For films without brightener additive, the effect of heat-treatment on the tensile strength and the fracture ductility are small, but both of them are much smaller for annealed film those for as-prepared film. The residual stress may be smaller for annealed film, therefore, the grain boundary stability must be responsible for this difference, and the annealing makes the film brittle as already reported by [1].

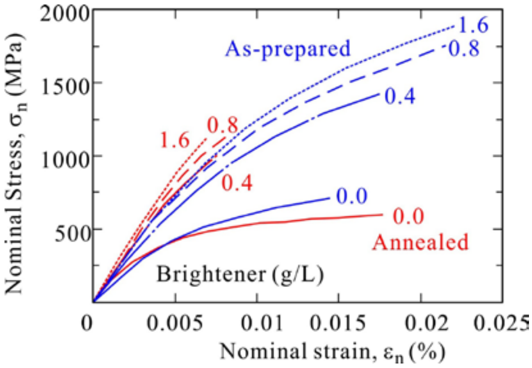


Figure 3. Stress-strain curves.

### 3.3. Fatigue life

*S*–*N* curves are shown in Fig. 5. Clear fatigue limit exists for all films, and it is much larger for films obtained with brightener additive in electrodeposition solution than that obtained without brightener additive in electrodeposition solution. Small effect of amount of brightener additive in electrodeposition solution can be recognized and the fatigue strength for annealed films is higher than that for as-prepared film.

The stress amplitude, $\sigma_a$, normalized by the tensile strength, $\sigma_{UTS}$, is plotted against the number of cycles to failure, $N_f$, in Fig. 6. Almost unique relationship is obtained for each heat-treatment, and the fatigue limit is found to proportional to the tensile strength. However, the ratio is 10 % for annealed film and 15% for as-prepared film while it is from 30 to 60 % for most of conventional bulk alloys. It should be clarified whether nanocrystallization, thickness, or fabrication by electrodeposition is responsible for this difference.

Figure 7 shows the effects of grain size and heat-treatment of the fatigue limit, indicating the annealing derives beneficial effect to the fatigue strength while it deteriorates the tensile strength.

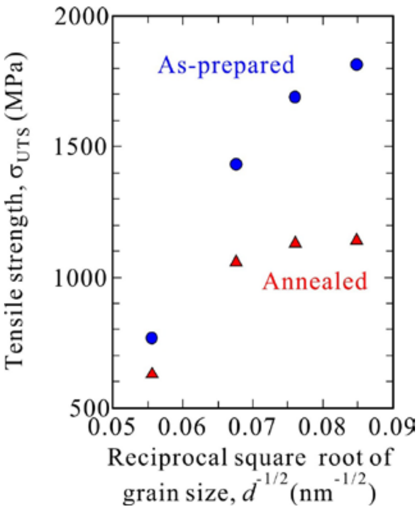


Figure 4. Grain size effect on tensile strength.

### 3.4. Fatigue crack propagation

The relation between fatigue crack propagation rate, d*a*/d*N*, and stress intensity factor range, $\Delta K$, is shown in Fig. 8. Effects of brightener additive in the electrodeposition solution are minimal in Paris law region. The effect of the force ratio, *R*, is not recognized in the region near threshold differently from

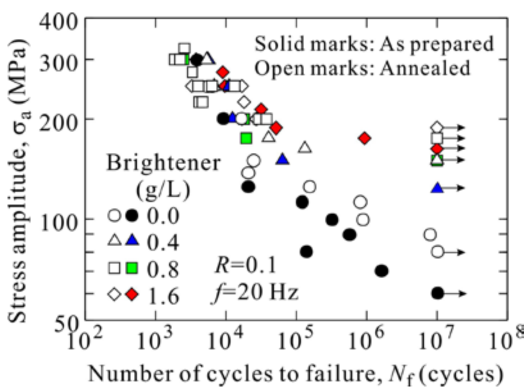


Figure 5. *S*–*N* curves.

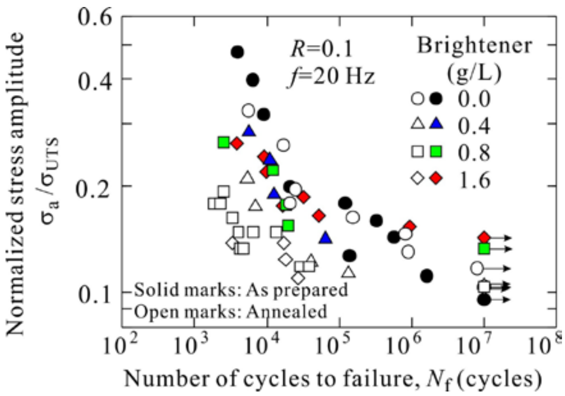


Figure 6. Normalized *S*–*N* curves.

conventional bulk alloys [5]. This may be come from the difference in roughness induced crack closure. Since the roughness of fracture surface is proportional to the grain size, it is very small for nanocrystalline materials. Actually, the force–displacement curve is almost linear and crack closure behavior was not observed, then the effective stress intensity factor range, $\Delta K_{eff}$, is the same value as the stress intensity factor range. It is well known that the d$a$/d$N$–$\Delta K_{eff}$ relationship is independent of the stress ratio for conventional bulk alloys [5].

The threshold stress intensity factor range, $\Delta K_{th}$, is smaller for the films fabricated with brightener additive in electrodeposition solution than that without brightener additive in the electrodeposition solution. Nakai et al. reported for a low-carbon steel that the threshold stress intensity factor range and the effective component of the range is smaller for smaller grain size, and the effect was explained by the blocked slip band model [5]. Then, the effect of amount of brightener additive in the electrodeposition solution on the threshold condition can be attributed to the effect of the grain size.

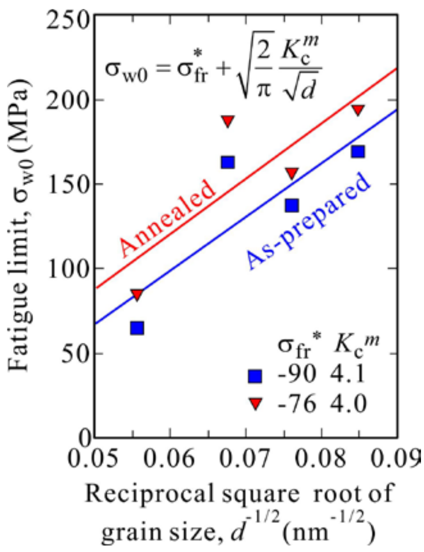


Figure 7. Grain size effect on fatigue limit.

## 4. Conclusions

The effect of amount of brightener additive in the electrodeposition solution on the tensile properties and the fatigue properties of nanocrystalline nickel thin film made by electrodeposition was examined, and following results were obtained.

(1) Tensile and fatigue strengths increased with decreasing grain size. Although annealing deteriorates the tensile strength, it improves the fatigue strength.

(2) The ratio of fatigue limit to the tensile strength for nanocrystalline thin film was much smaller than that for bulk metals.

(3) No effect of stress ratio on the d$a$/d$N$- $\Delta K$ relationship was observed. $\Delta K_{th}$ was lower for smaller grain size film. The crack closure was not observed for nanocrystalline thin film for $R$>0.

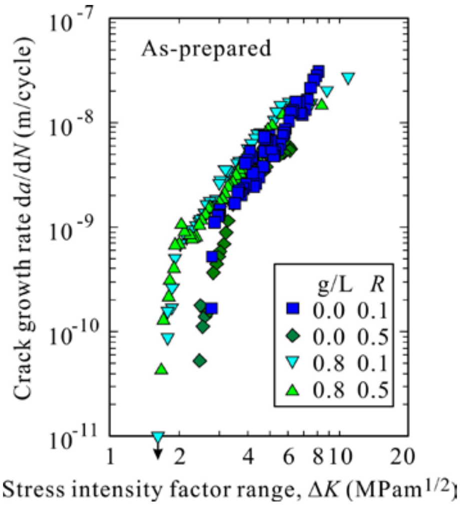


Figure 8. Stress ratio effect on crack propagation behavior.


## Acknowledgements

Support of this work through a Grant-in-Aid for Scientific Research (C) from Japan Society for the Promotion of Science under proposal number 18K03837 (Head investigator: Professor Yoshikazu Nakai, Kobe University) is gratefully acknowledged.


## References


[1] Hu, J., Shi, Y. N., Sauvage, X., Sha, G., Lu, K.,2017, Grain boundary stability governs hardening and softening in extremely fine nanograined metals, Science, 24, vol. 355, Issue 6331, pp. 1292-1296.

[2] Jang, D., Atzmona, M., 2006, Grain-boundary relaxation and its effect on plasticity in nanocrystalline Fe, Journal of Applied Physics, vol. 99, no. 8,183504.

[3] Rupert, T. J. , Trelewicz, J.R., Schuh, C.A., 2012. Grain boundary relaxation strengthening of nanocrystalline Ni–W alloys, Journal of Materials Research, vol. 27, pp. 1285-1294

[4] Matsui, I., Mori, H., Kawakatsu, T., Takigawa, Y., Uesugi, T., Higashi, K., 2014, Enhancement in mechanical properties of bulk nanocrystalline Fe–Ni alloys electrodeposited using propionic acid, Materials Science and Engineering: A, vol. 607, pp.505-510.

[5] Nakai, Y., Tanaka, K., Nakanishi, T., 1981, The effects of stress ratio and grain size on near-threshold fatigue crack propagation in low-carbon steel, Engineering Fracture Mechanics, vol. 15, no. 3-4, pp.291-302.

# Fatigue and Crack Growth under Variable-Amplitude Loading using Rainflow-on-the-Fly Methodology

J.C. Newman, Jr.[a]

[a]Mississippi State University, Mississippi State, MS, 39762, USA

E-mail address: newmanjr@ae.msstate.edu

**Abstract** – Fatigue of "engineered" materials, like alloys and steels, is basically fatigue-crack growth of small cracks nucleating at material micro-structural features, such as inclusions, voids and grain boundaries, and at micro-machining marks. Fatigue and crack-growth tests have been conducted on a 9310 steel under laboratory air and room temperature conditions. Large-crack growth data were obtained from compact, C(T), specimens over a very wide range in rates from threshold to fracture conditions for load ratios (R) of 0.1 to 0.95. New test procedures based on compression pre-cracking were used in the near-threshold regime because the current ASTM test method (load shedding) causes load-history effects and elevated thresholds. High load-ratio (R) data were used to approximate small-crack-growth-rate behavior. A crack-closure model, FASTRAN, was used to develop the baseline crack-growth rate curve. Fatigue tests were conducted on single-edge-notch-bend, SEN(B), specimens under both constant-amplitude loading and a Cold-Turbistan spectrum loading. Test results were compared to fatigue-life calculations or predictions made from the FASTRAN code using a micro-structural initial surface-flaw size (6-μm). The code was validated for both fatigue and crack-growth predictions. In general, predictions agreed well with the test data.

***Keywords:*** fatigue; crack growth; metallic materials; plasticity; crack closure; spectrum loading

## 1. Introduction

Fatigue-crack growth under variable-amplitude loading is composed of very complex crack-shielding mechanisms and damage accumulation due to cyclic plastic deformations around a crack front in metallic materials. Typically, "rainflow" methods are applied to these spectra to develop a load sequence that is used to compute damage accumulation and life because damage relations are, generally, a non-linear function of the crack-driving parameters. However, crack-tip damage is only a function of the current loading and load history (material memory). Loading in the future has no bearing on the current damage. The life-prediction code, FASTRAN [1], has a "rainflow-on-the-fly" methodology [2] to compute damage as the cyclic load history is applied; and there was no need to reorder the spectra.

The paper presents the results of large-crack-growth-rate tests conducted on compact, C(T), specimens made of 9310 steel [3] over a wide range of constant-amplitude loading to establish the baseline crack-growth-rate curve for fatigue and crack-growth analyses. The compression pre-cracking methods [4, 5] were used to generate test data in the near-threshold regime because the ASTM test method [6] causes load-history effects and slower rates than steady-state behavior. Both compression pre-cracking constant-amplitude (CPCA) and load-reduction (CPLR) methods were used. A crack-closure analysis was used to collapse the rate data from C(T) specimens into a fairly narrow band over many orders of magnitude in rates using a plane-strain constraint factor for low rates and modeled a constraint-loss regime to plane-stress conditions at high rates. For steels, small- and large-crack data (without load-history effects) agree. Thus, the high-R large-crack data in the near-threshold regime is a good estimate for small-crack behavior. A Two-Parameter Fracture Criterion [7] was used to characterize the fracture behavior. Fatigue tests were conducted on 9310 steel single-edge-notch-bend, SEN(B), [8] specimens under both constant-amplitude and Cold-Turbistan [9] spectrum loading. The test results were compared to the life calculations or predictions made using the FASTRAN code.

## 2. Material and specimen configurations

The Boeing Company provided a 9310 steel rod (150 mm diameter by 950 mm length) to Mississippi State University. C(T), SEN(B), and tensile specimens (B = 6.35 mm) were machined in the longitudinal direction (cracks perpendicular to longitudinal direction) and heat treated by procedures in Ref. 3. The yield stress, $\sigma_{ys}$, was 980 MPa, ultimate tensile strength, $\sigma_u$, was 1250 MPa, and modulus of elasticity was E= 209 GPa. Figure 1 shows C(T) and SEN(B) specimens with backface strain (BFS) gages used to monitor crack growth in the C(T) specimens and crack nucleation and growth in the SEN(B) specimens.

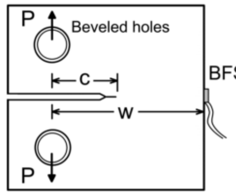


(a) Compact, C(T)

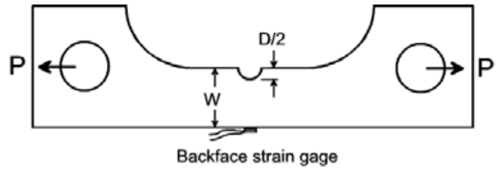


(b) Single-edge-notch bend, SEN(B)

**Figure 1**: Crack configurations tested and analyzed

### 3. "Rainflow-on-the-fly" methodology

The Christmas-Tree loading sequence is shown in Figure 2(a) and was designed to test the Rainflow-on-the-Fly option in FASTRAN. Rainflow methods are needed when damage rules (crack-growth-rate relations) are non-linear. Without Rainflow analyses, the difference in crack-growth lives for the sequence would be several orders on magnitude in error [2]. One block of loading is defined from point A to B, and the sequence was repeated until the final crack length was reached or the specimen failed. To simplify calculations and verification, the analytical crack-closure model in FASTRAN was turned off by intentionally setting the crack-opening stress, $S_o$, to a constant value of 50 MPa.

The sequence was applied to a very wide middle-crack tension, M(T), specimen. Figure 2(b) shows crack-growth increments calculated for each load cycle using Elber's crack-opening stress concept for an aluminum alloy: $dc/dN = 5e\text{-}10\ (\Delta K_{eff})^3$ where $\Delta K_{eff} = \Delta S_{eff} \sqrt{(\pi c)}\ F$. If the crack-opening stress is greater than the minimum stress, $S_{min}$, then $\Delta S_{eff} = S_{max} - S_o$. If $S_{min}$ is greater than the crack-opening stress, then $\Delta S_{eff} = S_{max} - S_{min}$. These equations apply only for "linear damage" (lines with solid blue symbol) and for loadings that do not require Rainflow methods. Diamond symbols show what a Rainflow method would give in crack extension. (Note that a cycle is defined as any minimum to maximum to minimum loading; and crack-growth damage only occurs during loading. The unloading part of the cycle causes reverse plastic deformations that may affect damage during the next load application.) FASTRAN with the rainflow subroutine gives the solid (black) symbols that match exactly what Rainflow method predicted.

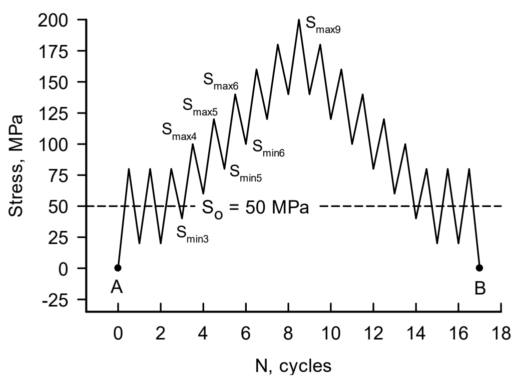


(a) Christmas-tree type loading

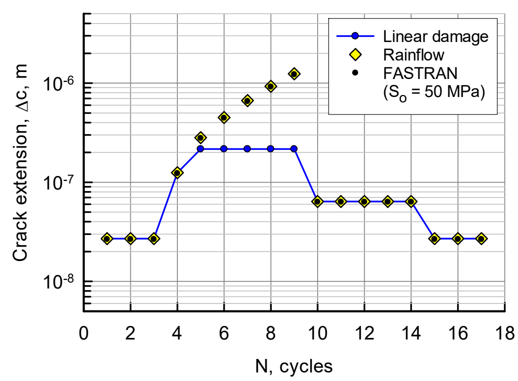


(b) Crack extension from Linear damage, Rainflow, and FASTRAN

**Figure 2**: Christmas-tree type loading and cyclic damage from various methods

Figure 3 shows the calculated crack-opening stresses from FASTRAN ($\alpha = 2$) using the full crack-closure model for Block 1 using the cycle-by-cycle option. These results are shown as the lines with circular symbols (red). Red symbols are the calculated crack-opening stresses at the minimum applied stresses. The model starts with a "zero" crack-opening stress and the opening stress increases as the crack grows and leaves plastically-deformed material in the wake of the crack tip. During cycles 3 to 9, the crack surfaces were fully open, but slightly closed at the minimum stress for cycle 2 and 10. At the minimum stress for cycle 17, point B, the crack-opening stress was slightly higher than at point A due to the plastic-deformation history.

Calculated crack-opening stresses for Block 1765, after 30,000 cycles, are shown as the blue symbols. Here cycle numbers are the 17 cycles in Block 1765. Crack surfaces are only open from cycles 5 to 9; and crack growth from cycles 1, 2, 3, 15, 16 and 17 are almost eliminated ($S_o$ near $S_{max}$ for each cycle).

For a constraint factor of 2, the stabilized crack-opening stress would be about 75 MPa for R = 0 loading with a maximum stress of 200 MPa, as shown by the current model calculations for cycles 1 to 3 and 14 to 16. These results are very important, in that, Rainflow analyses for fatigue-crack growth are a function of load history. Fortunately, current Rainflow analyses, used in the literature, would be conservative without considering load-history effects. But the accuracy of fatigue-crack-growth calculations under spectrum loading would be greatly improved with "Rainflow-on-the-Fly" methodology.

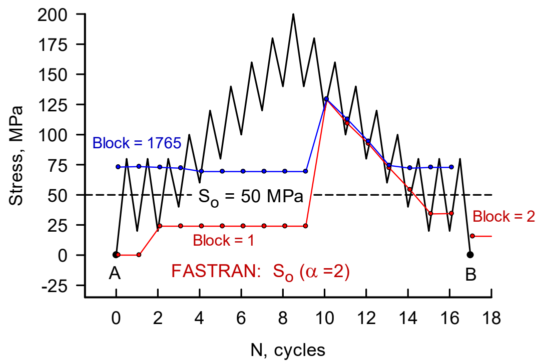


**Figure 3**: Calculated crack-opening stresses during many applications of the Christmas-tree loading

## 4. Fatigue-crack-growth tests

A crack-closure analysis was performed on fatigue-crack growth ($\Delta K$-rate) data [3] generated over a very wide range in the load ratio, R, to determine the $\Delta K_{eff}$-rate relation. Compression pre-cracking methods (CPCA and CPLR) were used. The lower vertical dashed line at $(\Delta K_{eff})_{th}$ is the estimated threshold for the steel [10]; and the upper vertical dashed line at $(\Delta K_{eff})_T$ is the location of constraint loss from plane-strain to plane-stress behavior [11]. Selection of the lower constraint factor, 2.5, was found to reasonably collapse the $\Delta K$-rate data onto an almost unique relation. In the threshold region, the lower R tests exhibited a rise in crack-opening loads as the $\Delta K$ level was reduced. Even the CPLR method showed a load-history affect, but not as much as the current ASTM procedure [6]. The upper constraint factor, 1.15, and constraint-loss range was selected to help fit spectrum crack-growth tests. The solid (blue) lines with circular (yellow) symbols shows the baseline crack-growth-rate curve for FASTRAN.

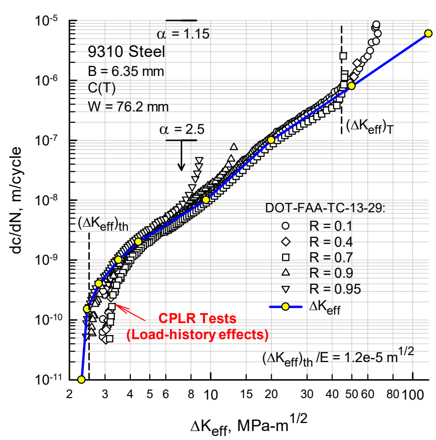


**Figure 4**: Effective stress-intensity factor against rate relation for 9310 steel

## 5. Fatigue behavior of notched specimens

Fatigue tests were conducted on SEN(B) specimens under: (1) constant-amplitude loading (R = 0.1) and (2) Cold-Turbistan+ loading. The semi-circular edge notch was chemically polished. The Cold-Turbistan+ spectrum was obtained from Ref. 9 but adding a constant load to make the overall R = 0.1 (compression loads not allowed on SEN(B) specimens). Figure 5(a) shows the constant-amplitude tests plotting $\sigma_{max}$ (notch root elastic stress) against cycles to failure ($N_f$). The square symbols are single-edge-notch tension, SEN(T), specimens [12]; whereas, the solid circular symbols are from the current study. A trial-and-error procedure was used to find the 6-µm semi-circular surface flaw at the center of the notch to fit the fatigue data. The solid curve shows calculated lives that used available crack-growth-rate data (rates ≥ 4e-11 m/cycle), which was for $\sigma_{max} \geq 980$ MPa. The dashed (blue) curve used the estimated $\Delta K_{eff}$-rate relation for rates below 4e-11 m/cycle (Fig. 4). Horizontal dashed (black) line is where $\Delta K_{eff} = (\Delta K_{eff})_{th} = 2.3$ MPa√m. Upper and lower bound calculations were made with 4- and 10-µm, respectively.

Figure 5(b) shows the test data (solid circular symbols) under the Cold-Turbistan+ spectrum. The open symbols are the retest of the two runout tests, but at higher applied notch elastic stress. FASTRAN predictions using the same 6-µm surface flaw fell at the lower bound of the test data using the baseline curve from Figure 4. If a threshold of 2.3 MPa√m (no crack growth) was selected, then the cycles to failure were near the upper bound of the test data. These results indicate that the selection of the baseline curve in Figure 4 for rates below 1e-10 m/cycle are very important.

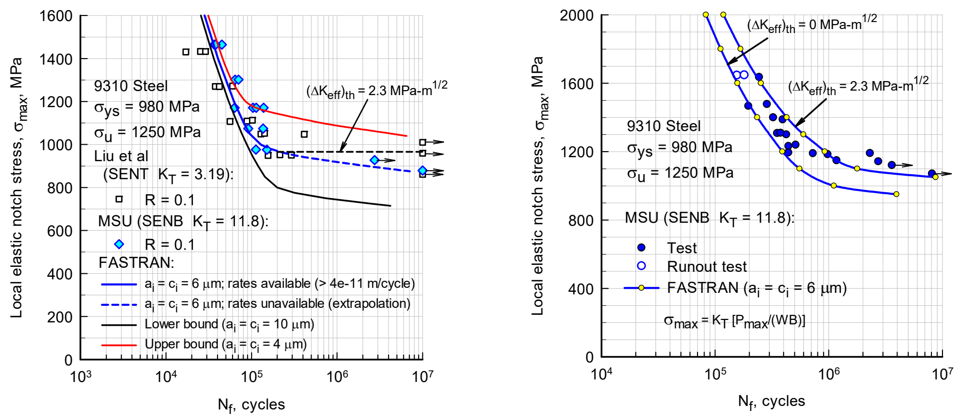


(a) Constant-amplitude loading (b) Cold-Turbistan+ loading

**Figure 5**: Measured and calculated stress-life behavior under constant- and variable-amplitude loading

## 6. Concluding remarks

Tests conducted on compact, C(T), and single-edge-notch-bend, SEN(B), specimens made of a 9310 steel under laboratory air and room temperature conditions indicated that fatigue behavior could be calculated under constant-amplitude (R = 0.1) loading and predicted under a Cold-Turbistan+ spectrum using crack-closure theory and an initial semi-circular surface flaw (6-µm). Rainflow-on-the-Fly methodology was validated on complex spectrum loadings and indicated that calculated damage was a function of load history and the usual Rainflow methods would not capture correct crack-growth damage.

## References

[1] Newman, J.C., Jr., "FASTRAN—A Fatigue Crack Growth Life Prediction Code based on the Crack-Closure Concept," Version 5.4 User Guide, Fatigue and Fracture Associates, LLC, Eupora, MS, 2013.

[2] Newman, J.C., Jr., "Rainflow-on-the-Fly Methodology: Fatigue-Crack Growth under Aircraft Spectrum Loading," Advanced Materials Research, 2014, Vol. 891-892, pp. 771-776.

[3] Newman, J.C., Jr., Yamada, Y., Ziegler, B.M., and Shaw, J.W., "Small- and Large-Crack Databases for Rotorcraft Materials," DOT/FAA/TC-13/29, June 2014.

[4] Newman, J.C., Jr., Schneider, J., Daniel, A. and McKnight, D., "Compression Pre-cracking to Generate Near Threshold Fatigue-Crack-Growth Rates in Two Aluminum Alloys," International Journal of Fatigue, Vol. 27, 2005, pp. 1432-1440.

[5] Newman, J.C., Jr., Ruschau, J.J., and Hill, M.R., "Improved Test Method for Very Low Fatigue-Crack-Growth-Rate Data," Fatigue and Fracture Engineering Materials and Structures, Vol. 34, No. 4, 2011, pp. 270-279.

[6] ASTM Standard Test Method for Measurement of Fatigue Crack Growth Rates, ASTM E-647, 2011; pp. 615-657.

[7] Newman, J.C., Jr., "Fracture Analysis of Various Cracked Configurations in Sheet and Plate Materials," Properties Related to Fracture Toughness. ASTM STP 605, 1976, pp. 104-123.

[8] Zeigler, B.M, "Fatigue and Fracture Testing and Analysis on Four Materials," Ph.D. Thesis, Mississippi State University, April 2011.

[9] ten Have, A.A., "Cold Turbistan - Final Definition of a Standardized Fatigue Test Loading Sequence for Tactical Aircraft Cold Section Engine Disc," Nationaal Lucht-en Ruimtevaartlaboratorium, NLR TR 87054 L, 1987.

[10] Newman, J.C., Jr., Kota, K. and Lacy, T.E., "Fatigue and Crack-Growth Behavior in a Titanium Alloy under Constant-Amplitude and Spectrum Loading," Engineering Fracture Mechanics, Vol. 187, 2018, pp. 211-224.

[11] Newman, J.C., Jr., "Effects of Constraint on Crack Growth under Aircraft Spectrum Loading," Fatigue of Aircraft Materials, A. Beukers, T. deJong, J. Sinke, A. Vlot and L. B. Vogelesang, 1992, pp. 83-109.

[12] Liu, J.Z. et al., "Crack growth behavior and fatigue-life prediction based on worst-case near-threshold data of a large crack for 9310 steel," Fatigue and Fracture of Engineering Materials and Structures Journal, Vol. 25, 2002, pp. 467-480.

# Fatigue Performance and Modeling of High Pressure Die Cast Aluminum Containing Defects

Ahmad Nourian-Avval and Ali Fatemi

*Department of Mechanical Engineering, University of Memphis, Memphis, TN, United States*

*E-mail address: nrnavval@memphis.edu , afatemi@memphis.edu*

**Abstract**

Defects are inevitable imperfections, which are formed in metallic components in many manufacturing techniques, including castings, additive manufacturing and powder metallurgy. These imperfections can significantly affect the fatigue performance of industrial components. Type of these defects depends on the manufacturing process. The common defects in castings are porosities and oxide films. It has been shown that fatigue failure in castings is almost always initiated from defects; however, elimination of these defects is neither always technically nor economically possible. So, the effect of these defects on fatigue performance of industrial component should be considered. On the other hand, many of the published works on fatigue behavior of defect containing materials have focused on uniaxial fatigue behavior, while the majority of these components are subjected to multiaxial stress states. In this study, the effect of defects on fatigue performance of high pressure die cast aluminum alloy, as an illustrative material containing defects, is investigated under different loading conditions. The defects were evaluated using both micro computed tomography and metallography, and different experimental fatigue tests were performed under uniaxial and multiaxial loading conditions. Fatigue life modeling and predictions were performed using statistical analysis of defects based on fracture mechanics approaches.

***Keywords**:* castings; defects; high pressure die cast aluminum; extreme value statistics; multiaxial fatigue; life prediction

## 1. Introduction

Investigation on the fatigue properties of defect containing materials has shown that not only the defects are the major source of scatter in fatigue properties of these materials, but also, defects shorten the fatigue lives of these materials by accelerating the crack nucleation under cyclic loadings [1–3]. On the other hand, producing complex geometries economically and efficiently has made casting an attractive manufacturing method for producing a large number of industrial components, especially casting of aluminum alloys, which has made it possible to produce lighter structures with improved fuel efficiency [4]. However, presence of defects, i.e. porosity, leads to high stress and strain concentrations within these components, which, facilitate crack nucleation under cyclic loadings [5, 6].

Studying the mechanisms of fatigue failure have shown that in the absence of defects, fatigue crack initiation occurs primarily from microstructural features, while in materials containing defects, the fatigue cracks mostly initiate from defects. It has been suggested that in pore free specimens, the total fatigue life consists of nucleation of fatigue cracks and propagation of the dominant fatigue crack [7, 8]; however, in specimens containing porosity, the number of cycles required for crack nucleation is negligible relative to the total fatigue life. Therefore, the fatigue life is dominated by crack propagation [9].

Fatigue life prediction of components containing defects can be performed following damage tolerant approach using crack growth rate models and the initial crack (flaw) size. In this approach, the defects can be considered as initial cracks within the specimens or components. To predict the fatigue life in defect containing materials, both long and short crack growth models have been used in literature. However, as the pores in cast aluminium alloys range between 100 - 1200 µm in size, the cracks initiated from these pores will be in the order of physically short cracks, which typically grow faster than long cracks. It has been shown that prediction of fatigue life using long crack growth models tend to be nonconservative. It has also been reported that the small crack growth is not a function of stress intensity factor, while it can be modelled by considering crack tip opening displacement (CTOD), which is related to cyclic plastic zone size, $r_p$, at the tip of the crack, which is, in turn, a function of both crack length $(a)$ and stress level $(\sigma_a)$. Therefore, the crack growth rate in physically small cracks can be approximated by [10]

$$da/dN = C(\sigma_a/\sigma_b)^n a \tag{1}$$

where $\sigma_b$ can be either yield strength $(\sigma_y)$ or ultimate strength $(\sigma_u)$, and *C* and *n* are material constants.

In this study, the fatigue performance of a high pressure die-cast aluminium alloy, as an illustrative material containing defects under different loading conditions, including uniaxial and multiaxial loading conditions is investigated. To achieve this goal, the defects within the specimens with two different size configurations were evaluated using both metallography and micro computed tomography. Furthermore, comprehensive fatigue tests were conducted to study the effect of specimen size, mean stress, stress gradient, and stress state. Fatigue life modelling and predictions were also performed using statistical analysis of defects based on fracture mechanics approaches.

## 2. Defect evaluation

In order to evaluate the defects within the specimens, both metallography and X-ray micro computed tomography was used. An example of the 2D and 3D images of the defects within the specimens are illustrated in Figure 1.

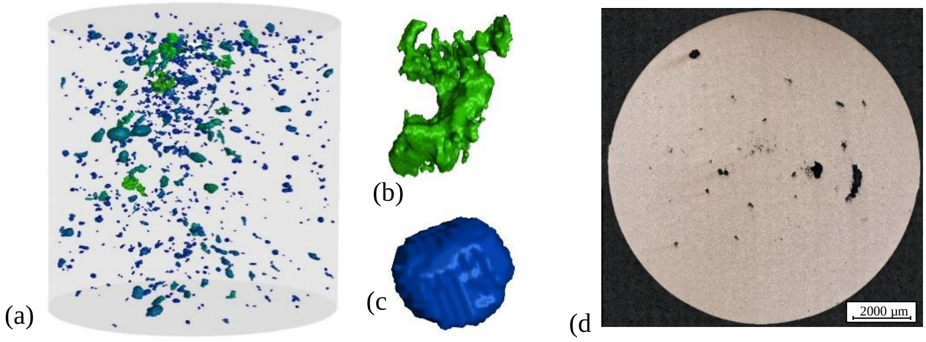


Figure 1. a) 3D pore distribution within a specimen obtained by X-ray CT scan, including b) shrinkage porosity and c) gas porosity, d) a typical 2D micrograph obtained by metallography

Extreme value statistics (EVS) were also performed on the defects size data obtained from metallography examination as well as x-ray µCT scan to estimate the maximum defect size within the specimens. The estimated maximum defect within the specimens will, then, be used in prediction of the fatigue life. The estimated maximum defect size within the specimens using 2D and 3D data is summarized in Table 1.

Table 1. Comparison of maximum defect within the specimens using 2D and 3D data with the maximum defect size observed on fracture surfaces of fatigue specimens

| maximum defect (µm) | Small specimens | Large specimens |
|---|---|---|
| EVS estimate using 2D data | 517 | 1186 |
| EVS estimate using 3D data | 603 | 1402 |
| Observed on fracture surfaces | 578 | 1274 |

## 3. Fatigue test results and comparisons

In order to investigate the fatigue behavior of this material, different experimental fatigue tests were performed under axial, rotating bending and multiaxial loading conditions. The results of different uniaxial fatigue tests are compared in figure 2a, showing the best fit line to the median fatigue life at a given stress level, while the horizontal bars indicate the scatter in fatigue life at different stress levels. As can be seen, the fatigue performance in small specimens is superior to that in large specimens due to higher stressed volume in large specimens, which increases the probability of existing defects larger than the critical defect size (20µm). Moreover, comparing the fatigue test results under axial and rotating bending conditions reveals that the fatigue life of the specimens under rotating bending fatigue test is higher than that in fully reversed axial loading condition. The reason is that in axial loading condition, the whole cross section is under uniform stress, while in rotating bending tests, there is a stress gradient and only the surface of the specimens is under the maximum stress. Therefore, the probability of existing a defect larger than the critical defect size is higher in the uniformly stressed region relative to the rotating bending loading condition.

The effect of mean stress was also examined by conducting axial fatigue tests under two stress ratios of 0 and -1. Comparing the fatigue behavior of the small specimens under different stress ratios indicates that in a given stress amplitude level, the fatigue life of the specimens under tension-tension condition is considerably shorter than that under fully reversed condition. In addition, in order to consider the mean stress effect in correlating the fatigue test results, Smith-Watson-Topper (SWT) parameter (i.e. $\sqrt{\sigma_a(\sigma_a+\sigma_m)}$ ) was found quite accurate in evaluating the fatigue life with the applied mean stress. The correlation of fatigue test results under uniaxial loading condition with and without mean stress is shown in Figure 2b.

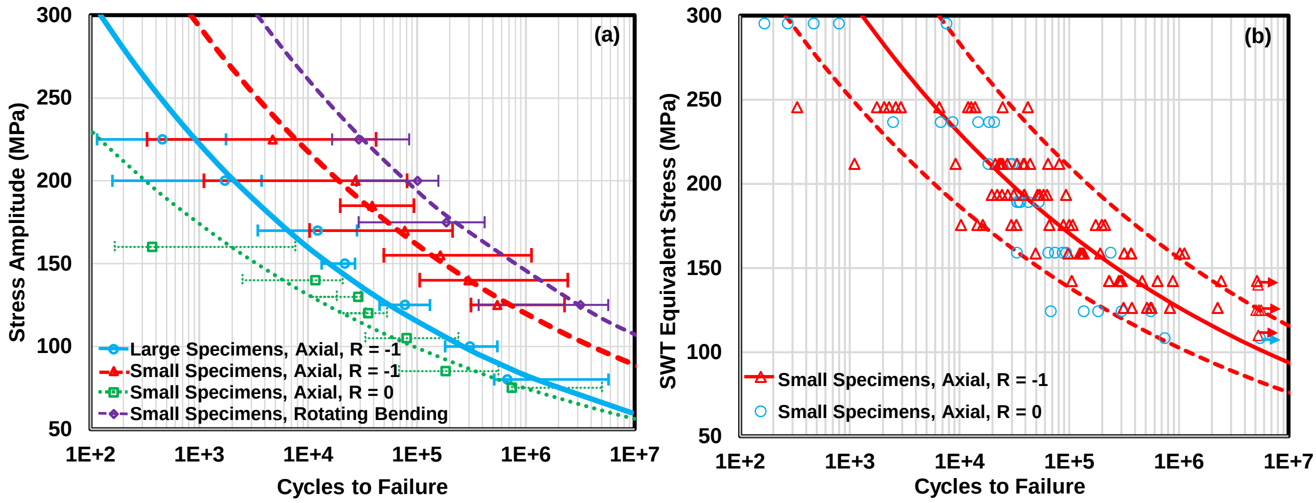


Figure 2. (a) Comparison of fatigue test results under uniaxial and rotating bending conditions evaluating the effect of specimen size, mean stress and stress gradient, (b) comparison of axial test data at different R ratios with SWT parameter

The comparison of the fatigue test results in large specimens under pure torsion as well as combined axial-torsion conditions is demonstrated in Figure 3. It was observed that the fatigue failure mechanism was propagation of fatigue cracks on the plane of maximum principal stress. This fact can also be seen by correlating the fatigue test results under axial and pure torsion using maximum principal stress criterion, although the volume effect causes the fatigue life to be slightly higher under pure torsion in comparison to axial loading condition. In addition, correlating the fatigue test results under different loading conditions showed that maximum principal stress was effective in evaluating the fatigue performance of this material under different loading conditions, as can be seen in Figure 3.

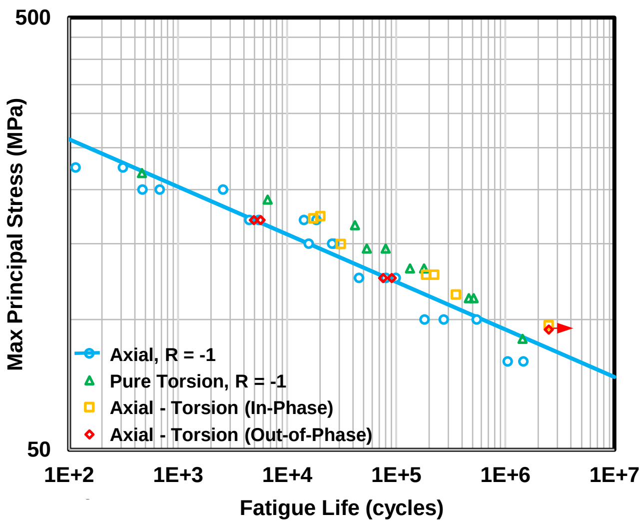


Figure 3. Correlation of fatigue tests results under axial, torsion, and multiaxial loading conditions based on maximum principal stress.

## 4. Fatigue life modeling and prediction

As was mentioned earlier, the fatigue life in defect containing materials is dominated by propagation of physically small cracks originated from defects. It was also proposed by Nisitani and Goto [10], that the small crack growth is a function of both crack length and stress level. However, in order to generalize the model to be applicable to all loading conditions, including mean stress as well as multiaxial stresses, Nisitani's model is modified as

$$\frac{da}{dN} = C\left[\left(E\frac{\sigma_{max}\varepsilon_a}{\sigma_u^2}\right)^n a\right]^t \qquad (2)$$

where $\sigma_u$ is the ultimate strength, $E$ is the modulus of elasticity, and $C$ and $n$ are material constants. Having used this model, the fatigue life of the specimens can be predicted by integrating from the observed fatal defect on fracture surfaces to the typical size of short cracks around $a_f = 2\,mm$. Comparison of the experimental fatigue life with the one estimated using the maximum defect estimated by extreme value statistics for different loading conditions is shown in Figure 4. As can be seen, the fatigue life estimated using the modified short crack growth model can predict the fatigue life for various loading conditions.

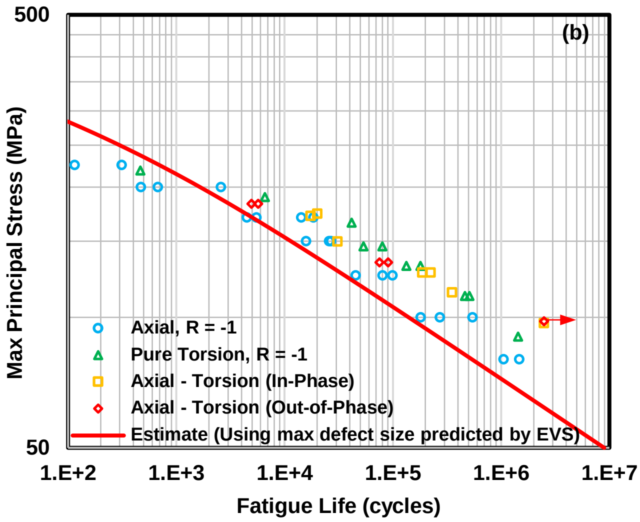


Figure 4. Comparison of experimental fatigue life with the estimated one using the maximum defects predicted by extreme value statistics

## Acknowledgements

The authors would like to thank Eaton Corporation for providing financial support and micro CT scan data for this study.

## References

[1] Avalle, M., Belingardi, G., Cavatorta, M. P., and Doglione, R., 2002, "Casting defects and fatigue strength of a die cast aluminium alloy: a comparison between standard specimens and production components", Int. J Fatigue, 24, 1-9.

[2] Boileau J. M. and Allison J. E., 2003, "The effect of solidification time and heat treatment on the fatigue properties of a cast 319 aluminum alloy," Metall. Mater. Trans. A, 34, 1807–1820.

[3] Wang Q., Apelian D., and Lados D., 2001, "Fatigue behavior of A356-T6 aluminum cast alloys. Part I. Effect of casting defects," J. Light Met., 1, 73–84.

[4] Campbell J., Complete casting handbook : metal casting processes, metallurgy, techniques and design, 2011 .

[5] Fan J., McDowell D., Horstemeyer M., Gall K., 2003, "Cyclic plasticity at pores and inclusions in cast Al–Si alloys," Engineering Fracture Mechanics, 70(10), 1281-1302.

[6] Gao Y. X., Yi J. Z., Lee P. D., and Lindley T. C., 2004, "The effect of porosity on the fatigue life of cast aluminium-silicon alloys", Fatigue Fract. Eng. Mater. Struct., 27, 559–570.

[7] Couper, M. J., Neeson A. E., and J. R. Griffiths, 1990, "Casting defects and the fatigue behaviour of an aluminium casting alloy." Fatigue Fract. Eng. Mater. Struct., 13, 213-227.

[8] Shiozawa, K. B., Tohda, Y., and Sun, S. M., 1997, "Crack initiation and small fatigue crack growth behaviour of squeeze-cast Al-Si aluminium alloys", Fatigue Fract. Eng. Mater. Struct., 20, 237-247.

[9] Wang Q. G. and P. E. Jones, 2007, "Prediction of Fatigue Performance in Aluminum Shape Castings Containing Defects," Metall. Mater. Trans. B, 38, 615–621.

[10] Nisitani H., Goto M., 1986, "A small-crack growth law and its application to the evaluation of fatigue life," EGF1, 1986.

# Thermal formulation of singular regions for orthotropic and isotropic materials

F. Ernesto Penado[a]

[a]Department of Mechanical Engineering, Northern Arizona University, Flagstaff, AZ 86011, USA

E-mail address: Ernesto.Penado@nau.edu

**Abstract** A method to formulate an asymptotic elasticity solution for singular regions in orthotropic materials is presented for the thermal case. In the vicinity of material and geometric singularities, approximate methods such as finite elements fail to converge and procedures to improve these solutions become necessary. The results presented herein can be used in conjunction with approximate numerical techniques for the determination of stress intensity factors in composite bonded joints, cracked bimaterial interfaces, or a junction of dissimilar materials under mechanical and thermal loading. The thermal displacement and stress fields in the near-region of the singularity are developed by means of eigenfunction expansions including both singular and nonsingular terms. The thermal elasticity solution for isotropic materials as the limiting case of the orthotropic solution is also obtained. The formulations are applicable to bonded joints with interfacial or interlaminar cracks, geometric and material discontinuities, and any combination of mechanical and thermal loading. The detailed formulation presented provides an essential component in the application of finite elements in the determination of generalized intensity factors in composites or other dissimilar materials under thermal loading. Formulation results for orthotropic materials, including the limiting case of isotropic materials, are compared with published and closed form results that use different formulations, and excellent agreement is observed. Furthermore, the existence of stress singularities of the form k·ln(r), in addition to $k^*\cdot r^{\lambda}$, is investigated and discussed.

***Keywords:***
Bimaterial interface; thermoelasticity; orthotropic materials; composite materials; eigenfunction expansion; singular stresses

## 1. Introduction

Cracks and delaminations are common examples of failures in laminated composite structures. Such failures can initiate at cracks and notches that may exist at the edge of ply or bonded joint interfaces. In order to correctly predict failure of these structures, the determination of singular stresses at interface corners in composite structures is essential. However, due to the complexities inherent in this type of problems, the analysis is generally very difficult to perform. For example, in the neighborhood of material and geometric singularities, approximate methods such as finite elements fail to converge and procedures to improve these solutions become necessary. Recently, a practical procedure to determine the complete singular stress field at points of singularity in cracked orthotropic materials has been demonstrated for structures under mechanical loading [1,2]. A key requirement of this method is the availability of a local elasticity solution near the point of singularity. In this paper, using eigenfunction expansions we consider the solution for a notch or crack at the interface between two orthotropic or isotropic materials, or a combination of the two. The loading consists of a uniform temperature distribution and possible mechanical loads. Thermal stresses develop due to the mismatch of material properties at the interface. The results obtained are compared with published and closed form results that use different formulations. Furthermore, the existence of stress singularities of the form k·ln(r), in addition to $k^*\cdot r^{\lambda}$, is investigated and discussed.

## 2. Formulation of the Problem and Basic Equations

Consider a bimaterial wedge as shown in Fig. 1. For a rectangular coordinate system $x_i$, (i=1,2,3), let $u_i$, $\sigma_{ij}$, and $\varepsilon_{ij}$ (i,j=1,2,3) be, respectively, the components of displacement, stress, and strain. The strain-displacement and equilibrium equations become respectively:

$$\varepsilon_{ij} = \left(\partial u_i / \partial x_j + \partial u_j / \partial x_i\right)/2; \qquad \partial\sigma_{i1}/\partial x_1 + \partial\sigma_{i2}/\partial x_2 = 0 \tag{1,2}$$

Furthermore, generalized Hooke's law for an orthotropic, linear elastic material subject to a uniform temperature change, ΔT, is given by

$$\{\sigma\} = [C]\left(\{\varepsilon\} - \{\alpha\}\Delta T\right); \quad \{\varepsilon\} = [S]\{\sigma\} + \{\alpha\}\Delta T \tag{3,4}$$

where $[C]=[S]^{-1}$ and $[S]$ are, respectively, the stiffness and compliance matrices, $\{\alpha\}=[\alpha_1\ \alpha_2\ \alpha_3\ 0\ 0\ 0]^T$ are the thermal expansion coefficients, and

$$\{\sigma\} = \text{stresses} = \left[\sigma_{11} \quad \sigma_{22} \quad \sigma_{33} \quad \tau_{23} \quad \tau_{13} \quad \tau_{12}\right]^T$$
$$\{\varepsilon\} = \text{strains} = \left[\varepsilon_{11} \quad \varepsilon_{22} \quad \varepsilon_{33} \quad \gamma_{23} \quad \gamma_{13} \quad \gamma_{12}\right]^T \tag{5,6}$$

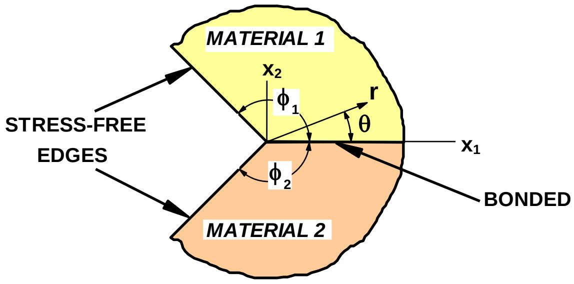


**Figure 2**: Bimaterial wedge used in the analysis.

In terms of the usual engineering constants, $E_i$, $\nu_{ij}$, and $G_{ij}$ (i,j=1,2,3), the entries of the compliance matrix for an orthotropic material are $S_{ii}=1/E_i$, $S_{ij}=-\nu_{ij}/E_i=-\nu_{ji}/E_j$ ($i\neq j$), $S_{44}=1/G_{23}$, $S_{55}=1/G_{13}$, $S_{66}=1/G_{12}$, all other entries are zero. Assuming generalized plane strain conditions in the $x_1$-$x_2$ plane, the displacements, strains, and stresses are independent of $x_3$, and $\varepsilon_{33}=0$.

Replacing (1) into (3) and (2) provides the equilibrium equations in terms of displacements:

$$C_{11}\,\partial^2 u_1/\partial x_1^2 + C_{12}\,\partial^2 u_2/\partial x_1 \partial x_2 + C_{66}\left(\partial^2 u_1/\partial x_2^2 + \partial^2 u_2/\partial x_1 \partial x_2\right) = 0$$
$$C_{66}\left(\partial^2 u_1/\partial x_1 \partial x_2 + \partial^2 u_2/\partial x_1^2\right) + C_{12}\,\partial^2 u_1/\partial x_1 \partial x_2 + C_{22}\partial^2 u_2/\partial x_2^2 = 0 \tag{7,8,9}$$
$$C_{55}\,\partial^2 u_3/\partial x_1^2 + C_{44}\,\partial^2 u_3/\partial x_2^2 = 0$$

We note that the equations for $u_1$ and $u_2$, corresponding to the in-plane problem, are decoupled from the equation for $u_3$, which corresponds to the out-of-plane problem. From here on, only the in-plane problem will be considered. Based on the results in [3] and [4], we assume the following solution for the in-plane problem:

$$u_i = \zeta_i\, Z^{1+\lambda}/(1+\lambda), \quad (i=1,2) \tag{10}$$

where $Z=x_1+\mu\cdot x_2$, $\mu$ represents the eigenvalues of the elasticity constants (to be determined from equilibrium, Eq. 7,8), $\zeta_i$ are functions of $\mu$, and $\lambda$ are eigenvalues to be determined from the local boundary conditions. Substituting (10) into (7) and (8) leads to the following homogeneous system of equations:

$$\begin{bmatrix} C_{11}+C_{66}\mu^2 & (C_{12}+C_{66})\mu \\ (C_{12}+C_{66})\mu & C_{66}+C_{22}\mu^2 \end{bmatrix} \begin{Bmatrix} \zeta_1 \\ \zeta_2 \end{Bmatrix} = \begin{Bmatrix} 0 \\ 0 \end{Bmatrix} \tag{11}$$

For a nontrivial solution, the determinant of the matrix of coefficients must be zero, leading to a quartic equation in $\mu$. Substitution of (10) into (1) and (3) results in

$$\begin{Bmatrix} \sigma_{11} \\ \sigma_{22} \\ \tau_{12} \end{Bmatrix} = \begin{Bmatrix} C_{11}\zeta_1 + \mu C_{12}\zeta_2 \\ C_{12}\zeta_1 + \mu C_{22}\zeta_2 \\ \mu C_{66}\zeta_1 + C_{66}\zeta_2 \end{Bmatrix} Z^{\lambda} - \begin{Bmatrix} \beta_{11} \\ \beta_{22} \\ \beta_{12} \end{Bmatrix} \Delta T \tag{12}$$

where $\{\beta\}$=thermal moduli=$[C]\{\alpha\}$. For the special case of an isotropic material in the $x_1$-$x_2$ plane with $E_1=E_2=E_3=E$, $\nu_{23}=\nu_{13}=\nu_{12}=\nu$, $G_{23}=G_{13}=G_{12}=G$, and $\alpha_1=\alpha_2=\alpha_3=\alpha$, the solution cannot be obtained simply by inserting isotropic material properties into the equations. In this case, instead of (10) the following new solution must be used [4]:

$$u_i = \zeta_i\, Z^{1+\lambda}/(1+\lambda) + \left[d\left(\zeta_i\, Z^{1+\lambda}\right)/d\mu\right]/(1+\lambda), \quad (i=1,2) \tag{13}$$

The complete asymptotic solutions for displacements and stresses for each material can be obtained by superposition of the solutions for each individual $\lambda$. Converting the results to cylindrical coordinates with $x_1=r\cdot\cos\theta$ and $x_2=r\cdot\sin\theta$, the resulting equations are as follows:

$$u_r^{(i)} = \sum_{m=1}^{M} a_m \left[ \frac{r^{1+(\lambda)_m}}{1+(\lambda)_m} \sum_{k=1}^{4} A_{km}^{(i)} (F_r^{(i)})_{km} \right], \quad u_\theta^{(i)} = \sum_{m=1}^{M} a_m \left[ \frac{r^{1+(\lambda)_m}}{1+(\lambda)_m} \sum_{k=1}^{4} A_{km}^{(i)} (F_\theta^{(i)})_{km} \right] \tag{14,15}$$

$$\sigma_r^{(i)} = \sum_{m=1}^{M} a_m \left[ r^{(\lambda)_m} \sum_{k=1}^{4} A_{km}^{(i)} (G_r^{(i)})_{km} \right] - \beta_r^{(i)} \Delta T, \quad \sigma_\theta^{(i)} = \sum_{m=1}^{M} a_m \left[ r^{(\lambda)_m} \sum_{k=1}^{4} A_{km}^{(i)} (G_\theta^{(i)})_{km} \right] - \beta_\theta^{(i)} \Delta T \tag{16,17}$$

$$\tau_{r\theta}^{(i)} = \sum_{m=1}^{M} a_m \left[ r^{(\lambda)_m} \sum_{k=1}^{4} A_{km}^{(i)} (G_{r\theta}^{(i)})_{km} \right] - \beta_{r\theta}^{(i)} \Delta T \tag{18}$$

where the superscript i=1,2 is used to denote each material region; M is the number of terms in the truncated infinite series; $\beta_r^{(i)}$, $\beta_\theta^{(i)}$, $\beta_{r\theta}^{(i)}$ are the cylindrical components of the thermal moduli; $a_m$'s are multiplicative constants associated with the in-plane eigenvectors; $F_{ij}$, $G_{ij}$ are defined explicitly in [3] for both orthotropic and isotropic materials; and $(\lambda)_m$, $A_{km}^{(i)}$ can be determined from the continuity and free edge boundary conditions. Moreover, the determination of the $a_m$'s requires the application of remote boundary conditions, which can include both mechanical and thermal loading, but this is not considered herein. For the wedge shown in Fig. 1, the boundary conditions to be satisfied near the vertex are:

$$\text{stress-free faces:} \quad \sigma_\theta^{(1)}(r,\phi_1) = \tau_{r\theta}^{(1)}(r,\phi_1) = \sigma_\theta^{(2)}(r,\phi_2) = \tau_{r\theta}^{(2)}(r,\phi_2) = 0 \tag{19}$$

$$\text{interface:} \quad \sigma_\theta^{(1)}(r,0) = \sigma_\theta^{(2)}(r,0), \quad \tau_{r\theta}^{(1)}(r,0) = \tau_{r\theta}^{(2)}(r,0), \quad u_r^{(1)}(r,0) = u_r^{(2)}(r,0), \quad u_\theta^{(1)}(r,0) = u_\theta^{(2)}(r,0) \tag{20}$$

Substituting (14)-(18) into (19) and (20) results in the following linear system of equations:

$$r^\lambda \left[ K(\lambda) \right] \{A\} = \Delta T \{b\} \tag{21}$$

where [K] is an 8x8 matrix whose elements depend on $\lambda$, {b} is an 8x1 column matrix whose elements depend on the entries of $\{\beta^{(1)}\}$ and $\{\beta^{(2)}\}$, and {A} is an 8x1 column matrix containing $A_{km}^{(i)}$. We note that the left hand side of (21) depends on r while the right hand side is constant, so the only way to satisfy this equation for all r is if we let $\lambda$=0. This results in the following system:

$$\left[ K(0) \right] \{A\} = \Delta T \{b\} \tag{22}$$

In addition to the particular solution with a non-zero right hand side, homogeneous solutions for {A} are possible if $|K(\lambda)|=0$. We find that $\lambda$=0 always satisfies this condition but is not the only root. Moreover, the system given by (22) with a zero right hand side has been considered in detail elsewhere [3,5] and only the particular solution to this system is considered here.

## 3. Results and Discussion

Since $\lambda$=0 is a root of $|K(\lambda)|=0$, [K(0)] is singular and a particular solution for {A} exists only if the rank of [K(0)] is equal to the rank of the augmented matrix $[K(0)|\Delta T\{b\}]$ [6]. In this case, the stresses obtained are uniform [7]. On the other hand, if this relationship does not hold the system is inconsistent, a uniform stress due to a uniform temperature change $\Delta T$ does not exist, and a different solution consisting of the derivative of (14)-(18) with respect to $\lambda$ must be used [7]. This leads to $\theta$-dependent stresses and a logarithmic singularity of the form $k \cdot \Delta T \cdot \ln(r)$ if $k \neq 0$. For isotropic materials, it was found that for wedge angles $\phi_1 = -\phi_2 = 90°$, the system (22) is consistent and the stresses are uniform. However, for angles other than 90° or 180°, the system is inconsistent and using the derivatives of (14)-(18) with respect to $\lambda$ in (22) results in the new 16x16 system

$$\begin{bmatrix} [K(0)] & [0] \\ [K'(0)] & [K(0)] \end{bmatrix} \begin{Bmatrix} \{A\} \\ \{A'\} \end{Bmatrix} = \Delta T \begin{Bmatrix} \{0\} \\ \{b\} \end{Bmatrix} \tag{23}$$

where the primes denote derivatives with respect to $\lambda$. Characteristic dimensionless stresses are now defined as

$$\sigma_0{*} = 2\sigma_\theta\big|_{\theta=0} / \left[ \Delta T \left( \alpha^{(2)} - \alpha^{(1)} \right) \left( E^{(1)} + E^{(2)} \right) \right], \quad \tau_0{*} = 2\tau_{r\theta}\big|_{\theta=0} / \left[ \Delta T \left( \alpha^{(2)} - \alpha^{(1)} \right) \left( E^{(1)} + E^{(2)} \right) \right] \tag{24}$$

and their variation is plotted in Fig. 2a with respect to the moduli of elasticity ratio for $\phi_1 = -\phi_2 = 90°$, $E^{(1)}$=40.61 msi, $\nu_1 = \nu_2 = 0.3$, and in Fig. 2b with respect to the wedge angle for $E^{(2)}/E^{(1)}=2$. Results from equations in [8] are also plotted for verification, showing excellent agreement with the present results. Note in Fig. 2 that $\sigma_0^*$ and $\tau_0^*$ approach infinity for certain values of $E^{(2)}/E^{(1)}$ or $\phi$. However, as pointed out in [8], this does not imply a stress singularity, since the stress intensity factor associated with $\lambda$=0 also approaches infinity and the ratio remains bounded.

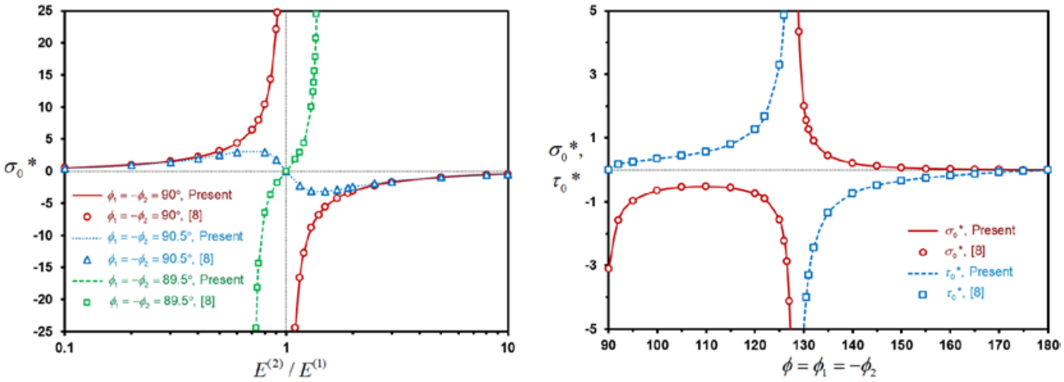


(a) (b)

**Figure 2**: Characteristic dimensionless stresses as a function of (a) Moduli ratio, and (b) Wedge angle for $E^{(2)}/E^{(1)}=2$.

For orthotropic materials, the interface of a [0/90] composite with plies made of the material used in [9] are considered, resulting in the following equivalent orthotropic material properties:

$$E_1^{(1)} = 20 \text{ msi},\ E_2^{(1)} = E_3^{(1)} = 2.1 \text{ msi},\ G_{23}^{(1)} = G_{13}^{(1)} = G_{12}^{(1)} = 0.85 \text{ msi},\ \nu_{23}^{(1)} = \nu_{13}^{(1)} = \nu_{12}^{(1)} = 0.21$$
$$\alpha_1^{(1)} = 0.2\times10^{-6}/°\text{F},\ \alpha_2^{(1)} = \alpha_3^{(1)} = 16\ \times10^{-6}/°\text{F} \tag{25}$$

$$E_1^{(2)} = E_2^{(2)} = 2.1 \text{ msi},\ E_3^{(2)} = 20 \text{ msi},\ G_{23}^{(2)} = G_{13}^{(2)} = G_{12}^{(2)} = 0.85 \text{ msi},\ \nu_{12}^{(2)} = 0.21,\ \nu_{23}^{(2)} = \nu_{13}^{(2)} = 0.0221$$
$$\alpha_1^{(2)} = \alpha_2^{(2)} = 16\times10^{-6}/°\text{F},\ \alpha_3^{(2)} = 0.2\ \times10^{-6}/°\text{F} \tag{26}$$

It was found for $\phi_1=-\phi_2=90°$ that the system (22) is consistent and the stresses are uniform. However, for any other wedge angles both systems (22) and (23) are inconsistent, indicating that a new system must be found in a similar way to (23) but with higher derivatives with respect to $\lambda$. The results for the stresses are shown in Table 1. For the special case of uniform stresses, an alternative closed form solution is possible and was derived using the approach in [7]. The closed form results are also shown in Table 1.

**Table 1**: Verification of results for stresses of the orthotropic wedge with $\phi_1=-\phi_2=90°$.

| Method | Stresses for $\phi_1=-\phi_2=90°$ (psi/°F) | | | | | |
|---|---|---|---|---|---|---|
| | $\sigma_{11}^{(1)}/\Delta T$ | $\sigma_{11}^{(2)}/\Delta T$ | $(\sigma_{22}^{(1)}=\sigma_{22}^{(2)})/\Delta T$ | $\sigma_{33}^{(1)}/\Delta T$ | $\sigma_{33}^{(2)}/\Delta T$ | $(\tau_{12}^{(1)}=\tau_{12}^{(2)})/\Delta T$ |
| Present | 0 | 0 | 173.06 | 32.343 | 2.7434 | 0 |
| Closed form | 0 | 0 | 173.06 | 32.343 | 2.7434 | 0 |

## 4. Conclusions

A method to formulate an asymptotic elasticity solution for singular regions in orthotropic and isotropic materials was presented for the thermal case. The results obtained were compared with published and closed form results that use other formulations and excellent agreement was found. Furthermore, the existence of stress singularities of the form $k\cdot\ln(r)$, in addition to $k^*\cdot r^\lambda$, was investigated and discussed, but no singularities of this type were found for the geometries and materials considered since k=0 in these cases.

## References

[1] Penado, F. E., 2018. Analysis of the partially closed interface crack in orthotropic materials. *Journal of Thermoplastic Composite Materials*, Vol. 31, pp 820–836.

[2] Penado, F. E., 2018. Fracture parameter determination for the orthotropic interface crack with friction. *Engineering Fracture Mechanics*, Vol. 204, pp 542–556.

[3] Penado, F. E., 2000. Determination of stress intensity factors in cracked bonded composite joints. *Journal of Thermoplastic Composite Materials*, Vol. 13, pp 174–189.

[4] Ting T. C. T. and Chou S. C., 1981. Edge singularities in anisotropic composites. *International Journal of Solids and Structures*, Vol. 17, pp 1057–1068.

[5] Penado, F. E., 2000. Analysis of singular regions in bonded joints. *International Journal of Fracture*, Vol. 125, pp 1–25.

[6] O'Neil, P. V., 1983. *Advanced Engineering Mathematics*. Wadsworth Publishing Company, Belmont, California, p. 494.

[7] Zwiers, R. I., Ting T. C. T. and Spilker R. L., 1982. On the logarithmic singularity of free-edge stress in laminated composites under uniform extension. *Journal of Applied Mechanics*, Vol. 49, pp 561–569.

[8] Munz, D., Fett, T. and Yang, Y. Y., 1993. The regular stress term in bonded dissimilar materials after a change in temperature. *Engineering Fracture Mechanics*, Vol. 44, pp 185–194.

[9] Wang, A. S. D. and Crossman, F. W., 1977. Edge effects on thermally induced stresses in composite laminates. *Journal of Composite Materials*, Vol. 11, pp 300–312.

# Analysis and Modeling of the Effect of Defects on Fatigue Performance of L-PBF Additive Manufactured Metals

Niloofar Sanaei[a], Ali Fatemi[a,b,]

[a]Mechanical, Industrial and Manufacturing Engineering, University of Toledo, Toledo, OH 43606, USA
[b]Mechanical Engineering, University of Memphis, Memphis, TN 38152, USA

*E-mail address:* afatemi@memphis.edu

**Abstract** Additive Manufacturing (AM) technologies are being developed to generate intricate and unique components with new levels of conformability. To achieve industrial standards for critical load carrying applications under typical cyclic loadings, AM parts should provide the required fatigue strength. Fatigue performance is greatly influenced by the existence of surface and internal defects since fatigue cracks often start at points of stress concentrations. In this work an overview of the process-structure-property relationships and how processing parameters, and post processing conditions affect the microstructure and defect characteristics that ultimately contribute to the fatigue performance of Ti-6Al-4V and 17-4 PH, is provided. This includes evaluating the effect of processing and post processing conditions on internal defects and surface roughness, analysis of distributions of the defect characteristics based on their location in the AM specimen, and investigating the effect of these surface and internal defects on fatigue performance. Finally, using fracture mechanics and considering both internal defects and surface roughness, fatigue life predictions are presented and compared with experimental data.

***Keywords**:* Additive Manufacturing; Fatigue Performance; Defects; Surface Roughness; Powder Bed Fusion (PBF)

## 1. Introduction

Metal AM components in aerospace and biomedical applications should be designed to work under complex loadings and in harsh environmental conditions. Acceptable mechanical properties and specifically fatigue performance of these parts which is significantly influenced by AM intrinsic defects is, therefore, very important. Reliable and appropriate defect characterization and analysis methods should be implemented for safety-critical parts. Powder Bed Fusion (PBF) with two main power sources, lasers and electron beams, is currently the most commonly used AM technique for metals. In this study L-PBF Ti-6Al-4V and 17-4 PH specimens are discussed, although the performed analyses may also be used for other metals with similar defect contents.

A favorable environment is created during metal PBF AM for defect formation with the rapid heating and cooling cycles, localized heating, and powdered material as the feedstock. This process usually creates gas bubbles and leaves small cracks, un-melted particles, and Lack of Fusion (LOF) regions. Examples of these defects and their characteristics which highly depend on the material, process parameters, and post-processing thermo-mechanical treatments can be seen in Figure 1 [1].

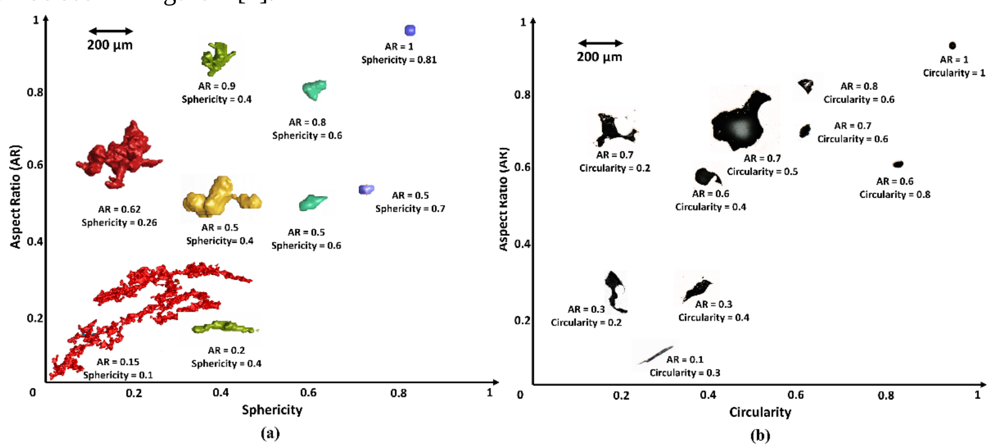


**Figure 1**Visualization of L-PBF Ti-6Al-4V defects gathered from (a) micro-CT, and (b) optical microscopy [1].

As-built Ti-6Al-4V AM parts generally have a finer microstructure compared to their wrought counterparts [2]. Moreover, the effect of defects is usually insignificant on performance of AM parts under static loading and, therefore, these parts generally provide a good static strength, although defects typically cause a lower ductility and fracture toughness [3]. Fatigue performance of AM metals on the other hand is significantly influenced by the existence of intrinsic AM defects since fatigue is a local phenomenon and fatigue cracks usually start at these defects due to the high stress concentrations [4]. The rough surface is another intrinsic feature of AM metals due to the layer by layer manufacturing strategy, partially melted powder particles attached to the surface, and the stair-stepping effect due to the geometry of the part. Surface roughness might be intentionally created for applications that require biointegration, but it is detrimental to fatigue performance since sharp surface features act as crack initiation sites [5].

This paper provides an overview of the authors recent works on the effect of defects on fatigue performance of AM Ti-6Al-4V and 17-4 PH. The effect of processing and post-processing conditions on internal defects and their distribution and on surface roughness and consequently on fatigue performance for various microstructures is analyzed. Finally, considering both internal defects and surface roughness, fatigue life predictions using a fracture mechanics-based approach will be presented and compared with experimental data.

## 2. Defects and Analysis of Their Variability

Variability of defects obtained from micro-CT scans in tubular specimens with outer diameter of ~15 mm and thickness of ~1.2 mm manufactured for multiaxial fatigue testing were analyzed. A 10 mm length of the gage section of L-PBF Ti-6Al-4V specimens manufactured by AM250 and M290 machines and 17-4 PH specimens manufactured by a M290 machine with manufacturer recommended parameters were used. Ti-6Al-4V specimens where annealed, or (Hot Isostatic Press) HIPed and 17-4 PH specimens were heat treated. Specimens with both as-built and machined surface conditions were used. 3D reconstructed volumes were divided in various directions. To examine the defect distributions along the height, the volume was divided into four equal volumes along the build height. To check dispersion of defects around the specimen axis of symmetry, it was divided into equal quadrants around the specimen axis. Finally, the gage section was divided into four shells with equal thickness to examine distribution of defects through wall thickness. To statistically determine any significant variability in defect distributions, the two sample Kolmogorov-Smirnov (K-S) statistical test was used. Diameter, volume, projected area, and sphericity as the most important defect characteristics were examined based on their location in each specimen. For each division method, distribution for each characteristic in each control volume was compared with distributions from the other three control volumes using K-S test.

No significant variation between the defect distributions along the 10 mm built height for any condition was observed. Significant difference between defect diameter distributions around specimen axis for AM250 specimens which contained many large LOF defects in both as-built and machined surface conditions was observed. This means the critical defects were mostly concentrated on one side of the specimen. No significant variability around M290 annealed specimens with small round defects was observed before and after HIPing. Concentration of defects were observed closer to inner and outer surfaces in as-built surface specimens. More uniform distribution of defects was observed after removing the near surface defects by surface machining. The highest volume fraction of defects in as-built surface specimens was observed in the inner or outer surface shells.

## 3. Effect of Internal Defects on Fatigue Performance

The number of defects in gage section of the specimen along with fatigue performance for various conditions were compared. AM250 Ti-6AL-4V annealed as-built and machined surface specimens are compared in Figures 2(a) and 2(b) [7]. After the rough surface and many large elongated LOF defects close to the as-built surface were removed with surface machining, fatigue performance significantly improved even in the presence of large internal defects. It can be seen in Figures 2(c) and 2(d) that specimens manufactured with M290 machine with well-optimized process parameters contain significantly lower number of defects with considerably smaller sizes compared to specimens produced by the AM250 machine. Consequently a significant improvement in fatigue performance is observed. The M290 HIPed specimens showed coarser lamellar α+β microstructure as opposed to the annealed specimens with martensitic microstructure. The improved microstructure after HIPing creates higher ductility which reduces sensitivity to the defects. Improved fatigue performance after HIPing, as can be seen in Figures 2(e) and 2(f), is more pronounced at longer fatigue lives.

| $\sqrt{A_{dp}}$ (µm) | Ti-6Al-4V AM 250 Annealed As-built Surface | Ti-6Al-4V AM 250 Annealed Machined Surface |
|---|---|---|
| 20-50 | 3718 | 2442 |
| 50-100 | 7297 | 2143 |
| 100-200 | 3564 | 485 |
| 200-500 | 875 | 78 |
| 500-1000 | 22 | 1 |
| > 1000 | 2 | 0 |

(a)

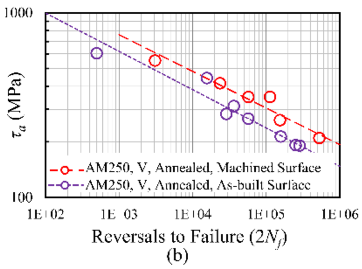


(b)

| $\sqrt{A_{dp}}$ (µm) | Ti-6Al-4V AM 250 Annealed Machined Surface | Ti-6Al-4V M290 Annealed Machined Surface |
|---|---|---|
| 20-50 | 2442 | 247 |
| 50-100 | 2143 | 43 |
| 100-200 | 485 | 0 |
| 200-500 | 78 | 0 |
| 500-1000 | 1 | 0 |
| > 1000 | 0 | 0 |

(c)

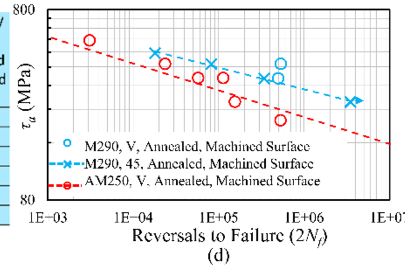


(d)

| $\sqrt{A_{dp}}$ (µm) | Ti-6Al-4V M290 Annealed Machined Surface | Ti-6Al-4V M290 HIPed Machined Surface |
|---|---|---|
| 20-50 | 247 | 48 |
| 50-100 | 43 | 1 |
| 100-200 | 0 | 0 |
| 200-500 | 0 | 0 |
| 500-1000 | 0 | 0 |
| > 1000 | 0 | 0 |

(e)

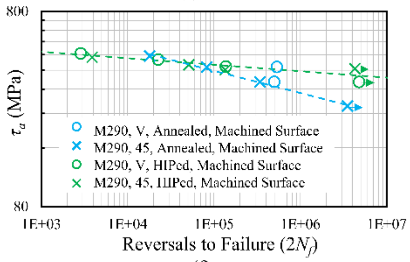


(f)

**Figure 2:** Comparison of defect size and number of defects in one specimen for different conditions, along with the corresponding comparison of fatigue performance of each two conditions under torsion loading. (each condition is denoted with the same color in all plots). (a) and (b) AM250 annealed as-built surface vs. machined surface; (c) and (d) M290 annealed machined surface vs. AM250 annealed machined surface;(e) and (f) M290 annealed machined surface vs. HIPed machined surface.

## 4. Effect of Surface Roughness on Fatigue Performance

Surface roughness of metal AM parts has a critical and dominant role on their fatigue performance. Most of the studies represent roughness with the arithmetic avergae of the roughness profile $R_a$. Examples of fatigue life correlations at a constant stress level with square root of $R_a$ for non-HIPed and HIPed specimens can be seen in in Figure 3(a) and 3(b) [8], respectively. Specimens shown in Figure3(a) were built with similar AM machines and processing conditions and therefore had similar internal defects with the largest defect size arround 50 µm. Fatigue life decreases with a increase in $R_a$ as a representation of surface roughness for specimens tested at both $R$ = -1 and $R$ = 0.1 and for both HIPed and non-HIPed specimens. Fatigue life for specimens with similar microstructures and smooth surfaces is highly dependent on the initial internal defect size and stress level. However, in the presence of surface defects or surface roughness, the roughness has the primary effect of fatigue performance and internal defects and microstructure have secondary effects. It is known that even in uniaxial loading thes surface defects create higher stress concentrations than internal defetcs. Surface roughness can be considered as a defect with defining an equivalent defect size later for fatigue life calculations.

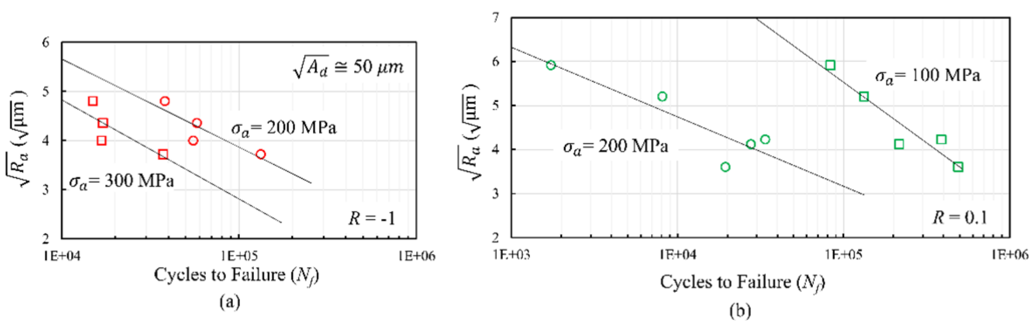


**Figure 3:** Correlations between fatigue life calculated from the stress-life fits at two different stress levels and square root of Ra: (a) R = -1 data on non-HIPed specimens, (b) R = 0.1 data on HIPed specimens.

## 5. Modeling the Effect of Defects on Fatigue Performance

Metal AM defects can be considered as existing cracks for fatigue life prediction based on internal defects using fracture mechanics approaches. These approaches need defect information such as size, shape, and location, loading information, material properties such as threshold value for stress internsity and fracture toughness, and the appropriate constants based on the adopted equation for each material, processing, and post-processing condition. To incorporate the effect of defect size, an effective initial crack size is defined based on the maximum prospective internal defect size and the maximum prospective equivalent surface defect size determined from the surface roughness profile. One approach is using a generalized Paris equation proposed by Pugno *et al.* [9] for prediction of the fatigue life. The effective initial defect size and shape represented by aspect ratio were calculated based on the size of the internal defects using Extreme Value Statistics and the surface roughness profile, and shape of the defects observed on the fracture surfaces. The defect size was projected perpendicular to the direction of maximum principle stress for each loading condition. Prediction results for as-built surface annealed Ti-6Al-4V AM250 specimens is presented in Figure 4 [10]. Solid data points are associated with specimens for which defects significantly larger than the ones found during defect characterization and used for EVS were responsible for fatigue failure and were observed on the fracture surfaces. These very large defects are caused by inconsistencies in the process.

| Loading | α(°) | $\sqrt{area}_p$(mm) |
|---|---|---|
| -- Axial | 0 | 0.394 |
| -- Torsion | 45 | 0.278 |
| -- In Phase | 155 | 0.362 |

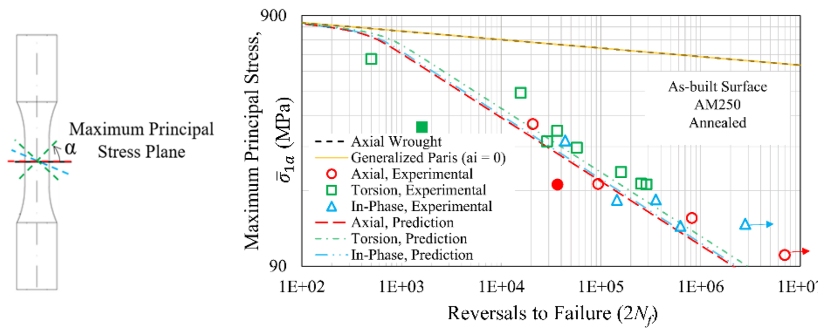


**Figure 4:** Experimental data and calculated fatigue curves (Aspect Ratio = 0.25) for different loading conditions of annealed LB-PBF Ti-6Al-4V with as-built surface condition using generalized Paris equation.

## Acknowledgements

Financial support for this project was provided by NAVAIR. VGSTUDIO MAX 3.1 software license for this project was provided by Volume Graphics. The authors would like to thank Dr. Nima Shamsaei of Auburn University for Fabricating most of the AM specimens. The authors would like to thank Nam Phan and Brendan Lessel for the CT scans.

## References

[1] N. Sanaei, A. Fatemi, and N. Phan, "Defect characteristics and analysis of their variability in metal L-PBF additive manufacturing," Materials & Design, vol. 182, p. 108091, 2019.

[2] T. M. Mower and M. J. Long, "Mechanical behavior of additive manufactured, powder-bed laser-fused materials," Materials Science and Engineering: A, vol. 651, pp. 198-213, 2016.

[3] M. Seifi, A. Salem, D. Satko, J. Shaffer, and J. J. Lewandowski, "Defect distribution and microstructure heterogeneity effects on fracture resistance and fatigue behavior of EBM Ti–6Al–4V," International Journal of Fatigue, vol. 94, Part 2, pp. 263-287, 2017.

[4] K. S. Chan, "Roles of microstructure in fatigue crack initiation," International Journal of Fatigue, vol. 32, no. 9, pp. 1428-1447, 2010.

[5] A. Fatemi, R. Molaei, J. Simsiriwong, N. Sanaei, J. Pegues, B. Torries, "Fatigue behavior of additive manufactured materials: An overview of some recent experimental data for Ti-6Al-4V considering various processing and loading direction effects," Fatigue & Fracture of Engineering Materials & Structures, vol. 42, pp. 991-1009, 2019.

[6] N. Sanaei and A. Fatemi, "Quantitative analysis of the effect of defects on fatigue performance of additive manufactured metals, part I: Internal defects, " in Preparation for Materials Science and Engineering: A, 2019.

[7] N. Sanaei and A. Fatemi, "Quantitative analysis of the effect of defects on fatigue performance of additive manufactured metals, part II: Surface roughness," in Preparation for Materials Science and Engineering: A, 2019.

[8] N. Pugno, M. Ciavarella, P. Cornetti, and A. Carpinteri, "A generalized Paris' law for fatigue crack growth," (in Journal of the Mechanics and Physics of Solids, vol. 54, no. 7, pp. 1333-1349, 2006.

[9] R. Molaei, A. Fatemi, N. Sanaei, J. Pegues, N. Shamsaei, S. Shao, P. Li, D.H. Warner, and N. Phan "Fatigue of additive manufactured Ti-6Al-4V, part II: The relationship between microstructure, material cyclic properties, and component performance," International Journal of Fatigue, 2019, Under Review.

# Analysis of driven piles using the peridynamic model

Nicolas Sau[a], Jose Medina-Mendoza[a], Antonia Lopez-Higuera[a]

[a]*University of Sonora, Boulevard Encinas & Rosales, Hermosillo 83000, Mexico*

*E-mail address:* nicolas.sau@unison.mx

**Abstract**

The Peridynamic Model has a great potential for application in soil mechanics since the soil mass can be modelled as a group of particles that interact with each other. In this work, we determine the bearing capacity of deep foundations where stresses are transmitted to deep deposits, which generally present better characteristics in terms of compressibility and shear strength. One of the main elements are driven piles, which must be previously designed, made and tested before their final use. In this work a comparison with different methods is presented. The finite element method and the peridynamic model are used. Because the effect of consolidation was not taken, in these examples the assumption is made that the structures are cemented in inert soil. Likewise, it is assumed that the water table has no influence on the simulations. Failure envelopes were observed where bonds between particles present high gradients of deformation and fracture. Bearing capacities were estimated and compared with those obtained from the Terzaghi and Meyerhof methods.

***Keywords**:* foundations; piles; soils; peridynamics

## 1. Introduction

Soil is a complex material which, in order to be modeled, requires important hypotheses similar to those made in other branches of mechanics, such as continuity, homogeneity and isotropy. Due to these hypotheses, there are significant differences between theoretical models and reality. So the good judgment of the engineer and his experience play a key role. For the calculation of foundations there is a variety of solutions for different given problems, such as footings and piles. In the analysis and design of foundations it is necessary to choose the type of suitable model that represents the situation faced by the project engineer.

There are two major classes of foundations, surface and deep foundations. Piles are a type of a deep foundation, which are classified as friction piles and tip piles. These types of elements must be analyzed and tested prior to placement. For the calculation of superficial and deep foundations there are different theories developed mainly by Terzaghi, Meyerhof and Prandtl [1]. These types of models are the most accepted today by the engineer. However, given the rise of computers in recent years, there has been a tendency to use other methods of analysis such as the finite element.

Current models have limited applications to quasi-fragile structures such as rocks and soil. Existing models for quasi-fragile materials can be classified as continuous and discrete. The formulation of the finite element method is a remarkable advance in the modeling of civil engineering structures. However, problems appear when damage and discontinuities develop in these types of structures [2].

In an effort to correct the deficiencies of continuous models, the "peridynamic" model was proposed in 1998 by Silling. Stewart Silling proposed in 1998 the peridynamic term of the Greek word "peri" which means close. The equations in this type of formulation do not assume spatial differentiation of the field of displacements and allow discontinuities to arise as part of the solution [3]. This approach is also interpreted as a continuous adaptation of molecular dynamics models. Peridynamic theory is not local, where locality recovers as a special case. In addition, the peridynamic formulation can be considered as a generalization of the classical theory of elasticity.

Obviously it is not correct to model the soils as continuous materials using smeared cracks as is done in many material models such as in concrete and rock models, however, soil is far from being a continuous material, where the mechanisms of general failure can be compared with the propagation of cracks in quasifragile materials. Therefore, nowadays, continuum models of damage mechanics are used, similar to smeared crack models, and discrete models such as discrete element methods and molecular dynamics schemes, which present their advantages and disadvantages [4].

In this study, the load capacity of friction and tip piles is analyzed using conventional methods according to the failure mechanisms proposed by Terzaghi and Meyerhof. Also two computational models are used.

The first is the finite element method using a damage mechanics model and the second is the peridynamic model in which forces between pairs of particles are used.

## 2. Analysis of driven piles

Three types of analysis are presented: the first one is using conventional models such as the ones proposed by Terzaghi and Meyerhof, the second one is using the finite element method, and the third one bond based peridynamics is used.

### *2.1. Analysis using Bearing Capacity Theories*

By analyzing semi-infinite two-dimensional media using continuum mechanics, solutions were obtained for surface and deep foundations. These solutions were used by Terzaghi and Meyerhof in the development of Soil Mechanics and Geotechnics models, which were adapted for square or circular section foundations. Terzaghi theory uses Prandtl and Reissner solutions formulated in 1921 and 1924 respectively, in which a continuous two-dimensional, semi-infinite, homogeneous and isotropic medium is assumed using plane strain conditions. In this model the theory of plasticity is used in the limit state, assuming a perfectly plastic model. In these theories, Mohr-Coulomb failure envelopes are used in which soil is considered to have cohesion and friction properties between particles.

To solve this problem, the length of the foundation is assumed to be infinite since it is a two-dimensional plane stress problem. Likewise, soil above the foundation depth is replaced with a uniformly distributed load, as shown in [1]. With this model the following formula was obtained for the calculation of the bearing capacity.

$$q_u = CN_c + \gamma D_f N_q + 0.5\gamma B N_\gamma, \tag{1}$$

in which, C is the soil cohesion, $\gamma$ is the soil volumetric weight, $D_f$ is the footing depth, $B$ is the foundation width, and, $N_c$ , $N_q$, $N_\gamma$ are factors that depend on the soil internal friction angle.

For example, for a tip pile with a foundation depth of 1.0 m, a soil volumetric weight of 1.5 ton/m$^3$, a pile diameter of 15.2 cm, a soil internal friction angle.the angle of 30° and the cohesion is null, the bearing capacity can be calculated assuming a local type of failure. For this type of failure the values of $N_c$, $N_q$, $N_\gamma$ are 18.0, 7.0 and 5.0 respectively. Using Equation (1) the bearing capacity is 10.84 ton/m$^2$. The total capacity is obtained by multiplying by the transverse area of the pile, so that the bearing capacity is 0.197 tons.

If this problem is analyzed as if the pile worked under friction, the equation to obtain the bearing capacity is as follows

$$q_f = 0.5\,\pi\,D\,K_o \gamma L^2 \tan\delta, \tag{2}$$

where D and L are the diameter and length of the shaft respectively, $\gamma$ is the soil volumetric weight, $K_o$ is the soil friction coefficient and $\delta = \frac{2}{3}\,\phi$, in which $\phi$ is the soil internal friction angle. For this example, the value of $\delta$ is 22 °, the value of $K_o$ is 0.5 and the values of the other variables remain unchanged. Using Equation (2) the bearing capacity considering only friction is 0.072 tons.

### *2.2. Analysis using the Finite Element Method*

Discontinuities are present in quasibrittle materials even when they are unloaded. In the model of smeared cracks, the constitutive properties of the material are artificially modified instead of their geometric properties. The previous problem is analyzed using the smeared crack model with the finite element method. To perform the analysis with the finite element, rectangular elements were used (Fig. 1). Soil modulus of elasticity considered was 70 MPa with a Poisson ratio of 0.3, and the modulus of elasticity of the concrete pile concrete was 25 GPa with a Poisson ratio of also 0.3. The maximum tensile soil stretch is $1.3 \times 10^{-6}$ and in compression is $1.0 \times 10^{-5}$. For concrete tension, the maximum strain is $1.3 \times 10^{-4}$ and $1.0 \times 10^{-3}$ for concrete compression. A total of 78 nodes with two degrees of freedom each and 120 elements in total were used.

Using the finite element method with the spread distribution model, the maximum load obtained is 0.01 tons. Since this method is very sensitive to the mesh size, the maximum load corresponding to the creep point of the strain-stress curve was taken. Due to this mesh sensitivity, different non-local methods have been proposed such as the peridynamic model.

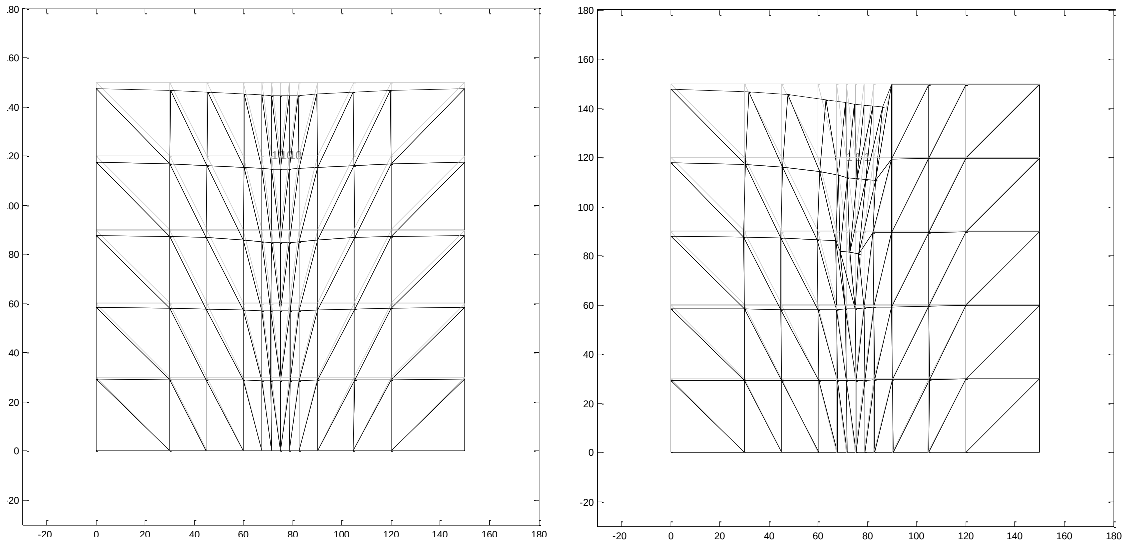

**Figure 1**: failure sequence of a pile using the finite element method

### *2.3. Analysis using the Peridynamic Model*

In the peridynamic formulation a vector function that represents the interaction between pairs of particles is postulated. This function depends on the force and its units are force by unit volume squared. The force is supposed to be a function of the relative position and the relative displacement between the particles of an elastic material. It is also assumed that there is a positive value called the material horizon in which the particles outside this horizon do not interact.

Using the peridynamic model, a computational model was developed in which particles are distributed in an array, where dynamic equilibrium equations are satisfied. With this model the problem of a tip pile subject to a vertical load is analyzed in which load is increased monotonically. Likewise, the same material properties used in the finite element example were chosen. In Figure 2 the pile model subjected to a vertical pressure is shown using the peridynamic model. With this model the maximum load obtained for a creep state is 0.009 tons.

## 3. Conclusions

In this work, the study of the bearing capacity of foundation piles subjected to vertical loads was performed. Current design methods are based on Terzaghi and Meyerhof theories. These models were formulated at the beginning of the past century and are based on theories of elasticity and perfect plasticity models. Nevertheless, there are strong hypotheses in the development of these theories such as continuity and perfect failure surfaces.

With the advent of the computer age there has been an advent of mechanistic methods for many civil engineering problems, both in soil mechanics and in structural mechanics. Most popular methods are the finite element, discrete element methods and smeared crack models.

By performing the analysis with the finite element method and the smeared crack model in its linear portion, it was found that the pile resistance was around 0.01 tons. This value is far from the values obtained with the semi-empirical models of Terzaghi and Meyerhof. One possible reason for this difference is that the maximum load in the linear finite element method is quite far from the ultimate load in the theories of Terzaghi and Meyerhof, in which plastic failure envelopes are used.

In an effort to unify continuum non-linear models and particle models, the peridynamic model was proposed. The peridynamic model is a continuous version of molecular dynamics models where discontinuities are part of the formulation. However, using particles has the disadvantage of using a large amount of computational resources.

Using the peridynamic method to the analysis of piles, a maximum load of 0.009 tons was obtained at the creep level, very similar to the value obtained with the smeared crack model. However, it was observed that the pile remained stable for higher loads, where areas of plasticity and discontinuities in the soil mass were obtained. However, no failure envelopes could be observed as predicted in the Terzaghi and Meyerhof models.

Therefore, it is important that future research on mechanistic models unify continuum theories and particle models. It is also necessary to conduct mesh convergence studies to be able to make a complete verification of these models. In addition to this, three-dimensional mechanistic models should be incorporated into these studies.

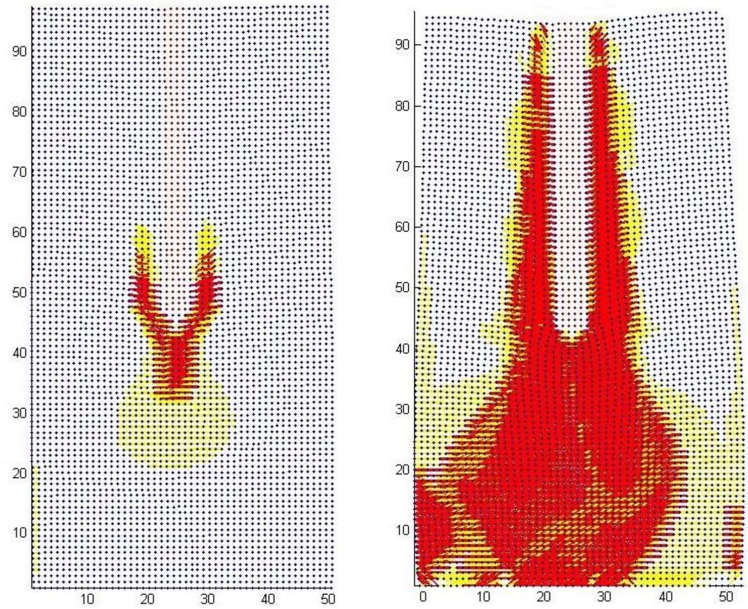


**Figure 2**: failure sequence of a pile using the peridynamic model.

## References

[1] Juárez, B., Rodríguez, R., "Soil Mechanics, Vol. II", Limusa Ed. 1997.
[2] Sau, N. "Peridynamic Model of Quasibrittle Structures". Doctoral Dissertation, University of New Mexico, 2008.
[3] Silling S. A., "Reformulation of elasticity theory for discontinuities and long-range forces". Journal of the Mechanics and Physics of Solids, 48, 175-209. 2000.
[4] ACI, American Concrete Institute. "Finite element analysis of fracture in concrete structures". Report ACI 446.3R-97. 1997.

# Stress constrained topology optimization based on a minimum compliance script

Abdelhak Touiti, Abderrahim Talha, Jean-Marie Nianga, Driss Marhabi

*"Pôle matériaux innovants", HEI – Hautes Études d'Ingénieur, 13 rue de Toul, BP 41290 , 59014 Lille*

*E-mail addresses:* abdelhak.touiti@yncrea.fr, abderrahim.talha@yncrea.fr

**Abstract**

With the emerging development of additive manufacturing process, Topology Optimization (TO) have a more and more significant importance as a design assistance tool. It allows weight reduction while it guarantees reliability, integrity and operational safety of industrial structures, particularly those of the transportation industry.

The aim of this paper is to present a new MATLAB topology optimization program derived from the top88 code written by Ole Sigmund. This is achieved through implementation of a supplementary module. This new script allows obtaining an efficient topology of a structure in term of weight, stiffness and strength. The algorithm is still solving the minimum compliance problem, it is also still using filtering, and is always used for simple 2D cases. The local stress is calculated for every element. The volume fraction, which was an entree variable of the original script, is now determined automatically in order to respect the admissible stress criterion for each finite element of the structure. The Common example of an MMB beam is discussed and its results are noted to be in good agreement with those obtained by a Standard Structural Calculation (SSC) software. The results are also compared to those from a commercial TO software.

***Keywords:*** Topology optimization ; Structures weight reduction ; Stress criterion ; Minimum compliance problem ; MATLAB.

## 1. Introduction

Weight is a major parameter in mechanical design for transportation. It has a significant influence on economizing the utilized materials, which are often very expensive (Aluminum, Titanium, Composite...). Moreover, weight affects energy consumption, as heavier mechanical parts lead to heavier vehicles that consume more fuel. Those are the reasons for the introduction of topology optimization.

Topology optimization was first introduced to structural optimization by Bendsoe and Kikuchi [1], in order to help designers in finding a material distribution of a maximal stiffness in a reference design domain with a limit on the volume. The first open source TO program was Sigmund's 99 line MATLAB program published in 2001 [2]. Popular TO methods are the SIMP method, which penalize the intermediate densities, and the Homogenization method, which optimize composite geometrical characteristics. Another advanced method is the Level Set Method [3], which has the advantage of optimizing both topology and shape.

Topology Optimization problems are time costly due to its iteratively huge number of finite element calculation. SIMP is the most time efficient method by means of its simplicity. That is why most commercial softwares are based on it. Another characteristic of the TO problem is that it has more than one optimal solution, depending on the mesh. Sensitivity and density filters have demonstrated to be good tools to obtain mesh independent material distribution. In addition, filtering gives the designer the freedom to choose the minimum diameter of the bars of a truss structure that was generated by a TO algorithm.

However, and as stated before, it is always more interesting for engineers to search for weight optimized structures rather than those with a maximum stiffness. For this purpose, stress-constrained topology optimization problem was introduced [4]. This problem is known for its complexity as it is nonlinear and with degenerated solution. The relaxation method has been introduced for solving the degeneration issue [5].

Yet there is no available published scripts or practical methods for solving this problem, this is because of the high commercial value of such scripts. The only open source code for stress-constrained TO with SIMP method is the PTOs [6] and it's using a non-gradient method which consists of attributing density values to each finite element proportionally to each elementary stress.

This paper purpose is to introduce a new method for solving the stress-constrained problem by adding a while loop to the 88 line script and a module that analyses the Von Mises stresses. The obtained results are verified using an SSC software and compared to those established by the TO software Inspire.

## 2. Theoretical background

### *2.1. Stress Constrained Topology Optimization (SCTO)*

The aim of SCTO is to find the volume fraction $vf$ that minimizes the weight of a structure by minimizing its total volume $\mathrm{V}$. The minimum weight problem is written as follows:

$$\begin{cases} \min_{vf} \quad \mathrm{V} = \sum_e \rho_e v_e \\ s.t. \quad \mathbf{Ku} = \mathbf{f} \\ \qquad \sigma_{VMe} \leq \dfrac{\sigma_y}{\alpha} \qquad \forall e \in \{1,..,N\} \\ \qquad 0 < \rho_e \leq 1 \end{cases} \tag{1}$$

Where $\mathbf{K}$ is the global stiffness matrix, $\mathbf{u}$ is the global displacement vector, $\mathbf{f}$ nodal forces vector, $v_e$ is the volume of a single element $e$ on $N$ total number of finite elements, $\sigma_{VMe}$ is the Von Mises stress calculated in element $e$, $\sigma_y$ the material yield limit and $\alpha$ is a security coefficient that is to be chosen by the designer. $\rho_e$ is the elementary volume density. Its value must be strictly superior to zero in order to avoid singularity in stiffness matrix. The optimization result consists of a distribution of the material density with a minimal weight. This guarantees resistance to applied loadings.

### *2.2. Initial script*

The basic script is the top88 [7] written by Sigmund in 2010. It uses the SIMP method for an elastic isotropic material 2D model and works in the same way as top99, but with fewer iterations by using prelocalized tables and vectorization of loops. Figure 1 represents its corresponding parameters.

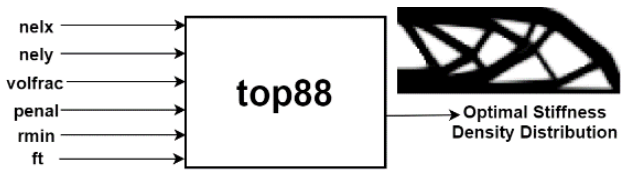


**Figure 1**: Input and output of the top 88 code

nelx and nely are the number of finite elements in the x and y directions of the design domain, rmin is the filter radius, penal is the penalty exponent and volfrac is the volume fraction of the optimized structure. volfrac is always chosen by the designer.

Top88 gives a result of the minimum compliance problem, which consist of seeking the density distribution of a structure with a maximal stiffness. The MCP is defined as follows:

$$\begin{cases} \min_{\rho} \quad c = \mathbf{u}^t \mathbf{K} \mathbf{u} \\ s.t. \quad \mathbf{Ku} = \mathbf{f} \\ \qquad \sum_e \rho_e v_e < V_{\lim} \\ \qquad 0 < \rho_e \leq 1 \end{cases} \tag{2}$$

Where c, defined as the compliance, is a quantity that characterizes the global elastic energy.

Physically, for a constant loading, the strains and the elastic energy are smaller when the material is stiffer. That is why the goal is to minimize the elastic energy.

## 3. Modification taking into account the stress criterion

The modified script, as shown in figure 3, consists of a loop on the top 88 program for finding a minimal volume fraction value that allows the structure to locally resist to the stress limit $\sigma_y/\alpha$ . This is achieved by calculating the Von Mises Stresses in every finite element and by comparing its value with the stress limit. If the stress limit criterion is verified, a total mass reduction can still generate a resistant structure. volfrac is then reduced and the top 88 is relaunched to obtain an optimal stiffness density distribution. However, if the stress criterion is not respected, a critical area with regard to the applied load exists. The modified code thus increases volfrac. This whole loop is repeated until volfrac value converges to a relative change lesser than 0.01. The final result is a topology of resistant structure with a minimal weight.

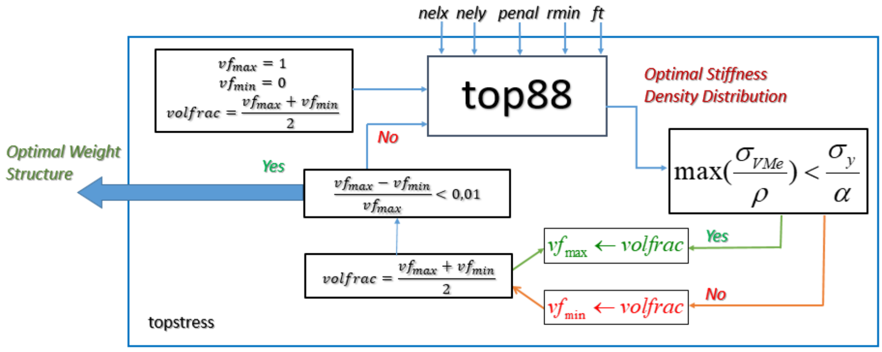


**Figure 3**: Block chart of the modified code

## 4. Studied Example

For this paper, the MBB beam was chosen as a 2D example for modified code "topstress" (see Fig 2), with a thickness of 10 mm, a length of 1 meter and a height of a 40 cm**.** It is discretized into 100×40 square elements of length 10mm. p value is 3 and rmin value is 1.5. The ASTM A36 Steel characteristics are a Young Modulus of 200 GPa, a Poisson's ratio of 0.26 and a Yield limit of 250 MPa. A security coefficient of 1.5 is used. A point force of 10 kN is applied in the top left corner of the Beam.

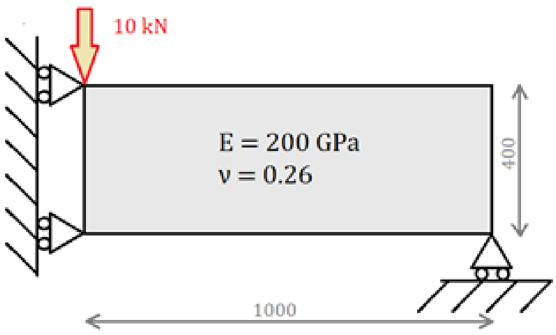


**Figure 2**: Studied example by the modified code

## 5. Results and Discussion

When we run the program, we observe iterations of removing and adding material to the structure until obtaining a final structure of a converged value of the volume fraction.

Figure 4 shows the optimization result of our example. The resulted structure is obtained after 12 iterations on volfrac. The final optimal compliance and volume fraction values are respectively 14.885 J and 0.218. This volume fraction value correspond to a weight of 6.802 kg (mass reduced by 78%). The obtained structure is a truss structure with 6 rectangular bars of different Heights. The bars were numbered from 1 to 6 to make the discussion easier.

This optimized structure is a minimal weight structure that will resist to the 10 kN applied force, along with a maximal stiffness. It should also be pointed out that this structure is not the optimal structure due to the non-convexity of the TO problem.

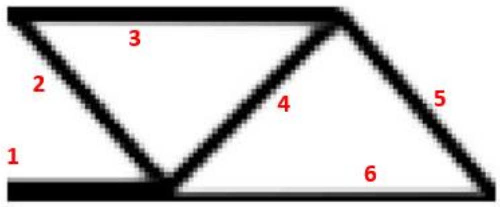


**Figure 4**: Output of the modified code

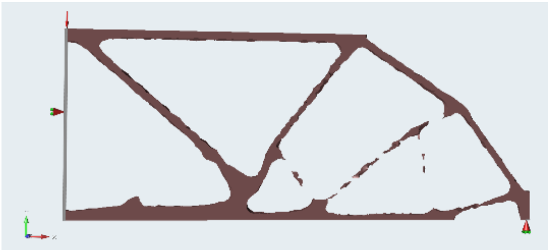

**Figure 5**: Results obtained from Inspire

Using the generated data of top 89, the elementary Von Mises stresses values were extracted and the dimension of each bar was calculated from the global density matrix. The following table presents the dimensions, the maximal value and the mean value of Von Mises stresses on each bar. The last column presents the mean VM stress calculated using an SSC software for the same obtained structure and the same loading and boundary conditions. The aim is to verify values of the stresses obtained by topstress.

**Table 1.** Results obtained by topstress and by an SSC software (stresses are in MPa and lengths are in mm)

| Bar Number | topstress Bar Height | topstress Bar Length | topstress Bar $max(\sigma_{VMe})$ | topstress Bar $mean(\sigma_{VMe})$ | SSC software $\sigma_{VM}$ |
|---|---|---|---|---|---|
| 1 | 42.7 | 330 | 69.3 | 62.8 | 58.8 |
| 2 | 28.6 | 550 | 72.9 | 45.9 | 45.4 |
| 3 | 32.3 | 670 | 66.2 | 55.8 | 52.0 |
| 4 | 29.4 | 556 | 62.4 | 47.2 | 46.2 |
| 5 | 28.2 | 550 | 64.6 | 44.6 | 44.7 |
| 6 | 16.3 | 670 | 72.4 | 51.2 | 50.9 |

The obtained bars have constant heights. The elementary stresses have constant values in the direction of each bar. The bar number one, which has the largest height, is also the bar that is submitted to the highest effort. Those results are consistent with the truss model.

Contrarily, a variation on stress values was observed in each transversal direction of each bar. This result does not conform to the truss model. This variation is explained by the existence of bending stresses, which are a consequence of the rigid connections that occur between the bars of the obtained topology.

The comparison between the VM stresses and the values of the structural software results is in an adequacy. This confirms the right choice of topstress for the calculation of VM stresses.

Lastly, Figure 5 presents the results of the stress-constrained optimization obtained by a commercial topology optimization software "Inspire". Those results are for the same problem and the same material characteristics as in our example.

We observe some slight differences between Inspire results and topstress output. They consist of adding three fine bars to the structure and a leg like shape near the right slider joint. Those differences prove the mesh dependency of topology optimization**.** Which is explained by the use of a different type of finite elements by Inspire, which are the tetrahedral FEs.

## 6. Conclusion

In this paper, we introduce a new simple method for solving the stress constrained topology optimization by implementing a while loop on the top88 script. This constructs as result a resistant structure with a minimal weight. The stress values of the obtained structure are verified by a structural software. A comparison with Inspire highlights a different geometry, which is explained by the mesh dependency of TO**,** since Inspire is using a different type of FEs. We also note that we obtain a truss like structure because the applied load was small enough**.** However, for greater loading values and the same filter radius**,** we obtain much more complicated structures that can only be manufactured by additive manufacturing.

**References:**

[1] M. P. Bendsøe and N. Kikuchi, "Generating optimal topologies in structural design using a homogenization method," *Comput. Methods Appl. Mech. Eng.*, vol. 71, no. 2, pp. 197–224, Nov. 1988.
[2] O. Sigmund, "Sigmund, O.: A 99 Line Topology Optimization Code Written in MATLAB. Structural and Multidisciplinary Optimization 21, 120-127," *Struct. Multidiscip. Optim.*, vol. 21, pp. 120–127, Apr. 2001.
[3] G. Allaire, F. Jouve, and A.-M. Toader, "Structural optimization using sensitivity analysis and a level-set method," *J. Comput. Phys.*, vol. 194, no. 1, pp. 363–393, Feb. 2004.
[4] P. Duysinx, L. V. Miegroet, E. Lemaire, O. Brüls, and M. Bruyneel, "Topology and generalized shape optimization: Why stress constraints are so important?," *Int. J. Simul. Multidiscip. Des. Optim.*, vol. 2, no. 4, pp. 253–258, Dec. 2008.
[5] G. D. Cheng and X. Guo, "ε-relaxed approach in structural topology optimization," *Struct. Optim.*, vol. 13, no. 4, pp. 258–266, Jun. 1997.
[6] E. Biyikli and A. C. To, "Proportional Topology Optimization: A new non-gradient method for solving stress constrained and minimum compliance problems and its implementation in MATLAB," *PLOS ONE*, vol. 10, no. 12, p. e0145041, Dec. 2015.
[7] E. Andreassen, A. Clausen, M. Schevenels, B. Lazarov, and O. Sigmund, "Efficient topology optimization in MATLAB using 88 lines of code," *Struct. Multidiscip. Optim.*, vol. 43, pp. 1–16, Nov. 2011.